OPTIMIZATION OF BLENDING AND SPATIAL SAMPLING IN SEISMIC ACQUISITION DESIGN

OPTIMIZATION OF BLENDING AND SPATIAL SAMPLING IN SEISMIC ACQUISITION DESIGN

Proefschrift

ter verkrijging van de graad van doctor
aan de Technische Universiteit Delft,
op gezag van de Rector Magnificus Prof. dr. ir. T.H.J.J. van der Hagen,
voorzitter van het College voor Promoties,
in het openbaar te verdedigen op woensdag 15 april 2020 om 10:00 uur

door

Shotaro NAKAYAMA

Master of Science in Earth and Planetary Science,
The University of Tokyo, Tokyo, Japan,
geboren te Hachinohe, Japan.

Dit proefschrift is goedgekeurd door de

promotor: dr. ir. G. Blacquière
promotor: prof. dr. ir. C.P.A. Wapenaar

Samenstelling promotiecommissie:

Rector Magnificus,	voorzitter
Dr. ir. G. Blacquière	Technische Universiteit Delft
Prof. dr. ir. C.P.A. Wapenaar	Technische Universiteit Delft
Onafhankelijke leden:	
Prof. dr. ir. E.C. Slob	Technische Universiteit Delft
Prof. dr. W.A. Mulder	Technische Universiteit Delft
Prof. dr. D. Gajewski	Universität Hamburg
Dr. ir. G.G. Drijkoningen	Technische Universiteit Delft
Dr. ir. G.J.M Baeten	Shell

Keywords: Acquisition design, Source blending, Spatial sampling, Optimization

Printed by: Gildeprint

Front & Back: illustAC

ISBN 978-94-6366-265-9

An electronic version of this dissertation is available at
http://repository.tudelft.nl/.

Dedicated to my family

Shotaro Nakayama

CONTENTS

SUMMARY

The quality and business aspects are both of particular importance in determining the type of seismic acquisition. Usually, a strong emphasis on cost reduction is inevitable. On the other hand, there is an increasing demand for the acquisition of high-quality seismic data that can contribute to the various stages in the field development profile. These conflicting desires eventually make conventional seismic surveys an inadequate option. The application of blended acquisition along with efficient detector and source geometries is capable of providing high-quality seismic data in a cost-effective and productive manner. This way of data acquisition also contributes to minimizing health, safety and environment exposure in the field. Blended acquisition allows multiple source-wavefields to be overlapped in time, space, and temporal and spatial frequency, causing blending interference. The acquisition of less data via sparse detector and source geometries likely violates the Nyquist sampling criterion. Therefore, to make the aforementioned approach technically justifiable, deficiencies in recorded data have to be dealt with through the course of subsequent processing steps. One way to encourage this technique is to minimize any imperfection in processing algorithms. In addition, one may derive survey parameters that enable a further improvement in these processes, which is the primary focus in this thesis.

The survey design scheme introduced in this thesis aims at the optimization of survey parameters responsible for spatial sampling of detectors and sources as well as source blending in an automated manner. The proposed approach makes use of available subsurface information to simulate the desired outcome from the survey under consideration. With this knowledge, we cast design of survey parameters as a minimization problem. Using a given design, we derive practical data, i.e., blended and sparsely-sampled data. These data are input for computing an objective function based on the residue between the desired outcome and the estimated outcome from a pre-defined quality measure. This information is then used to update the survey parameters by integrating genetic algorithms and convolutional neural networks. Bio-inspired stochastic operators enable the simultaneous updates of the blending and spatial-sampling schemes. We enable irregularity to be embedded into survey parameters, making a survey design problem complex and consequently leading to a significantly large solution space. To enhance computational efficiency, we utilize convolutional neural networks which are trained to relate the choice of survey parameters to the quality measures. The applied network architecture rejects suboptimal solutions among newly generated ones from genetic operators. Consequently, only optimal ones, i.e., according to the neural network, are fed into the subsequent step. Furthermore, the solution space is limited via the so-called repeated encoding sequence that combines a set of short binary vectors, each having a random-like feature to form a long parameter sequence representing blending and sampling operators. The proposed approach updates survey parameters for enhancement of data quality at a computationally affordable time. Although our

application does not necessarily guarantee the best output within a practical computation time, acceptable solutions are expectantly achievable. Unlike various geophysical problems seeking for the ground truth, e.g., subsurface properties, this feature is fully acceptable in an acquisition design problem as long as the resultant survey parameters satisfy a pre-set technical criterion.

When seismic data are acquired in a blended and sparsely-sampled manner, the outcome from the subsequent decompression of recorded data, comprising of deblending and/or data reconstruction, is of primary importance. We hence apply the proposed survey design to derive survey parameters that can provide optimum deblending and data reconstruction. In this application, we deal jointly with deblending and data reconstruction via a sparse inversion in the frequency-wavenumber domain, coupled with constraints based on prior knowledge such as causality and coherency. The residue between the ideal data, i.e., unblended and well-sampled data, and deblended and reconstructed data from this process is subsequently used to update the survey parameters. A comparison among different survey design strategies highlights the ability of the method to effectively derive optimum solutions. The resultant acquisition scenario derived from the proposed approach yields a notable enhancement of deblending and data reconstruction quality, attributed solely to the choice of survey parameters. Alternatively, the reduction of survey effort is also attainable without adversely affecting the resultant deblending and reconstruction quality.

While deblending and data reconstruction conventionally accompany the aforementioned acquisition strategy, the recorded data can be processed directly to estimate subsurface properties. We therefore also implement the proposed workflow to design a seismic survey, leading to optimum reflectivity and velocity estimation via joint migration inversion. In the workflow, we extend the standard implementation of joint migration inversion to cope with the data acquired in a blended fashion along with irregular and sparse geometries. This makes a direct estimation of reflectivity and velocity models feasible without the need of deblending or data reconstruction. During the iterations, the errors in reflectivity and velocity estimates are used to update the survey parameters. In this implementation, the resultant acquisition scenario also attains a clear enhancement in both reflectivity and velocity estimation attributable to the choice of survey parameters.

Acquisition of multiple seismic datasets at different moments in time is capable of satisfying the continuously increasing demand for high-quality subsurface images by extracting both static and dynamic elements during the field development. However, in practice, challenges of pursuing this strategy lie in different perspectives related to budgetary, operational and regulatory constraints. Hence, we explore a strategy allowing us to utilize seismic surveys acquired in a compressed manner in time and/or space through the field life, contributing to cost, efficiency, health, safety and environment perspectives, while recovering deblended and reconstructed data of sufficient quality. We introduce a simultaneous recovery scheme that jointly handles deblending and data reconstruction for multiple time-lapse measurements via a sparse inversion in the frequency-wavenumber domain, coupled with constraints on causality and coherency. Additionally, we formulate a single objective function enabling static information among vintages to be shared and, at the same time, dynamic changes in the reservoir of inter-

est to be extracted on the basis of prior subsurface information. We demonstrate the proposed recovery to both synthetic and real data. We also examine the effect of survey design on the quality of simultaneous recovery. Using the proposed survey design, we demonstrate optimally designed time-lapse measurements can contribute to enhancing the quality of recovered data and extract reliable time-lapse signatures.

SAMENVATTING

Bij het bepalen van de opzet van seismische data-acquisitie spelen zowel kwaliteit als kosten een belangrijke rol. Meestal ligt de nadruk op het beperken van de kosten. Er is echter ook een toenemende vraag naar seismische meetgegevens van hoge kwaliteit, die gebruikt kunnen worden in de verschillende stadia van de ontwikkeling van een veld. Aan deze tegenstrijdige eisen kan traditioneel seismisch onderzoek niet voldoen. Een kosteneffectieve en productieve oplossing is het toepassen van zogenaamde "geblende-acquisitie, gecombineerd met een efficiënte opstellingen van de ontvangers en bronnen. Daarnaast draagt deze aanpak positief bij aan veiligheid, arbo en milieu. In geblende acquisitie overlappen meerdere golfvelden elkaar in tijd en ruimte, en in temporele en spatiële frequentie, waardoor ingewikkelde interferentiepatronen ontstaan. Tijdens het meten van data met genoemde efficiënte bron- en ontvangeropstellingen is het onwaarschijnlijk dat er aan het Nyquist bemonsteringscriterium wordt voldaan. Om deze manier van data-acquisitie technisch verantwoord toe te passen moet deze beperking worden gecompenseerd door geavanceerde dataverwerking. Eén manier om de praktische toepassing van deze meetmethode te stimuleren, is het verder perfectioneren van de algoritmes voor dataverwerking. Vervolgens kan men ook meetparameters kiezen die bijdragen aan een verdere verbetering van het eindresultaat. Dit laatste is het belangrijkste onderwerp van dit proefschrift.

De methode voor het ontwerpen van een seismische survey, die we in dit proefschrift introduceren, richt zich op het automatisch optimaliseren van de surveyparameters. Deze hebben betrekking op de posities van de bronnen en de ontvangers, en de blendinginformatie van de bronnen. De voorgestelde werkwijze maakt gebruik van reeds beschikbare informatie over de ondergrond om de ideale uitkomst van de seismische dataverwerking te simuleren. Met behulp van deze informatie gieten we het ontwerpen van de surveyparameters in de vorm van een minimalisatieprobleem, dat we op een iteratieve manier oplossen. Aan de hand van een gegeven surveyontwerp genereren we een praktische dataset, met andere woorden, efficiënt gemeten en geblend. Deze dataset wordt verwerkt. Vervolgens wordt vastgesteld of het residu – het verschil tussen het resultaat van de dataverwerking en de ideale uitkomst – kleiner is dat het vooraf bepaalde criterium. Zo niet, dan wordt deze informatie gebruikt om de surveyparameters aan te passen en zodoende het residu te verkleinen. Hiervoor gebruiken we een geïntegreerde aanpak op basis van een genetisch algoritme, een convolutioneel neuraal netwerk en biologisch-geïnspireerde stochastische operatoren. We staan toe dat de surveyparameters onregelmatig mogen zijn. Hierdoor neemt de complexiteit van het probleem toe en kan de oplossingsruimte zeer groot worden. Om het uitrekenen van de oplossing efficiënter te maken, gebruiken we het convolutionele neurale netwerk, dat getraind is om de surveyparameters rechtstreeks te koppelen aan de kwaliteit van het eindresultaat. Het netwerk beoordeelt alle oplossingen van het genetische algoritme en keurt de suboptimale af. Alleen oplossingen die volgens het neurale netwerk optimaal zijn wor-

den in de volgende stap gebruikt. Verder limiteren we de hoeveelheid oplossingen door gebruik te maken van zogeheten herhaalde encoderende sequenties. Deze combineren een beperkt aantal korte binaire sets tot langere vectoren die de onregelmatige surveyparameters efficiënt beschrijven. Hoewel onze methode niet per se het beste resultaat zal opleveren binnen de beschikbare hoeveelheid rekentijd, is het aannemelijk dat de resultaten goed bruikbaar zijn. In tegenstelling tot sommige andere geofysische problemen die de absolute waarheid zoeken, zoals eigenschappen van de ondergrond, is deze beperking volkomen acceptabel voor het ontwerpen van een seismische survey. Het ontwerp voldoet immers aan het vooraf bepaalde criterium.

Als seismische data worden gemeten op deze geblende en efficiënte manier, is de kwaliteit van het proces van deblenden (d.w.z. het proces om de blending ongedaan te maken) en datareconstructie van groot belang voor het te behalen eindresultaat. Daarom baseren we het residu van onze methode op deze kwaliteit. De deblending en datareconstructie worden in onze toepassing tegelijkertijd uitgevoerd door gebruik te maken van schaarse inversie (Eng.: 'sparse inversion') in het dubbele Fourier domein (frequentie-golfgetal domein), waarbij rekening wordt gehouden met randvoorwaarden gebaseerd op a priori kennis, zoals causaliteit en coherentie. Het residu, het verschil tussen de ideale data en de data verkregen na deblending en datareconstructie, wordt gebruikt om de surveyparameters aan te passen. Een vergelijking tussen verschillende strategieën voor surveyontwerp benadrukt het vermogen van onze methode om tot optimale oplossingen te komen. Het uiteindelijke surveyontwerp leidt tot een aanzienlijke verbetering in de kwaliteit van het eindresultaat, dat wil zeggen na deblending en datareconstructie. Deze verbetering kan alleen worden toegeschreven aan de keuze van de surveyparameters. Deze oplossing leidt dus tot een verbeterde kwaliteit bij gelijkblijvende kosten. Als alternatief kan men ook streven naar een gelijkblijvende kwaliteit bij afgenomen kosten.

Deblending en datareconstructie zijn gebruikelijke stappen in de conventionele seismische dataverwerking, maar men kan deze stappen ook overslaan en de gemeten data direct verwerken om de eigenschappen van de ondergrond, zoals reflectiviteit en geluidssnelheid, in beeld te brengen. We gebruiken onze werkwijze daarom ook om een seismische survey te ontwerpen met het oog op het schatten van de reflectiviteit en de geluidssnelheid via een gecombineerd inversie-migratieproces. Daartoe hebben we een beschikbaar algoritme uitgebreid, zodat het om kan gaan met geblende data en onregelmatige bron- en ontvangerposities. Gedurende de iteraties worden fouten in de schatting van de reflectiviteit en de geluidssnelheid gebruikt om de surveyparameters bij te werken. Ook nu zien we een duidelijke verbetering in de schatting van de reflectiviteit en de geluidssnelheid, bereikt door de optimale keuze van de surveyparameters.

De eisen die worden gesteld aan de beeldvorming van de ondergrond gedurende de gehele "levensduur"van een veld worden steeds hoger. Men kan hieraan voldoen door het meten van meerdere seismische datasets op verschillende tijdstippen. Dit levert zowel statische als dynamische informatie van hoge kwaliteit. In de praktijk leidt dit herhaalde meten tot allerlei problemen gerelateerd aan budget, uitvoering en regelgeving. Daarom zoeken we naar een strategie die het mogelijk maakt om een seismische meetstrategie te ontwerpen die uitgevoerd kan worden binnen een beperkte tijd, met beperkte middelen, rekening houdend met veiligheid, arbo en milieu, terwijl tegelijkertijd het eindresultaat een goede kwaliteit heeft. We stellen een schema voor waarbij te-

gelijkertijd de verwerking van de data van meerdere tijdstippen wordt uitgevoerd door middel van schaarse inversie in het dubbele Fourier domein, gebaseerd op de randvoorwaarden van causaliteit en coherentie. Daarnaast stellen we ook randvoorwaarden op met betrekking tot het dynamische karakter van de ondergrond: sommige delen worden als tijd-invariant verondersteld, terwijl andere delen mogen veranderen als functie van de tijd. Deze keuze wordt als a priori informatie aangegeven. We laten goede resultaten van deze toepassing zien op synthetische en echte data. Tenslotte bestuderen we ook het effect van surveyontwerp op de kwaliteit van het resultaat van dit schema. We laten zien dat een optimaal ontwerp leidt tot een verbeterde kwaliteit van het eindresultaat, en dat betrouwbare informatie over veranderingen in de ondergrond wordt verkregen.

1

INTRODUCTION

1.1. SEISMIC ACQUISITION IN THE UPSTREAM SEGMENT OF THE OIL AND GAS INDUSTRY

Seismic waves that propagate through a given medium capture substantial information on its properties. The use of seismic data has contributed significantly to hydrocarbon exploration, development and production. For these purposes, a controlled man-made source, typically located at or close to the surface, generates seismic waves that penetrate down to the Earth's interior. The waves are reflected and recorded at detectors typically placed at or close to the surface. The recorded waves provide valuable insight into subsurface structures and properties. When applied in 3D, it can provide volumetric data covering the entire field without any gap. At least up until now, this is the only practically feasible way enabling an indirect measurement of oil and/or gas fields with reasonable vertical and lateral resolution, sufficient depth of investigation and sufficient spatial coverage. Due to its technical ability and wide applicability to various environments at affordable cost and time, the technique is routinely utilized to almost all the occasions in the upstream of the oil and gas industry.

1.2. BLENDED ACQUISITION WITH SPARSE AND IRREGULAR GEOMETRIES

1.2.1. DATA ACQUISITION

In a conventional seismic survey, detectors and sources are deployed at regular spatial intervals. Each source then emits a spatially uniform signature with sufficiently large temporal and spatial separations with respect to other sources. This allows the energy from the former shot to decay to an acceptable level or to propagate outside of the area of interest before the data associated with the following shot arrives at the detectors. Despite its vital role in the oil and gas industry, the acquisition of seismic data is costly and time-consuming. Furthermore, the operation inevitably entails certain health, safety

and environment (HSE) risks in the field. These factors potentially curtail our opportunities to acquire seismic data, particularly when desiring denser sampling along with longer apertures for all the azimuths. One hence needs to design a seismic survey more efficiently and cost-effectively while satisfying geophysical requirements.

Over the last decade, blended acquisition, or sometimes referred to as simultaneous source acquisition, has attained considerable attention in the industry due to its ability to drastically change the business and technical aspects of seismic data acquisition. This consequently has resulted in wide-spread applicability of the technique. Beasley *et al.* [1] proposed to deploy two sources simultaneously at both ends of a streamer cable. They demonstrated the possibility of separating interference noise using conventional processes, such as multi-channel filtering and pre-stack migration. Berkhout [2] proposed the concept of blending in acquisition and processing. Blended acquisition is a way in which seismic data are continuously recorded along with significant overlap among consecutive shots in time and space as well as in temporal and spatial frequency to produce "blended shot records". Blended acquisition is capable of recording high quality seismic images in an economically favourable way. In recent years, various field-wide applications of the technique have been easily recognizable in the industry [3–5]. While conventional seismic surveys aim ideally at regular and dense sampling, further easing the spatial sampling requirements contributes to the business aspect, and reduces the environmental footprint. For example, compressive sensing has recently been successfully implemented in the oil and gas industry. This technique allows for a non-uniform spatial sampling along with fewer measurements in the field [6, 7].

As mentioned previously, a conventional seismic survey employs a spatially uniform source signature that is normally designed to (almost) instantaneously emit all frequencies of interest at a regularly spaced interval. This wide-band and centralized source configuration is widely applied while it inherently forces a trade-off among subsurface illumination, operational flexibility, cost, time and sound exposure to the environment. Berkhout [8] introduced the dispersed source array (DSA) concept that utilizes a set of source units, each having a dedicated narrow frequency range. Caporal *et al.* [9] extensively discussed its benefits from different perspectives, some of which are reviewed as follows. DSA acquisition permits each narrow-band source to be independently deployed to satisfy its own spatial sampling criteria determined by its frequency range. This subsequently allows for proper sampling of entire frequency ranges and addresses both the oversampling of lower frequencies and undersampling of higher frequencies. The DSA concept is also capable of contributing to operational and business perspectives. In general, the sources responsible for the high frequencies can be smaller, lighter and less expensive than conventional broadband sources. The sources for the low frequencies can be deployed at much coarser intervals than the conventional ones, leading to the reduction of acquisition effort. The concept has gradually become realizable in the industry. For example, Dellinger *et al.* [10] introduced a marine source dedicated to cover low frequency components that conventional sources are unable to generate. Additionally, this source can be deployed separately and independently from conventional ones, making the DSA concept feasible.

1.2.2. DATA PROCESSING

When data acquisition is carried out in a blended, irregular and sparse fashion (both in the spatial and temporal frequency), an extra effort in data processing is inherently required to address the deficiency of the recorded data. Due to the large imbalance between acquisition and processing effort and cost, this extra effort is reasonably acceptable as acquiring the actual, unblended traces in a conventional way is far more costly. Therefore, this acquisition strategy potentially enhances the value of a seismic survey further, provided that the quality of processed data is ensured.

A common practice to process blended data is to deblend the recorded data first. In most cases, deblending is posed as an inversion problem that (iteratively) estimates unblended data in some transform domain such as the Fourier [11], Radon [12], Curvelet [13] or Focal [14] domain. The deblended data then enables us to make use of standard processing algorithms and to treat the data as if it were acquired in a regular, unblended manner. Recovery of missing data from compressive measurements allows the processed data to attain the desired data density. Several studies have demonstrated both practical and theoretical aspects of data reconstruction. For instance, well-known and widely-used approaches are transformation-based ones such as the use of the Fourier [15], Curvelet [16], Radon [17] or Focal [18] domain. As forward and inverse operators for these domains are not orthogonal, data reconstruction is generally posed as an inversion problem to minimize loss of information in input data. Signals are iteratively estimated in the transform domain where undesired events are better separated from desired signals than in the time-space domain. After estimating the model parameters through minimizing a defined objective function under certain constraints, the data at any desired grid can be recovered via the inverse transformation.

An alternative, more modern approach to handle blended data is to apply imaging without deblending [9, 19–22]. Instead of directly migrating blended data, these studies utilized a least-squares migration (LSM) scheme. The formulation of the imaging problem as a least-squares problem enables LSM to iteratively minimize the misfit between the real and the modelled blended data, which consequently produces the subsurface reflectivity without the separation of blended wavefields. Insufficient spatial sampling in the acquisition often induces aliasing noise in migration. A common practice to address this issue is to apply data reconstruction prior to imaging, yet alternatively, LSM can be used for this purpose. Nemeth *et al.* [23] showed that the technique is capable of suppressing migration artefacts and producing images with balanced amplitudes and high resolution even when the input data suffer from coarse and/or irregular spatial sampling. Full-waveform inversion (FWI) is capable of using the acquired seismic data to retrieve the subsurface properties that determine the seismic wavefield in an iterative manner [24], i.e., blended records can be directly used in FWI, which attempts to minimize the misfit between observed data and forward-modelled blended data [25]. Due to the heavy computational burden in FWI, the concept of blending is considered as one of the crucial strategies to improve its efficiency, even when the acquired data were not blended. It combines individual shot records into super-shot records which are then simulated during waveform forward modelling and the residuals are back-propagated for gradient calculation. This implementation ideally accelerates the inversion process with a factor of the number of shots gathered in the super-shot record.

1

1.3. ACQUISITION DESIGN

The relevant and conventional survey parameters, for both land and marine environments, are the detector and source intervals along two perpendicular directions as well as the detector and source apertures along two perpendicular directions of the template geometries [26]. In a conventional way, as long as detectors and sources are regularly deployed, the design of these parameters is still manageable [27, 28]. However, this is not the case with blending and irregular geometries. Despite their potential benefits, designing a survey incorporating these techniques is rather intricate as irregularity or randomness is often embedded into the survey parameters, making a survey design problem significantly large and complex.

In existing blended acquisition schemes, the source wavefield is often made incoherent in at least one of the sorting domains by the use of a random time delay, a randomized distance between concurrent sources for each blended shot, a unique encoding for each source, or by their combination [29]. Similarly, irregularity is also of importance when sampling detectors and sources. For example, spatial sampling of data in an irregular fashion is a key element to implement compressive sensing [6, 7, 30]. The irregularity permits energy of spectral leakage to spread over the entire spectrum and to behave as if it were random noise. In compressive sensing, those random-like artefacts are well separated in a certain transform domain. A subsequent sparsity promoting inversion makes the recovery of desired signals realizable.

A fundamental drawback in estimating reflectivity or velocity directly from blended data is the crosstalk noise that arises from the interference of overlapping wavefields from multiple sources. One way to minimize this issue is to encode the sources to be blended both for LSM and FWI, see for example the studies by [31–35]. In these studies, different source encoding schemes were implemented, such as the use of random time shifts, frequency scheduling, amplitude encoding, selection of source locations used for the inversion, or combinations thereof. However, the inadequacy in spatial sampling still deteriorates inversion results [33, 36]. Boonyasiriwat and Schuster [32] applied a random distribution of sources to minimize the crosstalk noise in FWI. Wang *et al.* [37] confirmed the improvement of FWI results with irregularly-decimated data as compared to regularly decimated data.

By taking the effectiveness of the subsequent processes into account, we can potentially design an economically favourable seismic survey without jeopardizing data quality. When designing a survey or assessing a given acquisition geometry, common midpoint (CMP) based attributes such as fold and sampling in different offset as well as azimuth ranges are widely used as illustrated in [26, 38]. Although they can quickly provide beneficial information on anticipated data quality from a given acquisition geometry, these attributes inherently disregard the effect of processing. With the application of blending and irregular spatial sampling, the quality of subsequent processes is inevitably a major concern, so one eventually needs another means. One solution would be to build a field-wide subsurface model with finer grids followed by forward modelling of any anticipated acquisition scenarios [e.g., 39]. This certainly requires enormous computer resources, funds and time, which may not be allocated to every occasion. Therefore, it is obviously worthwhile to seek an efficient and practical way to design a survey to incorporate blending and irregular geometries. Additionally, different types of survey

parameters interactively influence the quality of the subsequent processing steps and eventually that of the final subsurface image. To deal with this, we have to optimize the parameters simultaneously rather than sequentially.

Even though the application of random realizations is still a common practice to incorporate irregularity into acquisition parameters, in recent years, there have been several studies that aim to design the irregularity. Mosher *et al.* [7] derived irregular acquisition geometries from several hundreds of Monte Carlo simulations for the implementation of compressive sensing. Jamali-Rad *et al.* [40] demonstrated that effective recovery of sparsely sampled data is attainable by minimizing the maximum mutual coherency of a dictionary matrix determined from the acquisition geometries. Additionally, Campman *et al.* [30] outlined that the ability to reconstruct a sparsely-sampled seismic wavefield can be enhanced by optimization of the dictionary matrix, which guides the choice of acquisition parameters. Abma and Ross [41] introduced popcorn shooting for marine seismic surveys, which permits a firing time of an individual airgun in an array to vary over a given time period. They pointed out that minimal correlations among the popcorn signatures enhance the performance of deblending. Mueller *et al.* [42] demonstrated a method of encoding source sequences using simulated annealing to improve deblending quality. In addition, Wu *et al.* [43] proposed a blending code so-called shot repetition that enables multiple shots to be repeatedly activated at the same location. They obtained shot-repetition codes that make effective deblending realizable from 10000 random realizations. Nevertheless, few studies have investigated the optimization of source blending as well as detector and source geometries in a combined way, which is the topic of this thesis.

1.4. SEISMIC ACQUISITION THROUGH THE FIELD LIFE

It is widely recognized that seismic data is indispensable in hydrocarbon exploration. The information from seismic data also plays a vital role in various phases in the field development. Multiple seismic datasets are often acquired at different stages, from the exploration phase all the way to the enhanced oil recovery (EOR) phase. In general, different objectives are involved depending on whether a field is being explored, discovered, developed or produced. It is generally a good assumption that the level of geophysical requirements tends to be increasingly demanding as the field development progresses. Some examples are listed as:

- Structural definition: from low-order to high-order events going from regional, field-wide to inter-well scale
- Data usage: from post-stack, partial-stack to pre-stack
- Description of wavefield: from isotropic acoustic to anisotropic viscoelastic
- Characterization: from qualitative to quantitative properties
- Well placements: from vertical to complex trajectories
- Seismic-well tie: from fair correlation at a few control points to precise correlation at many control points.

For an exploration purpose, the main emphasis often lays on the extraction and delineation of prospects and/or leads to subsequently site exploration and delineation wells. For this purpose, relatively low-quality seismic images, even from 2D measurements, may already provide satisfactory information, such as the interpretation of major geological events. However, high-quality 3D seismic images are inevitably required at later stages, in mature fields, to provide detailed insight into subsurface properties.

The improved oil recovery (IOR) and EOR techniques have drawn considerable attention in the industry to expand the oil and gas production in existing reservoirs. Reservoir monitoring in the production stage is an aspect where geophysical approaches can play a significant role. Time-lapse seismic is an applicable and practical tool allowing us to obtain field-wide volumetric datasets at different moments in time without any data gap. Proper understanding of time-lapse seismic signatures then enables us to relate them to dynamic changes in reservoir properties due to production activities. Hence, detection of reliable time-lapse responses leads to a huge business impact on various aspects, including but not limited to increasing sweep efficiency by identifying fluid contacts and front, minimizing bypassed hydrocarbon by properly locating infill wells, obtaining optimum history matching and flow predictions by updating static and dynamic models, etc.

During the primary recovery stage, production behaviour is largely governed by natural mechanisms [44]. However, the first natural flow mechanisms normally cause more than half of the hydrocarbons to remain untouched in the reservoir. To extract hydrocarbons that are irrecoverable by intrinsic energy, other methods are chronologically applied after primary recovery. For example, an external fluid is injected to enhance hydrocarbon production via pressure maintenance and displacement of hydrocarbon by the injected fluid. Furthermore, the implementation of IOR/EOR technologies in a phased fashion surely add complexities in the recovery mechanism [45]. To properly and efficiently execute IOR/EOR operations, subtle and non-uniform reservoir sweep needs to be accurately captured. As fields become mature, the collection of high-resolution and high-density seismic datasets over the period of production contributes to improving the injection and production conformance. A successful deployment of seismic monitoring relies partially on the repeatability of detector and source positions between time-lapse measurements. Smit *et al.* [46] demonstrated that the normalized root mean square (NRMS) value [47] in the North sea surveys increases with the absolute value of detector positioning error plus source positioning error. Cabolova *et al.* [48] illustrated the advantages of monitor surveys at frequent intervals to disentangle timely injection and production behaviours.

The aforementioned increasing demands towards high-quality seismic data during the field development profile leads to the need for considerable investment in data acquisition. Meanwhile, there is also a continuous requirement in cost reduction. The acquisition of data in a compressed manner in space and time, e.g., via the application of blended acquisition and/or sparse geometries, has drawn considerable attention as the approach is capable of enhancing operational efficiency as well as data quality. Furthermore, the enhancement in the survey productivity contributes to minimizing HSE exposure in the field. While this way of data acquisition is widely accepted for structural imaging, few examples extend the technique to a time-lapse purpose. Krupovnickas

et al. [49] pointed out that subtle imperfection in deblending can hamper us from detecting the time-lapse signal which tends to employ much smaller amplitudes than primary reflections. Replication of acquisition geometries remains challenging particularly when time-lapse surveys are carried out in a blended and irregularly-sampled manner. Hence, it is worthwhile to investigate a strategy allowing us to properly realize the benefits of compressed data acquisition throughout the field development where replication of each vintage is no longer mandatory.

1.5. HSE IN SEISMIC OPERATIONS

The consideration and awareness towards HSE in a seismic survey have been increasingly recognized as essential factors determining a way to acquire seismic data. Bouska [3] and Nakayama *et al.* [5] described that blended acquisition both in land and marine cases does not require operational complexity; thus, standard and common practices used in a conventional, unblended fashion are sufficient for implementation without the need for any specialized equipment or procedure. Therefore, it is highly unlikely that the technique brings any major safety concerns to field operations, while significant minimization of the operational risk in the field is doubtlessly realizable with a shorter survey duration, especially in land, seabed and transition-zone acquisition, where adding extra sources introduces a subtle change in the overall cost. The deployment of fewer detectors and sources can also improve survey productivity without any complicated procedures. Therefore, the implementation of blending along with efficient acquisition geometries can lead to a potential reduction in HSE incidents in the field.

Furthermore, the implementation of certain blending codes such as the DSA concept is of help in contributing to an HSE perspective [9]. The emission of acoustic energy may incur a potential environmental risk, particularly in marine surveys. Sound pressure level and sound exposure level are of primary concern to determine the effects of an acoustic source on the marine environments, in particular on marine mammals [50]. Airgun clusters that generate an impulsive signal are widely used in the industry. As a broad frequency range of acoustic energy is instantaneously generated, the technique inevitably accentuates the peak pressure. Furthermore, these conventional marine sources inevitably emit high frequency components, e.g., above 100 Hz, which are normally discarded in seismic imaging yet significantly overlap with the hearing ranges of odontocetes and pinnipeds [50]. The use of dedicated narrow-band sources, e.g., via the DSA concept, decrease both the peak amplitude and the total energy for each shot. Properly designed blending codes potentially lead to preventing a seismic survey from the emission of unnecessary frequency components, while still acquiring the information needed to characterize the subsurface.

For these reasons, the design of data acquisition in a blended and sparsely-sampled fashion is of great help in minimizing HSE exposure in the field.

1.6. OBJECTIVES AND OUTLINE OF THESIS

This research, motivated by the aforementioned perspectives, aims at the following objectives:

- to develop an automated scheme to simultaneously optimize survey parameters

responsible for both source blending and spatial sampling of detectors and sources;

- to derive acquisition parameters that make the benefits of blending and irregular acquisition geometries realizable while attaining pre-set geophysical requirements, i.e., optimum deblending and data reconstruction quality as well as optimum estimates of subsurface properties;

- to explore a strategy for the application of compressed measurements through the field life.

In addition to the introductory part in **Chapter 1**, this thesis consists of the following chapters.

In **Chapter 2**, we describe the forward model of seismic data in terms of matrix operations in the frequency domain. We then illustrate the applicability of the model to various blending and spatial sampling schemes. We subsequently describe an iterative scheme to design survey parameters related to blending and spatial sampling of detectors and sources. The notation and representations as well as the assumptions given in this chapter are the fundamental basis of this thesis.

In **Chapter 3**, we demonstrate the implementation of the proposed survey design leading to satisfactory deblending and data reconstruction quality. Numerical examples representing different acquisition environments illustrate the applicability of the proposed approach. Additionally, we discuss practical and operational aspects of the method including a way to manage a trade-off between the survey cost and data quality.

In **Chapter 4**, we elaborate an iterative scheme to design the source blending and the spatial sampling of detectors and sources for direct reflectivity and velocity estimation. We use joint migration inversion (JMI) as a property estimation tool that iteratively derives a high-resolution subsurface reflectivity model as well as a migration velocity model [51, 52]. The numerical examples demonstrate that resultant survey parameters from the proposed approach lead to an enhanced JMI quality.

In **Chapter 5**, we explicitly focus on the application of blending and irregular sampling for different purposes and needs varying through the field life. We introduce a recovery scheme for time-lapse datasets, which is capable of sharing static elements among vintages while extracting dynamic changes according to prior subsurface information. Along with the virtue of the proposed recovery process, we examine the effect of survey parameters on the quality of recovered data and time-lapse signatures using real datasets.

In **Chapter 6**, we discuss the main research findings drawn from the thesis and provide recommendations for the future research directions.

The two appendixes provide detailed descriptions of joint deblending and data reconstruction and JMI respectively. It should be noted that the contents of this thesis are based on publications by the author [53–59].

REFERENCES

[1] C. J. Beasley, E. C. Ronald, and Z. Jiang, *A new look at simultaneous sources,* 68th SEG Annual Meeting, New Orleans, Louisiana, USA, Expanded Abstracts, 133 (1998).

[2] A. J. Berkhout, *Changing the mindset in seismic data acquisition,* The Leading Edge **27**, 924 (2008).

[3] J. Bouska, *Distance separated simultaneous sweeping, for fast, clean, vibroseis acquisition,* Geophysical Prospecting **58**, 123 (2010).

[4] R. Abma, Q. Zhang, A. Arogunmati, and G. Beaudoin, *An Overview of BP's Marine Independent Simultaneous Source field trials,* 82nd SEG Annual Meeting, Las Vegas, Nevada, USA, Expanded Abstracts, 1 (2012).

[5] S. Nakayama, G. Mercado, M. Benson, K. Belaid, and M. Garden, *Field-wide implementation of time and distance separated source techniques on a 3D OBC survey offshore Abu Dhabi, UAE,* First Break **33**, 47 (2015).

[6] F. J. Herrmann, *Randomized sampling and sparsity: Getting more information from fewer samples,* Geophysics **75**, WB173 (2010).

[7] C. C. Mosher, S. T. Kaplan, and F. D. Janiszewski, *Non-uniform optimal sampling for seismic survey design,* 74th EAGE Conference and Exhibition, Copenhagen, Denmark, Extended Abstracts **X034** (2012).

[8] A. J. Berkhout, *Blended acquisition with dispersed source arrays,* Geophysics **77**, A19 (2012).

[9] M. Caporal, G. Blacquière, and M. Davydenko, *Broadband imaging via direct inversion of blended dispersed source array data,* Geophysical Prospecting **66**, 942 (2018).

[10] J. Dellinger, A. Ross, D. Meaux, A. Brenders, G. Gesoff, J. Etgen, J. Naranjo, G. Openshaw, and M. Harper, *Wolfspar®, an "FWI-friendly" ultralow-frequency marine seismic source,* 86th SEG Annual Meeting, Dallas, Texas, USA, Expanded Abstracts, 4891 (2016).

[11] A. Mahdad, P. Doulgeris, and G. Blacquière, *Separation of blended data by iterative estimation and subtraction of blending interference noise,* Geophysics **76**, Q9 (2011).

[12] I. Moore, B. Dragoset, T. Ommundsen, D. Wilson, C. Ward, and D. Eke, *Simultaneous source separation using dithered sources,* 78th SEG Annual Meeting, Las Vegas, Nevada, USA, Expanded Abstracts, 2806 (2008).

[13] T. T. Y. Lin and F. J. Herrmann, *Designing simultaneous acquisitions with compressive sensing,* 71st EAGE Conference and Exhibition, Amsterdam, The Netherlands, Extended Abstracts **S006** (2009).

[14] A. Kontakis and D. J. Verschuur, *Combined focal and coherency-based deblending strategy,* 85th SEG Annual Meeting, New Orleans, Louisiana, USA, Expanded Abstracts, 4667 (2015).

[15] S. Xu, Y. Zhang, D. Pham, and G. Lambaré, *Antileakage Fourier transform for seismic data regularization,* Geophysics **70**, V87 (2005).

[16] G. Hennenfent and F. J. Herrmann, *Simply denoise: Wavefield reconstruction via jittered undersampling,* Geophysics **73**, V19 (2008).

[17] D. J. Verschuur, J. W. Vrolijk, and C. Tsingas, *4D reconstruction of wide azimuth (WAZ) data using sparse inversion of hybrid Radon transforms,* 82nd SEG Annual Meeting, Las Vegas, Nevada, USA, Expanded Abstracts, 1 (2012).

[18] H. Kutscha and D. J. Verschuur, *Data reconstruction via sparse double focal transformation: An overview,* IEEE Signal Processing Magazine **29**, 53 (2012).

[19] Y. Tang and B. Biondi, *Least-squares migration/inversion of blended data,* 79th SEG Annual Meeting, Houston, Texas, USA, Expanded Abstracts, 2859 (2009).

[20] D. J. E. Verschuur and A. J. Berkhout, *Seismic migration of blended shot records with surface-related multiple scattering,* Geophysics **76**, A7 (2011).

[21] A. J. Berkhout, G. Blacquière, and D. J. Verschuur, *Multiscattering illumination in blended acquisition,* Geophysics **77**, P23 (2012).

[22] Y. Chen, J. Yuan, S. Zu, S. Qu, and S. Gan, *Seismic imaging of simultaneous-source data using constrained least-squares reverse time migration,* Journal of Applied Geophysics **114**, 32 (2015).

[23] T. Nemeth, C. Wu, and G. T. Schuster, *Least-squares migration of incomplete reflection data,* Geophysics **64**, 208 (1999).

[24] A. Tarantola, *Inversion of seismic reflection data in the acoustic approximation,* Geophysics **49**, 1259 (1984).

[25] K. A. Florez, J. G. Mantilla, and A. B. Ramirez, *Full Waveform Inversion (FWI) in time for seismic data acquired using a blended geometry,* 2016 XXI Symposium on Signal Processing, Images and Artificial Vision (STSIVA), Bucaramanga, Colombia, 1 (2016).

[26] G. J. O. Vermeer, *3D Seismic Survey Design, Second Edition* (Society of Exploration Geophysicists, 2012).

[27] T. Ishiyama, G. Mercado, and K. Belaid, *3D OBC seismic survey geometry optimization offshore Abu Dhabi,* First Break **30**, 51 (2012).

[28] S. Nakayama, K. Belaid, and T. Ishiyama, *Seeking efficient OBC survey designs that still satisfy established geophysical objectives,* First Break **31**, 65 (2013).

[29] R. Baardman and R. van Borselen, *A simulated simultaneous source experiment in shallow waters and the impact of randomization schemes,* 83rd SEG Annual Meeting, Houston, Texas, USA, Expanded Abstracts, 4382 (2013).

[30] X. Campman, Z. Tang, H. Jamali-Rad, B. Kuvshinov, M. Danilouchkine, Y. Ji, W. Walk, and D. Smit, *Sparse seismic wavefield sampling,* The Leading Edge **36**, 654 (2017).

[31] J. R. Krebs, J. E. Anderson, D. Hinkley, R. Neelamani, S. Lee, A. Baumstein, and M.-D. Lacasse, *Fast full-wavefield seismic inversion using encoded sources,* Geophysics **74**, WCC177 (2009).

[32] C. Boonyasiriwat and G. T. Schuster, *3D Multisource Full-Waveform Inversion using Dynamic Random Phase Encoding,* 80th SEG Annual Meeting, Denver, Colorado, USA, Expanded Abstracts, 1044 (2010).

[33] H. Ben-Hadj-Ali, S. Operto, and J. Virieux, *An efficient frequency-domain full waveform inversion method using simultaneous encoded sources,* Geophysics **76**, R109 (2011).

[34] W. Jeong, S. Pyun, W. Son, and D.-J. Min, *A numerical study of simultaneous-source full waveform inversion with l1-norm,* Geophysical Journal International **194**, 1727 (2013).

[35] Y. Huang and G. T. Schuster, *Multisource least-squares migration of marine streamer and land data with frequency-division encoding,* Geophysical Prospecting **60**, 663 (2012).

[36] A. Aldawood, I. Hoteit, and T. Alkhalifah, *The possibilities of compressed-sensing-based Kirchhoff prestack migration,* Geophysics **79**, S113 (2014).

[37] C. Wang, D. Yingst, J. Brittan, P. Farmer, and J. Leveille, *Fast multi-parameter anisotropic full waveform inversion with irregular shot sampling,* 84th SEG Annual Meeting, Denver, Colorado, USA, Expanded Abstracts, 1147 (2014).

[38] A. Cordsen, M. Galbraith, and J. Peirce, *Planning Land 3-D Seismic Surveys* (Society of Exploration Geophysicists, 2000).

[39] C. J. Regone, *Using 3D finite-difference modeling to design wide-azimuth surveys for improved subsalt imaging,* Geophysics **72**, SM231 (2007).

[40] H. Jamali-Rad, B. Kuvshinov, Z. Tang, and X. Campman, *Deterministically subsampled acquisition geometries for optimal reconstruction,* 78th EAGE Conference and Exhibition, Vienna, Austria, Extended Abstracts **We STZ1 04** (2016).

[41] R. Abma and A. Ross, *Popcorn shooting: Sparse inversion and the distribution of airgun array energy over time,* 83rd SEG Annual Meeting, Houston, Texas, USA, Expanded Abstracts, 31 (2013).

[42] M. B. Mueller, D. F. Halliday, D. J. van Manen, and J. O. A. Robertsson, *The benefit of encoded source sequences for simultaneous source separation,* Geophysics **80**, V133 (2015).

[43] S. Wu, G. Blacquière, and G.-J. A. van Groenestijn, *Shot repetition: An alternative seismic blending code in marine acquisition,* Geophysics **83**, P43 (2018).

[44] M. Muskat, *Physical principles of oil production* (IHRDC, Boston, MA, 1981).

[45] J. Fink, *Petroleum engineer's guide to oil field chemicals and fluids* (Gulf Professional Publishing, 2015).

[46] F. Smit, J. Brain, and K. Watt, *Repeatability monitoring during marine 4D streamer acquisition,* 67th EAGE Conference and Exhibition, Madrid, Spain, Extended Abstracts (2005).

[47] E. D. Kragh and P. Christie, *Seismic repeatability, normalized rms, and predictability,* The Leading Edge **21**, 640 (2002).

[48] A. Cabolova, J. L. Lopez, and P. Wills, *Benefits of frequent seismic monitoring and computer simulations in thermal EOR projects,* 84th SEG Annual Meeting, Denver, Colorado, USA, Expanded Abstracts, 3513 (2014).

[49] T. Krupovnickas, K. Matson, C. Corcoran, and R. Pascual, *Marine simultaneous source OBS survey suitability for 4D analysis,* 82nd SEG Annual Meeting, Las Vegas, Nevada, USA, Expanded Abstracts, 1 (2012).

[50] B. L. Southall, J. J. Finneran, C. Reichmuth, P. E. Nachtigall, D. R. Ketten, A. E. Bowles, W. T. Ellison, D. P. Nowacek, and P. L. Tyack, *Marine mammal noise exposure criteria: updated scientific recommendations for residual hearing effects,* Aquatic Mammals **45**, 125 (2019).

[51] X. R. Staal and D. J. Verschuur, *Joint migration inversion, imaging including all multiples with automatic velocity update,* 75th EAGE Annual Meeting, London, UK, Extended Abstracts **Tu 02 16** (2013).

[52] A. J. Berkhout, *Review Paper: An outlook on the future of seismic imaging, Part III: Joint Migration Inversion,* Geophysical Prospecting **62**, 950 (2014).

[53] S. Nakayama, G. Blacquière, T. Ishiyama, and S. Ishikawa, *Blended-acquisition design with irregular geometries for wide-azimuth sampling,* 88th SEG Annual Meeting, Anaheim, California, USA, Expanded Abstracts, 126 (2018).

[54] S. Nakayama, G. Blacquière, T. Ishiyama, and S. Ishikawa, *Blended-acquisition design of irregular geometries towards faster, cheaper, safer and better seismic surveying,* Geophysical Prospecting **67**, 1498 (2019).

[55] S. Nakayama, G. Blacquière, and T. Ishiyama, *Automated survey-design for blended-acquisition with irregular spatial sampling via the integration of a metaheuristic and deep learning,* Geophysics **84**, P47 (2019).

[56] S. Nakayama, G. Blacquière, and T. Ishiyama, *Acquisition design for direct reflectivity and velocity estimation from blended and irregularly-sampled data,* Geophysical Prospecting **67**, 2127 (2019).

[57] S. Nakayama and G. Blacquière, *Automated Survey Design for Land Acquisition Using the Dispersed Source Array Concept,* New Advances in Land Geophysical Acquisition Technologies Workshop, Muscat, Oman (2019).

[58] S. Nakayama and G. Blacquière, *Simultaneous deblending and data reconstruction to supply proper time-lapse datasets throughout the field life in a cost-effective and efficient manner,* Geophysical Journal International **220**, 568 (2020).

[59] G. Blacquière and S. Nakayama, *Optimum seismic acquisition geometry design with the help of artificial intelligence,* 89th SEG Annual Meeting, San Antonio, Texas, USA, Expanded Abstracts, 117 (2019).

2

ACQUISITION DESIGN FRAMEWORK

This chapter reviews the notation used to describe seismic data in terms of matrix operations in the frequency domain. In this expression, the Earth's responses are surrounded by three operators. Two out of three operators are responsible for detector and source responses. The other is responsible for source blending such as information on source-to-be-blended and encoded source signatures. We provide matrix operations enabling us to formulate acquisition systems given by these three operators that we aim to design to properly retrieve subsurface properties. We then cast the design of these three operators as a minimization problem that we solve in an iterative way. The proposed method makes use of prior subsurface information. At each iteration, a quality measure is computed for a given survey design, which is subsequently assigned as its objective function. This information is then used to update the survey parameters by integrating a genetic algorithm and a convolutional neural network. Bio-inspired stochastic operators enable the simultaneous update of the blending and sampling parameters. To relate the choice of survey parameters to the result of a given quality measure, we utilize the convolutional neural network. The applied network architecture is designed to reject suboptimal solutions among newly generated ones from genetic operators. Consequently, only optimal ones are fed into the subsequent, expensive residue evaluation step. Furthermore, the solution space is limited via a repeated encoding sequence that combines a set of short binary vectors, each having a random-like feature to form a long parameter sequence representing blending and sampling operators. The proposed approach updates survey parameters for improvement of the data quality at a computationally affordable time under given practical constraints. The proposed implementation does not necessarily guarantee the global optimum. Nevertheless, in our application, this is fully acceptable as long as the residue satisfies the pre-set criterion.

Parts of this chapter are available in references [1–4].

2.1. BLENDING AND SPATIAL SAMPLING

Using the matrix notation in the **WRW** model (**W** stands for wave propagation and **R** for reflection) proposed by Berkhout [5], we describe monochromatic seismic data, recorded by detectors at depth z_d for sources at z_s, as:

$$\mathbf{P}(z_d; z_s) = \mathbf{D}(z_d)\mathbf{X}(z_d, z_s)\mathbf{S}(z_s). \tag{2.1}$$

Each column and row of data matrix $\mathbf{P}(z_d; z_s)$ represent a shot and detector gather, respectively. For example, vectors corresponding to the j^{th} shot and i^{th} detector gathers are written as $\vec{P}_j$ and $\vec{P}_i^{\dagger}$ where the dagger symbol (†) represents a row vector. A collection of $\mathbf{P}(z_d, z_s)$ matrices for each frequency enables us to form a 3D data matrix. $\mathbf{D}(z_d)$ and $\mathbf{S}(z_s)$ are the detector and source matrix, respectively. Columns and rows in $\mathbf{D}(z_d)$ correspond to spatial coordinates and detector arrays, respectively, whereas columns and rows in $\mathbf{S}(z_s)$ correspond to source arrays and spatial coordinates, respectively. Matrix $\mathbf{X}(z_d, z_s)$ is the Earth's transfer function containing single frequency components of the subsurface impulse responses. It can be also regarded as unblended data with perfect spatial sampling. Amplitude and phase information for a given frequency are embedded into each element of each matrix. In the following, we assume the sources and detectors to be located at the same depth, i.e., $z_s = z_d = z_0$. This model refers to the situation where the response of each source is recorded by the all the detectors.

According to [6], $\mathbf{X}(z_0, z_0)$ can be approximated by:

$$\mathbf{X}(z_0, z_0) = \sum_{m=1}^{M_{\text{d}}} \underset{\sim}{\mathbf{W}}^{-}(z_0, z_m)\mathbf{R}^{\cup}(z_m)\underset{\sim}{\mathbf{W}}^{+}(z_m, z_0), \tag{2.2}$$

with

$$\begin{aligned} \underset{\sim}{\mathbf{W}}^{-}(z_0, z_m) &= \mathbf{W}^{-}(z_0, z_1)\prod_{n=1}^{m-1}[\mathbf{I} + \delta\mathbf{T}^{-}(z_n)]\mathbf{W}^{-}(z_n, z_{n+1}), \\ \underset{\sim}{\mathbf{W}}^{+}(z_m, z_0) &= \mathbf{W}^{+}(z_m, z_{m-1})\prod_{n=m-1}^{1}\left[\mathbf{I} + \delta\mathbf{T}^{+}(z_n)\right]\mathbf{W}^{+}(z_n, z_{n-1}), \end{aligned} \tag{2.3}$$

where $\mathbf{W}^{-}(z_n, z_{n+1})$ and $\mathbf{W}^{+}(z_n, z_{n-1})$ account for the upward and downward propagation, respectively, between consecutive depth levels. They are transposed versions of each other. Parameter M_{d} indicates the number of depth levels. Matrix $\mathbf{R}^{\cup}(z_m)$ is the down-up reflectivity operator responsible for scattering at depth z_m. Terms $\left[\mathbf{I} + \delta\mathbf{T}^{\mp}(z_n)\right]$ are the upward and downward transmission operators at depth z_n, respectively. Hence, matrices $\underset{\sim}{\mathbf{W}}^{\mp}$ include both propagation and transmission effects. The approximations given by Equations 2.2 and 2.3 neglect internal multiples, while it is also possible to incorporate their responses via the so-called full wave field modelling [6]. According to [6], the assumption of angle and frequency independent reflectivity along with small shear contrast allows for the following approximations to be used:

$$\begin{aligned} &\mathbf{R}^{\cup}(z_m) \approx -\mathbf{R}^{\cap}(z_m) \approx \mathbf{R}(z_m), \\ &\delta\mathbf{T}(z_m)^{\mp} \approx \mp\mathbf{R}(z_m), \end{aligned} \tag{2.4}$$

where $\mathbf{R}^{\cap}(z_m)$ is the up-down reflectivity operator, and $\mathbf{R}(z_m)$ is a diagonal matrix containing the angle and frequency independent reflectivity coefficients. For notational

simplicity, detector and source depth indices are hereinafter omitted, except for Appendix B.

With the use of a point detector (rather than a detector array), the distribution of zero and non-zero elements in **D** dictates the spatial sampling of detectors. Information embedded into non-zero elements is attributable to responses of the sensor and recording system used in a given acquisition system. Similarly, with a point source, the distribution of zero and non-zero elements in **S** dictates the spatial sampling of the sources. Information embedded into non-zero elements is attributable to the source signature. Since our primary focus is on the effect of spatial sampling, we make the assumption of delta-functioned detector and source responses, where elements of **D** and **S** become either zero or one. Each row of **D** corresponds to the lateral location of a detector. If some detectors are missing, the number of rows in **D** becomes less than the number of columns. Similarly, each column of **S** corresponds to the lateral location of a source. If some shots are missing, the number of columns in **S** becomes less than the number of rows. Hence, the zero and non-zero elements in **D** and **S** are simply attributed to detector and source locations, respectively.

In an ideal situation, i.e., carpet detectors and sources, **D** and **S** are identity matrices that keep all the responses in **X**. In this case, **P** simply equates to **X** (see Equation 2.1). Figure 2.1a exemplifies a matrix representation of an ideal dataset **X**. Dots indicate seismic responses recorded by densely distributed detectors and sources along the acquisition surface. Unfortunately, this situation is hardly realizable due mainly to budgetary and operational constraints. Any imperfections related to the spatial sampling then hinder **P** from resembling **X**. In practice, data matrix **P** becomes a subset of **X** according to **D** and **S**. Some practical situations are illustrated in Figures 2.1b-d.

As mentioned previously, Equation 2.1 is only capable of describing stationary acquisition geometries. However, it is incapable of describing non-stationary acquisition geometries such as a towed-streamer survey. Furthermore, land and sea-bed acquisition often employ rolls of a template geometry, involving detector deployment and retrieval during the field operation. Blacquière and Nakayama [4] introduced a non-linear operator, $\mathscr{M}_{\mathbf{D},\mathbf{S}}$, to describe seismic data **P** acquired by practical acquisition geometries:

$$\mathbf{P} = \mathscr{M}_{\mathbf{D},\mathbf{S}}[\mathbf{X}], \tag{2.5}$$

where $\mathscr{M}_{\mathbf{D},\mathbf{S}}$ clears the responses from **X** which are not acquired by the current acquisition geometry and leaves only the recorded ones. This expression is applicable to both stationary and non-stationary geometries. Figures 2.1e and f show examples of matrix representations for non-stationary geometries which can be described by $\mathscr{M}_{\mathbf{D},\mathbf{S}}$.

Equations 2.1 and 2.5 indicate that **P** is a subset of **X**. In practice, the size of **P** is much smaller than the size of **X** as it contains numerous zero elements and potentially hinders us from extracting essential subsurface information. Therefore, we need to pay proper attention to the distribution of detectors and sources in order for subsequent process(es) to be able to retrieve **X** from **P**, which is our goal.

Berkhout [7] proposed the theoretical framework of source blending by introducing a blending operator, $\mathbf{\Gamma}$:

$$\mathbf{S}' = \mathbf{S}\mathbf{\Gamma}, \tag{2.6}$$

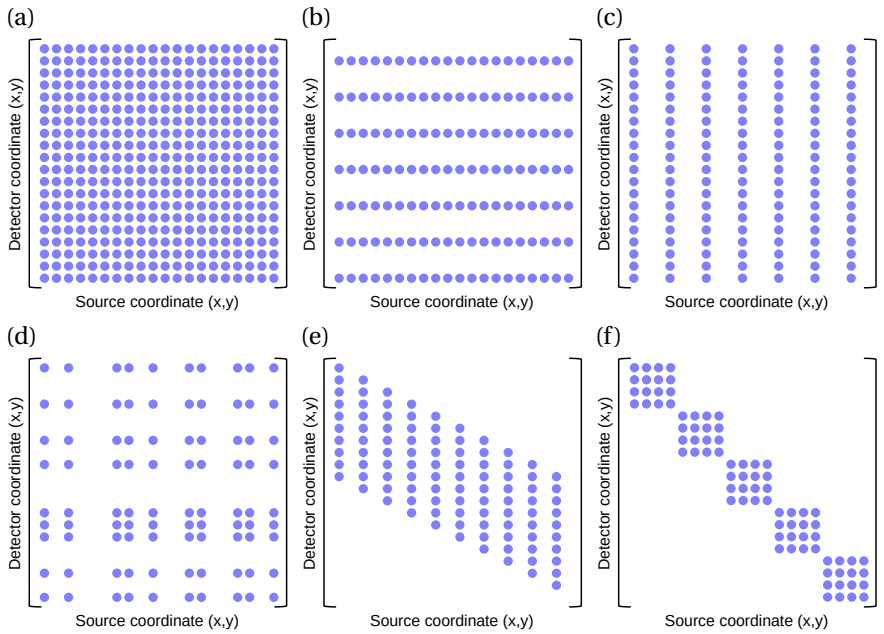

Figure 2.1: Matrix representations of seismic data with different geometries. (a) Ideal acquisition geometry, i.e., carpet detectors and carpet sources, representing **X**. (b) Regular acquisition geometry with sparsely-sampled detectors and densely-sampled sources. (c) Regular acquisition geometry with densely-sampled detectors and sparsely-sampled sources. (d) Irregular acquisition geometry with sparsely-sampled detectors and sparsely-sampled sources. (d) Non-stationary acquisition geometry, e.g., a towed-streamer configuration. (e) Non-stationary acquisition geometry, e.g., rolls of a template acquisition geometry.

where $\mathbf{S}'$ represents the blended source matrix. Each column and row of $\mathbf{\Gamma}$ correspond to a shot experiment and a location of a source-to-be-blended, respectively. Each element of $\mathbf{\Gamma}$ contains the blending code(s) such as phase and amplitude terms, applied to the corresponding source. With N-fold blended sources, i.e., N sources are blended in one blended experiment leading to one blended shot record, the blending codes of N source units are stored in one column of $\mathbf{\Gamma}$. Linearly summing the wavefields of those individual sources forms one blended source wavefield. Figure 2.2 illustrates matrix representations before and after the application of $\mathbf{\Gamma}$ in the case of two-fold blended sources.

From Equations 2.1 and 2.6, blended and spatially sampled data can be written as:

$$\mathbf{P}' = \mathbf{D}\mathbf{X}\mathbf{S}' = \mathbf{D}\mathbf{X}\mathbf{S}\mathbf{\Gamma} = \mathbf{P}\mathbf{\Gamma}. \tag{2.7}$$

Blacquière and Nakayama [4] then rewrote Equation 2.7 using $\mathscr{M}_{\mathbf{D},\mathbf{S}}$ to accommodate both stationary and non-stationary geometries as:

$$\mathbf{P}' = \mathscr{M}_{\mathbf{D},\mathbf{S}}[\mathbf{X}]\mathbf{\Gamma}. \tag{2.8}$$

Equations 2.7 and 2.8 imply that, starting with an unblended and regularly well-sampled dataset **X**, a dataset $\mathbf{P}'$ containing any blending and spatial sampling schemes can be

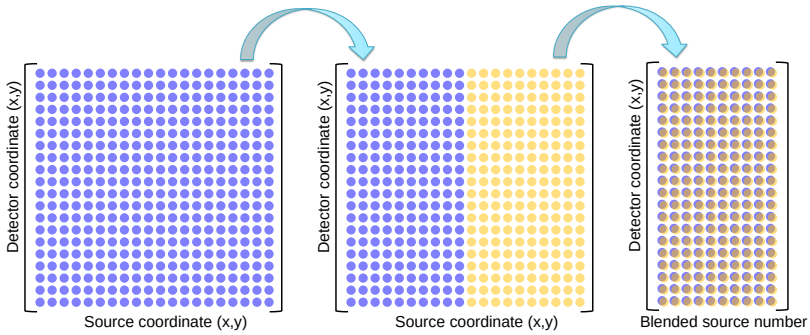

Figure 2.2: Application of blending operator to data matrix in the case of two-fold blended sources. Colours differentiate data acquired by two different sources which are blended according to $\mathbf{\Gamma}$. It should be noted that this exemplifies one of many possible cases for two-fold blending.

modelled by applying $\mathbf{D}$, $\mathbf{S}$ (or $\mathscr{M}_{\mathbf{D},\mathbf{S}}$) and $\mathbf{\Gamma}$. Figure 2.3 depicts matrix representations before and after the application of spatial sampling and blending operators. The change in the size of matrices can be translated to the amount of cost and time that we can potentially save.

As discussed previously, when designing $\mathbf{D}$, $\mathbf{S}$ (or $\mathscr{M}_{\mathbf{D},\mathbf{S}}$), our choices are limited to either clearing or leaving traces in $\mathbf{X}$. On the other hand, many choices are available to design $\mathbf{\Gamma}$. In a linear system, one element of the blending operator $\mathbf{\Gamma}$ for frequency ω is given by:

$$\gamma_{i,j} = a_{i,j}(\omega)\, e^{-j\,\phi_{i,j}(\omega)}, \tag{2.9}$$

where $a_{i,j}$ is the amplitude term corresponding to the i^{th} source of the j^{th} blended experiment, and $\phi_{i,j}$ is its phase. Many types of source code can be accommodated in Equation 2.9. In the case that the blending codes are time delays $\tau_{i,j}$, the corresponding phase can be written as $\phi_{i,j} = \omega\tau_{i,j}$. Figures 2.4b-h show different encoded source signatures, derived from a base wavelet shown in Figure 2.4a . In addition to a time delay, Equation 2.9 allows us to simulate various signatures such as band limitation, phase modulation, shot repetition [8], encoded sweeping [9], band limitation and popcorn shooting [10]. Note that the dispersed source array (DSA) concept [11], where the total blended wavefield is generated by a plurality of narrow-band sources with different centre frequencies, is also described by Equation 2.9 (albeit implicitly as the equations are formulated in the frequency domain). It should be noted that this dissertation focuses mainly on stationary acquisition geometries. This means that hereinafter we use Equation 2.7 rather than Equation 2.8. We, therefore, use $\mathbf{D}$ and $\mathbf{S}$ to describe the spatial locations of detectors and sources.

2.2. ITERATIVE ACQUISITION DESIGN SCHEME

2.2.1. OVERALL WORKFLOW

Nakayama *et al.* [1] introduced an iterative scheme to optimize survey parameters $\mathbf{D}$, $\mathbf{S}$ and $\mathbf{\Gamma}$ that can satisfy a pre-set geophysical criterion. They used the technique to derive

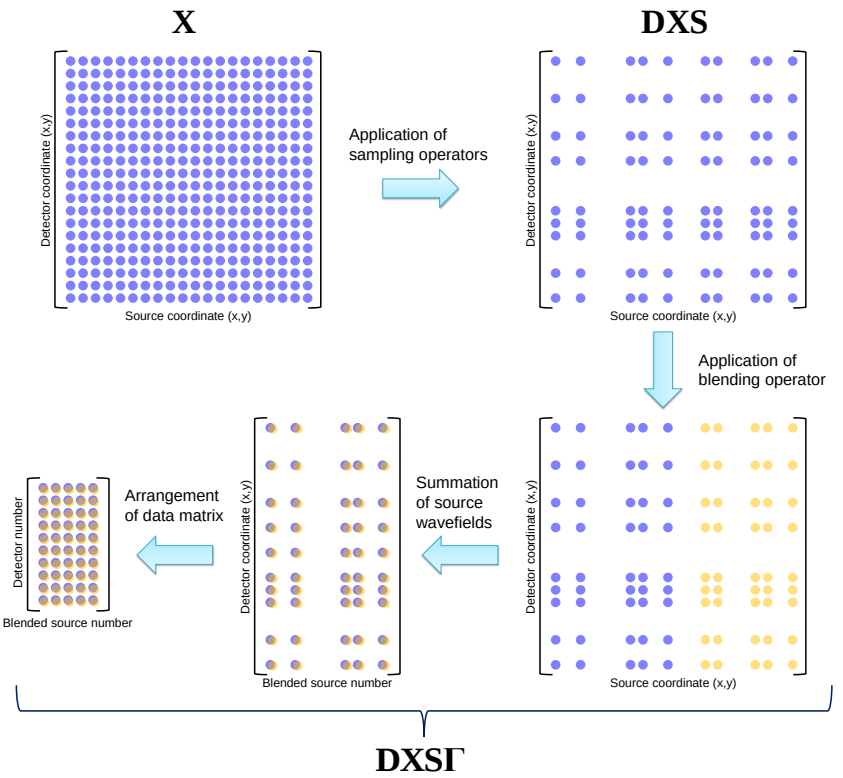

Figure 2.3: Application of sampling and blending operators to **X**. The sampling operators clear traces and the blending operator sums source wavefields. A significant reduction of the size of the data matrix is attainable by applying these operators, leading to an enhancement of survey efficiency.

acquisition scenarios, leading to optimum deblending and data reconstruction quality. This approach was further extended by [2, 12]. Additionally, Blacquière and Nakayama [4] summarized a central idea of our survey design.

Figure 2.5 is a schematic illustrating the proposed survey design workflow. Based on available subsurface knowledge, the workflow starts with simulating the desired dataset, e.g., unblended and well-sampled data via the use of finite-difference modelling. We assume certain subsurface information to be accessible, e.g., at a development or production stage, or when data from a previous acquisition and appropriate well logs are available. If such information is available, we make use of prior knowledge to design survey parameters. Availability of prior subsurface information is often considered as a valid assumption to design a seismic survey. In a simple case, knowledge of target depth levels in the area of interest is used to determine an offset coverage. We can also evaluate the illumination capabilities of different acquisition designs through ray tracing by assuming that the velocity field is known [13]. As mentioned previously, Regone [14] performed finite-difference modelling using a given subsurface model to generate a set of

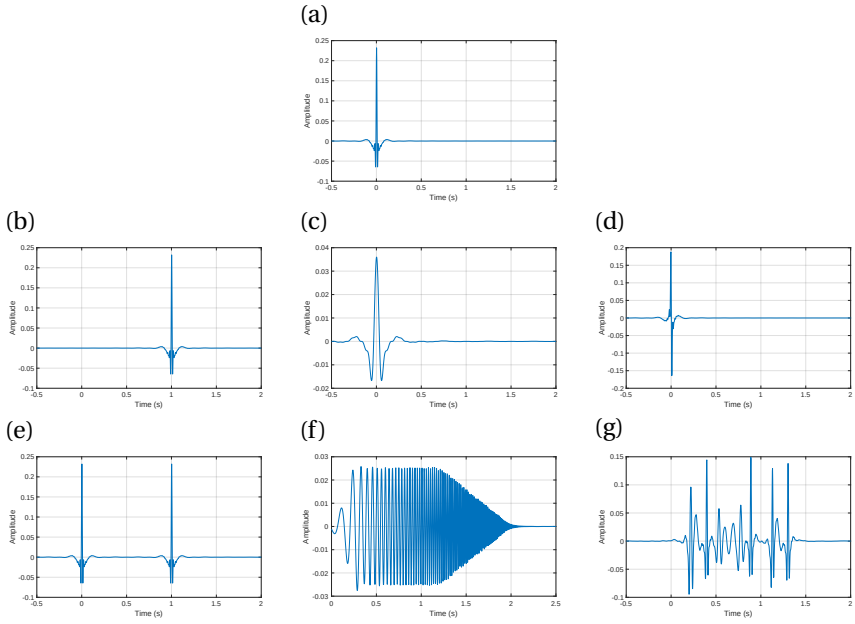

Figure 2.4: Encoded source signatures. (a) Base wavelet. (b) Time shift. (c) Band limitation. (d) Phase rotation. (e) Shot repetition. (f) Sweep. (g) Popcorn source.

simulated data, representing different survey designs, and processed them to determine the optimum acquisition parameters.

The blue-filled step in Figure 2.5 corresponds to the forward process to generate $\mathbf{P}'$ using $\mathbf{D}$, $\mathbf{S}$ and $\mathbf{\Gamma}$ as well as the desired dataset, i.e., $\mathbf{X}$. The red-filled step then represents the user-defined process(es) to generate estimate(s). The overall scheme aims at finding survey parameters that can minimize the objective function based on the residue between the ideal output and the estimated one. If the objective function is sufficiently small, or the maximum number of iterations is exceeded, the procedure stops. If not, we simultaneously update spatial sampling and blending schemes that are subsequently fed into the next iteration.

2.2.2. SURVEY PARAMETER UPDATE

According to [15], the relevant and conventional parameters to design seismic surveys are the four spatial intervals and four apertures of the acquisition template, i.e., detector and source intervals as well as detector and source apertures, each in the two perpendicular directions. In a conventional way, the aforementioned parameters sufficiently describe how seismic data are acquired. On the other hand, as described previously, incorporating irregularity into survey parameters is a key to design blended acquisition with efficient spatial sampling. Despite the potential benefits of blending with sparse and irregular geometries, the implementation of these techniques likely requires an extra effort. Unlike a conventional survey acquired in a regular fashion, irregularity inher-

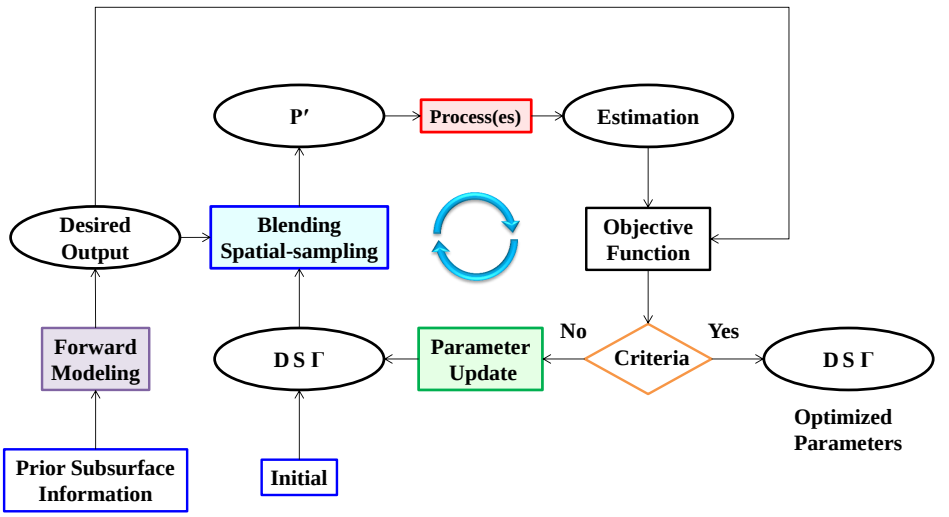

Figure 2.5: Iterative scheme for designing acquisition parameters. Prior subsurface information is used to model the ideal seismic data. This dataset is turned into practical seismic data by applying a certain acquisition geometry. The data from this geometry is processed, and the resulting subsurface image is evaluated by comparing it with the prior subsurface information. The difference between the two is the objective function to be minimized. If the result is satisfactory, the final acquisition geometry has been obtained. If not, the procedure is repeated with an updated acquisition geometry.

ently makes the parameter selection problem extremely large and complex. To handle this, Nakayama *et al.* [1, 16] presented a survey design scheme utilizing a genetic algorithm (GA), which allows for optimization of blending and spatial sampling schemes simultaneously rather than sequentially.

GAs are classified as a metaheuristic and are generally capable of handling optimization problems with nonconvexity, the existence of many local minima, nondifferentiability and large problem space. GAs are inspired by biological evolution through the process of natural selection. The latter was first introduced in "On The Origin of Species" by [17], which describes the biological development of species and survival of minor advantageous mutations. Holland [18] originated the concept of GAs and demonstrated how the theory of evolution can be exploited for optimization problems based on binary string representations. Such strings are considered as biological chromosomes, and evolution processes are described in the natural selection such as mutation, selection and crossover. Over several decades, the original definition of GAs has gradually evolved, and the technology has been widely adapted to a variety of optimization problems. Numerous successful applications of GAs are easily recognizable in different domains such as biomedicine [19], arts [20], architecture [21], music [22], games [23] and recently machine learning [24].

Despite the advantages of GAs in solving various optimization problems including survey design, the technique inherently and inevitably evaluates all the candidate solutions to obtain their objective function values. The evaluation of suboptimal solutions, which do not contribute to the next generation, makes its implementation computationally expensive. To efficiently use the computational resources, we integrate a convolutional neural network (CNN) into our GA [2, 12]. Figure 2.6 and Algorithm 1 focus on the proposed implementation to update survey parameters, which also corresponds to the green box in Figure 2.5. The GA iteratively updates **D**, **S** and **Γ** that constitute of a set of parameter vectors:

$$\vec{C}_{g,p} = \left[\vec{d}_{g,p}, \vec{s}_{g,p}, \vec{\gamma}_{g,p}\right]^T, \tag{2.10}$$

with

$$\vec{d}_{g,p} \in \{0,1\}^{l_\mathrm{d}}, \quad \vec{s}_{g,p} \in \{0,1\}^{l_\mathrm{s}}, \quad \vec{\gamma}_{g,p} \in \{0,1\}^{l_s \times l_\mathrm{g}}. \tag{2.11}$$

Here, g and p represent indices of generation and population, and $\vec{d}_{g,p}$, $\vec{s}_{g,p}$ and $\vec{\gamma}_{g,p}$ are binary vectors indicating detector sampling, source sampling and blending operators for the p^{th} individual solution in the g^{th} generation that we aim to update through stochastic operators in the GA. The dimensions of the parameter vectors are indicated by l_d, l_s and l_g. Terms l_d and l_s equate to the numbers of available detector grids and source grids in the ideal data **X** to be designed for the geometry under consideration. With the use of the delta-functioned detector response, a distribution of zeros and ones in $\vec{d}_{g,p}$ represents the presence and absence of detectors in the corresponding locations. Similarly, with the use of the delta-functioned source response, a distribution of zeros and ones in $\vec{s}_{g,p}$ represents the presence and absence of sources in the corresponding locations. Hence, **D** and **S** can be simply obtained by binary strings. Binary vector $\vec{\gamma}_{g,p}$ represents the blending operator for the p^{th} individual solution in the g^{th} generation.

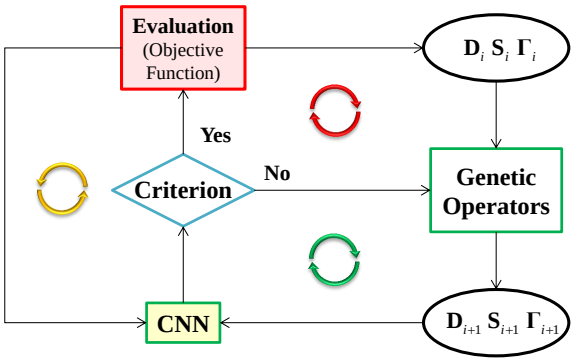

Figure 2.6: The scheme to update survey parameters. Steps within the green loop correspond to the green box in Figure 2.5. Genetic operators update **D**, **S** and **Γ** simultaneously. Newly generated parameters then go to the CNN. Survey parameters are regenerated until the classification result meets the criterion. Only selected solutions go to the evaluation that involves the actual computation of objective functions. Designs having smaller objective function values form a new generation. The evaluation results are also used to train the CNN used for the classification step in the next iteration.

Term l_g is equal to the required bit length to parametrize a given blending code per single source. In the case of time dither, a decimal number that indicates a time delay applied to a corresponding shot is converted from a binary string with length of l_g, which is subsequently used to derive **Γ** using Equation 2.9. The following steps describe the implementation of the technique to our survey design.

Let n_g and n_p represent the total numbers of generations and populations. The population in the g^{th} generation, $\vec{C}_g$, consists of a set of parameter vectors, having n_p individuals, as:

$$\vec{C}_g = \begin{bmatrix} \vec{C}_{g,1} \\ \vec{C}_{g,2} \\ \vdots \\ \vec{C}_{g,n_p} \end{bmatrix}. \tag{2.12}$$

The first step of the proposed scheme is to randomly generate the initial population, $\vec{C}_0$, across a given problem space as:

$$\vec{C}_0 = \begin{bmatrix} \vec{C}_{0,1} \\ \vec{C}_{0,2} \\ \vdots \\ \vec{C}_{0,n_p} \end{bmatrix} = \begin{bmatrix} \left[\vec{d}_{0,1}, \vec{s}_{0,1}, \vec{\gamma}_{0,1}\right]^T \\ \left[\vec{d}_{0,2}, \vec{s}_{0,2}, \vec{\gamma}_{0,2}\right]^T \\ \vdots \\ \left[\vec{d}_{0,n_p}, \vec{s}_{0,n_p}, \vec{\gamma}_{0,n_p}\right]^T \end{bmatrix}. \tag{2.13}$$

Each parameter vector in the initial population, $\vec{C}_{0,p}$, then goes to the forward process to derive $\mathbf{P}'_{0,p}$ by applying the survey parameters of the p^{th} individual solution in the initial

generation, ($\mathbf{D}_{0,p}$, $\mathbf{S}_{0,p}$ and $\mathbf{\Gamma}_{0,p}$), to the desired data. Then, a set of objective functions for the initial population, $\vec{J}_0$, can be obtained:

$$\vec{J}_0 = \left[J_{0,1}, J_{0,2}, \ldots, J_{0,n_\mathrm{p}}\right]^T. \tag{2.14}$$

Using $\vec{C}_0$ and $\vec{J}_0$, we train the CNN where we derive the predictive model that can relate the performance of a given estimation process to the choice of survey parameters. After the initial iteration, the CNN is embedded into our GA. It aims to classify whether survey parameters for a given design can satisfy a predetermined threshold based on the objective function. Until this criterion is met, genetic operators repeatedly produce new survey parameters which are subsequently evaluated by the CNN. As mentioned, its task is to exclude individual solutions that are unlikely to satisfy the predetermined threshold criterion for proceeding to the next generation. Although a deeper and more complex network would presumably enable us to directly input $\mathbf{D}$, $\mathbf{S}$ and $\mathbf{\Gamma}$ into the CNN, for now, this helps to obtain acceptable classification results in an efficient manner.

To minimize the objective function, the following genetic operators iteratively update $\mathbf{D}$, $\mathbf{S}$ and $\mathbf{\Gamma}$. To assign more weight to a solution with a smaller misfit, an expected selection probability of each individual solution according to its objective function is computed as:

$$G(\vec{C}_{g,p}) = j_{g,p} / \sum_{j=1}^{n_\mathrm{p}} j_{g,j}, \tag{2.15}$$

with

$$j_{g,p} = \exp(-\beta J_{g,p} / \max_{j \in n_\mathrm{p}} J_{g,j}), \tag{2.16}$$

where β is a scaling factor that defines the diversity in the selection. According to the selection probabilities of the individuals, parental solutions, fed into crossover and mutation operations, are defined via a roulette wheel selection. Crossover combines two parental solutions to generate two offspring solutions. Since $\vec{d}$, $\vec{s}$ and $\vec{\gamma}$ employ different lengths and constraints, crossover among different vectors is inadequate. Hence, a single crossover is applied to each binary vector. For further refinement of each parameter vector, mutation then applies local and random modifications on a single parental solution according to a mutation rate determined by parameter testing. Newly generated solutions are evaluated using the CNN trained in the previous iteration. As described previously, we utilize the technique to classify solutions according to their likelihood to pass the predefined threshold based on the objective function value. Genetic operators regenerate solutions until all the candidates in a given generation pass the criterion in the CNN.

Next, these solutions go to the evaluation process to derive a set of objective functions:

$$\vec{J}_g = \left[J_{g,1}, J_{g,2}, \ldots, J_{g,n_\mathrm{p}}\right]^T. \tag{2.17}$$

We combine $\vec{C}_g$ with the solutions obtained from generations 0 to $g-1^{\mathrm{th}}$, $\vec{C}_{0:g-1}$, and $\vec{J}_g$

with the objective functions from generations 0 to $g-1^{\text{th}}$, $\vec{J}_{0:g-1}$, as:

$$\vec{C}_{0:g} = \left[\vec{C}_{0:g-1}, \vec{C}_g\right]^T = \left[\vec{C}_0, \ldots, \vec{C}_g\right]^T, \tag{2.18}$$

and

$$\vec{J}_{0:g} = \left[\vec{J}_{0:g-1}, \vec{J}_g\right]^T = \left[\vec{J}_0, \ldots, \vec{J}_g\right]^T. \tag{2.19}$$

The best solutions in $\vec{C}_{0:g}$ are selected on the basis of the elitism to replace $\vec{C}_g$. This permits some better solutions in the previous generations to be still preserved in the new generation.

After obtaining $\vec{C}_{0:g}$ and $\vec{J}_{0:g}$, we train the CNN to update the predictive model derived from the $g-1^{\text{th}}$ generation. We apply an N-fold cross-validation to evaluate the predictive classifier. The procedure randomly splits all the samples into N subsets with equal size. One of the N subsets is used as a testing set, whereas the remaining $N-1$ subsets are assembled to form a training set. This process is repeated N times by alternately using every subset for testing and the remaining subsets for training. This interchange enables all the samples to be used for training as well as for testing. The mean of the prediction errors along with the variance among the N trials indicates the predictive performances of the classifiers. The best of the N models is applied to the next iteration. At each generation, the threshold criterion applied in the classification is updated, starting from a mild value and moving to a harsh one. To improve the stability of the CNN, we modify the number of epochs and the strength of the L2-regularization term applied to every weight in the network through the course of the iterations. The former parameter is increased, while the latter is decreased with the number of iterations. Controlling them is considered as an effective and simple means to prevent overfitting [25]. It is worth noting that the update of survey parameters is based primarily on the evaluation of the objective function, while the CNN classifier has a supporting role in the proposed scheme. Its role is to enhance the computational efficiency by reducing the number of iterations.

The iterative procedure stops when the objective function is sufficiently small, or when the number of generations reaches the pre-defined number of generations n_{g}. It should be noted that various constraints on the blending and sampling operators can be imposed within the genetic operators in order to prevent the generation of any undesired solutions, such as operationally infeasible designs. It is also noteworthy that the proposed optimization scheme is not a mandated choice as our workflow can accommodate different methods. Both metaheuristics and neural networks can be flexibly modified and designed, enabling us to adapt them for a problem-specific task. Therefore, a user can freely select a preferred framework for a given survey design problem.

2.2.3. INTEGRATION OF METAHEURISTIC AND NEURAL NETWORKS

A number of studies have shown the integration of metaheuristics and neural networks. In spite of recent successes in neural networks [26–28], advanced architectures have become deeper and more complex. Designing network architectures is still a challenging task due to the existence of numerous parameters. In this respect, a typical approach is to explore and design efficient network architectures using GAs [29, 30]. The other way around, Kramer [24] outlined ways to support and accelerate evolutionary algorithms

Algorithm 1 Acquisition design workflow

Input: Desired output

Output: $\vec{C}_{0:n_\mathrm{g}}$ $(= \left[\vec{C}_0, \ldots, \vec{C}_{n_\mathrm{g}}\right]^T)$ and $\vec{J}_{0:n_\mathrm{g}}$ $(= \left[\vec{J}_0, \ldots, \vec{J}_{n_\mathrm{g}}\right]^T)$

Set n_g and n_p $(= n_\mathrm{c} + n_\mathrm{m})$
Generate initial population, $\vec{C}_0$ $(= \left[\vec{C}_{0,1}, \ldots, \vec{C}_{0,n_\mathrm{p}}\right]^T)$
for $g = 0 \rightarrow n_\mathrm{g}$ **do**
  if $g = 0$ **then**
    $\vec{C}_{0:g-1} = \emptyset$ and $\vec{J}_{0:g-1} = \emptyset$
  else
    Compute selection probability of each solution in $\vec{C}_{g-1}$
    for $p = 1 \rightarrow n_\mathrm{c}/2$ **do**
      while stopping criterion not met **do**
        Select two parental solutions from $\vec{C}_{0:g-1}$ using roulette wheel selection
        Perform crossover operation to generate $\vec{C}_{g,2p-1}$ and $\vec{C}_{g,2p}$
        Evaluate $\vec{C}_{g,2p-1}$ and $\vec{C}_{g,2p}$ with the CNN trained from $g-1^{\mathrm{th}}$ generation
      end while
    end for
    for $p = n_\mathrm{c} + 1 \rightarrow n_\mathrm{p}$ **do**
      while stopping criterion not met **do**
        Select one parental solution from $\vec{C}_{0:g-1}$ using roulette wheel selection
        Perform mutation operation to generate $\vec{C}_{g,p}$
        Evaluate $\vec{C}_{g,p}$ with the CNN trained from $g-1^{\mathrm{th}}$ generation
      end while
    end for
  end if
  for $p = 1 \rightarrow n_\mathrm{p}$ **do**
    Generate $\mathbf{D}_{g,p}$, $\mathbf{S}_{g,p}$ and $\mathbf{\Gamma}_{g,p}$ from $\vec{C}_{g,p}$ $(= \left[\vec{d}_{g,p}, \vec{s}_{g,p}, \vec{\gamma}_{g,p}\right]^T)$
    Generate $\mathbf{P}'_{g,p}$ using $\mathbf{D}_{g,p}$, $\mathbf{S}_{g,p}$ and $\mathbf{\Gamma}_{g,p}$
    Derive estimate(s) and compute the objective function, $J_{g,p}$
  end for
  Update $\vec{C}_{0:g}$ $(= \left[\vec{C}_{0:g-1}, \vec{C}_g\right]^T)$ and $\vec{J}_{0:g}$ $(= \left[\vec{j}_{0:g-1}, \vec{j}_g\right]^T)$
  Train the CNN using $\vec{C}_{0:g}$ and $\vec{J}_{0:g}$
  Sort $\vec{C}_{0:g}$ based on the elitism to derive the fittest population, $\vec{C}_g$
end for

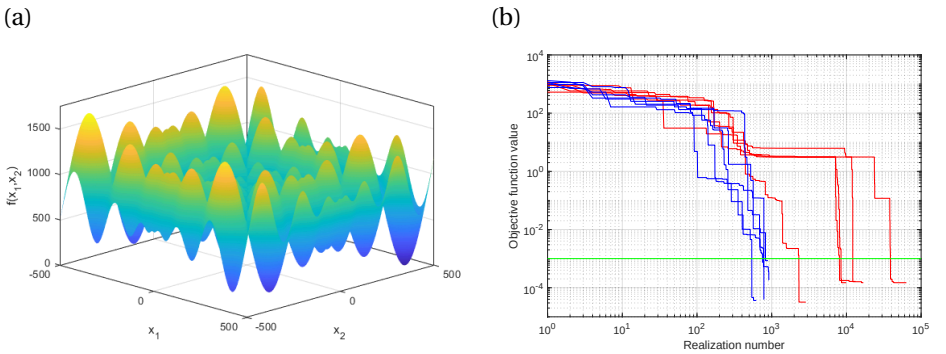

Figure 2.7: Benchmark test using 2D Schwefel Function. (a) 2D form of the function. (b) Test results. Blue lines show results from five trials with the hybridized approach. Red lines show results from five trials with only a GA. An objective function value of 10^{-3}, indicated by the green line, is regarded as the target in this experiment.

with the learning process, which is also implemented in our acquisition design workflow. Figure 2.7a shows the results of a quick benchmark test of Algorithm 1 using a 2D form of the Schwefel function, consisting of many local minima, given by:

$$f(x_1, x_2, \ldots, x_n) = 418.9829n - \sum_{i=1}^{n} x_i \sin(\sqrt{|x_i|}), \tag{2.20}$$

with

$$x_i \in [-500, 500]\,, \tag{2.21}$$

where n indicates the dimension of the function. Here, the applied network classifies solutions to be evaluated. Genetic operators are responsible for generating solutions according to a real fitness evaluation. Although it is a quick trial, we can see the discernible difference owing solely to the integration of a GA and a neural network (Figure 2.7b). Some trials with only a GA, indicated by red lines, exceed more than 10^4 realizations to reach the pre-set requirement. On the other hand, all the five trials using the integrated approach, described by the blue lines, reach the target point with less than 10^3 realizations. Although it may be easier for a neural network to predict the mathematical function as compared to practical problems, it provides some insight into the effectiveness of the integrated approach.

This way of integration can be seen in several engineering domains. In various engineering problems, determining the objective function of a single candidate takes a long time to execute, e.g., due to the use of finite element analysis or computational fluid dynamics simulations. To deal with such computationally expensive optimization problems, a viable option is to use a model that can approximate the outcomes from the fitness evaluations at relatively low computation cost and to limit the number of real evaluations [31]. Kramer [32] illustrated a workflow to embed a supervised learning model into a GA where the real fitness evaluations are performed only to the solutions that fulfil some criterion in the predictive model. This way of integration is easily recognizable in different engineering applications [33–37]. Exploiting a strategy from these engineering

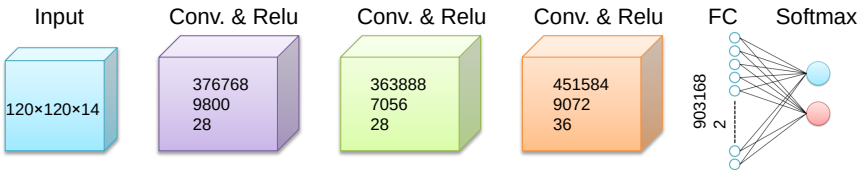

Figure 2.8: Diagram depicting the network architecture applied in [3]. Conv means a convolutional layer with two numbers indicating the channel size and the kernel size respectively. ReLU indicates a rectified linear unit layer. FC indicates a fully connected layer. The numbers in an input layer indicate the size of dimensions in the 3D matrix used as an input to the CNN. Vertically aligned three numbers in each convolutional layer indicate the numbers of neurons, weights and biases within a layer respectively. In a fully connected layer, two numbers indicate the numbers of weights and biases within a layer respectively.

problems is certainly valuable to our survey design problem because the large computational effort to calculate the objective function inherently restricts the number of fitness evaluations in our case. Hence, this study implements a CNN, which aims primarily to aid the population management in our GA and subsequently reach a satisfactory solution with affordable turn-around time. The implementation to the survey design problem can be found in the following chapters.

2.2.4. CLASSIFICATION OF SURVEY PARAMETERS

As described previously, the proposed workflow utilizes a CNN that accounts for the selection of survey designs prior to the evaluation step. Our implementation aims to classify whether survey parameters for a given design satisfy a pre-set criterion, i.e., the performance of a quality measure. Until this criterion is satisfied, genetic operators repeatedly produce new survey parameters which are subsequently evaluated by the CNN. Only solutions that pass the classification step in the CNN go to the step to compute an objective function.

Nakayama *et al.* [2], Nakayama and Blacquière [3], Nakayama *et al.* [12] utilizes a network architecture consisting of layers that are commonly used in CNN architectures: three pairs of 2D convolutional layers [38] and ReLU (rectified linear unit) layers [39], followed by a fully connected and softmax layer [40]. For instance, the network architecture applied in [3] is shown in Figure 2.8. Vertically aligned three numbers in each convolutional layer indicate the numbers of neurons, weights and biases in the layer. Each convolutional layer employs zero padding and a stride of one along the height and width dimensions with square shape kernels. Instead of down-sampling feature maps within the CNN via a pooling layer, we first arrange blending and sampling operators into a 3D matrix as an input to the CNN. The numbers in the input layer (Figure 2.8) indicate the size of dimensions in the 3D matrix used as an input to the CNN. Its width and height are equal to the numbers of columns and rows in $\mathbf{X}$, respectively. The third dimension is discussed in the following.

Figure 2.9 illustrates a way to arrange survey parameters, $\mathbf{D}$, $\mathbf{S}$, and $\mathbf{\Gamma}$, into the 3D matrix based on [3] which aimed at design of lateral locations of detectors and four DSA source types as well as encoded source signatures (Figure 2.10). Figure 2.9a exemplifies a layer containing information on a distribution of detectors and DSA source type 1. In

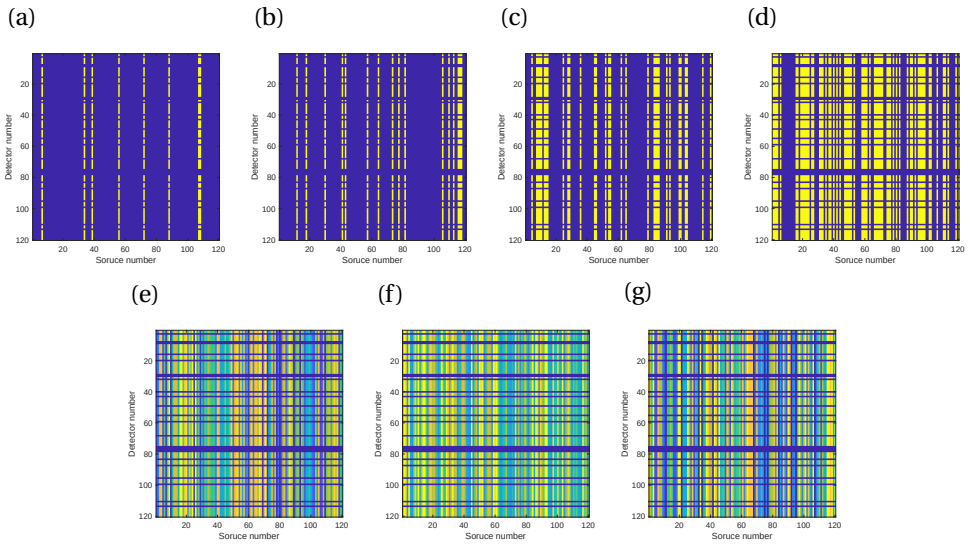

Figure 2.9: Feature maps containing information on applied survey parameters shown in Figure 2.10 (a)-(d) Distributions of zero elements in dark-blue and non-zero elements in yellow indicate spatial locations of detectors and four different DSA source types. (e)-(g) Variations among columns indicate spatially varying encoded source signatures in terms of activation time, sweep length and phase modulation, respectively.

this layer, all elements are either zero or one. A distribution of non-zero (indicated by yellow elements) and zero (indicated by dark-blue elements) rows represents the presence and absence of detectors in the corresponding locations. Similarly, a distribution of non-zero and zero columns represents the presence and absence of DSA source type 1 in the corresponding locations. Layers shown in Figures 2.9b-d indicate a distribution of detectors and DSA source type 2, 3 and 4, respectively. Figures 2.9e-g show a way to incorporate information on encoded source signatures into the network. The variation among columns in Figure 2.9e indicates activation times applied to different sources while missing rows corresponds to the absence of detectors. Likewise, Figures 2.9f and g show layers having information on spatial variation of sweep length and source modulation, respectively. These seven maps are transformed into the wavenumber domain via a 2D Fourier transform. Since these maps employ complex numbers, we form maps consisting of real and imaginary parts separately. As a consequence, fourteen maps are fed into the CNN as shown in Figure 2.8.

This arrangement leads to a significant reduction in the input data size. The design of network architecture including data arrangement is experimentally derived to fit our specific task. Although a deeper and more complex network would presumably enable us to directly input $\mathbf{D}$, $\mathbf{S}$ and $\mathbf{\Gamma}$ into the CNN in the future, for now, this helps to obtain acceptable classification results in an efficient manner, which can be found in the following chapters.

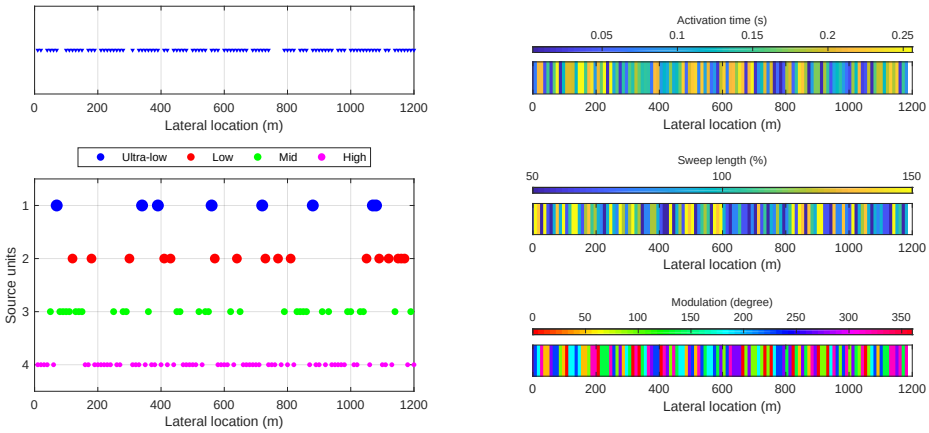

Figure 2.10: Acquisition scenario applied in [3]. The study aimed at optimizing distributions of detectors (the subplot with triangle markers on the upper-left)and four different DSA source units (the subplot with four different circle markers, each indicating spatial locations of ultra-low, low, mid and high frequency sources, on the lower-left) as well as different encoded source signatures such as activation time, sweep length and phase modulation (three subplots on the right). This information is arranged to seven maps shown in Figure 2.9.

Step 1	Main code: 01001011011100101010
Step 2	Base codes 1&2: 0100101101&1100101010
Step 3	Base codes 3&4: 1011010010&0101010011
Step 4	Primary source: 13424321231 4 -----
	Secondary source: 42131234324 1 -----

Figure 2.11: Steps to generate a binary string with RES. Twenty binary numbers exemplify a way to form long parameter vectors from the main code. Four different colours distinguish four base codes. Base codes 1 and 2 are simply the first and second half of the main code. Base codes 3 and 4 are the reverse of base codes 1 and 2.

2.2.5. REPEATED ENCODING SEQUENCE

Although GAs generally have the ability to handle large problem sizes, survey designing inherently provides a huge number of solutions. This is, even more, the case when dealing with parameters involved in irregularity, which is, unfortunately, the reality we deal with. Hence, a reduction of the solution space makes the proposed designing workflow practical and computationally affordable. In this respect, we propose repeated encoding sequence (RES), inspired by the nucleic acid sequence of deoxyribonucleic acid (DNA) [1]. DNA consists of a chain of four nucleobases: adenine (A); cytosine (C); guanine (G); and thymine (T). We make use of this as an analogy to form a parameter sequence in GAs to reduce problem space.

Figure 2.11 exemplifies our way to generate RES using twenty binary numbers. We first create a main code having a random-like feature (Step 1). Prior constraints can be embedded into this main code. It is then divided into two halves to make two base codes

(Step 2). These are flipped to create two more base codes (Step 3). The four base codes obtained in this way are finally combined in a predetermined order so that even long parameter sequences can be formed, like a chain of four nucleobases in DNA (Step 4). The order has to be predetermined to ensure reproducibility of the solution.

Additionally, it is well known that DNA has a double helix structure in which one nucleobase bonds only with one specific other. This is referred to as base pairs where A bonds only with T, while C bonds only with G. We also use this analogy for blended acquisition. We predefine base pairs. For example, as illustrated in step 4 in Figure 2.11, a base code 1 bonds with 4, while 2 bonds only with 3. When blending, we first define a parameter sequence of a primary source. Then parameters of a secondary source, which blends with the primary one, are automatically defined according to the concept of the base pairs. This ensures that sources, overlapping each other, likely hold different properties.

With RES, the optimization deals with a single main code rather than with a whole parameter sequence, which enables a significant reduction of the solution space. Although the four base codes are repeated, each one possesses a random-like feature and also appears in an irregular manner, based on a predetermined order. Therefore, the resulting survey parameters still employ the property of irregularity. Figure 2.12 shows the comparison of common shot and detector gathers in time-space and frequency-wavenumber domain having different spatial sampling and blending schemes. Figures 2.12a-d depict unblended and well-sampled data that contain no spatial aliasing or no blending noise. The other cases are pseudo-deblended data that employ 50% detector decimation and 50% source decimation, keeping one out of two detectors and one out of two sources. Additionally, two sources are blended. Figures 2.12e-h show regularly-decimated data, and two overlapped sources are activated at the same timing. This scenario shows coherent artefacts due to periodically missing traces, and blending noise appears still coherent. These properties result in difficulty to distinguish between desired events and undesired events, i.e., blending and aliasing noise. Irregular spatial sampling and activation times, derived from random variables, are applied to data shown in Figure 2.12i-l where blending and aliasing noise employ Gaussian-noise like features. Data with RES notably show a similar characteristic (Figure 2.12m-p). This consequently enables the subsequent process(es) to effectively handle the deficiency of recorded data as mentioned previously, while reducing the number of required parameters to define spatial sampling and blending schemes. Translation of binary strings to survey parameters, **D**, **S** and **Γ**, is described in section 2.2.2.

2.2.6. OPTIMIZATION OF AN ACQUISITION DESIGN PROBLEM

In various geophysical applications, the robustness and the capability of algorithms to reach a global optimum play an essential role as their fundamental objectives are to seek the ground truth such as subsurface properties. Therefore, solutions in local minima are often disregarded even when the objective function, representing the quality of the outcome, is reasonably minimized. The proposed acquisition design workflow does not necessarily guarantee the best output within a practical computation time. Furthermore, it may end up in some local minimum. Unlike the previously described geophysical problems, an acquisition design problem fortunately possesses the unique property

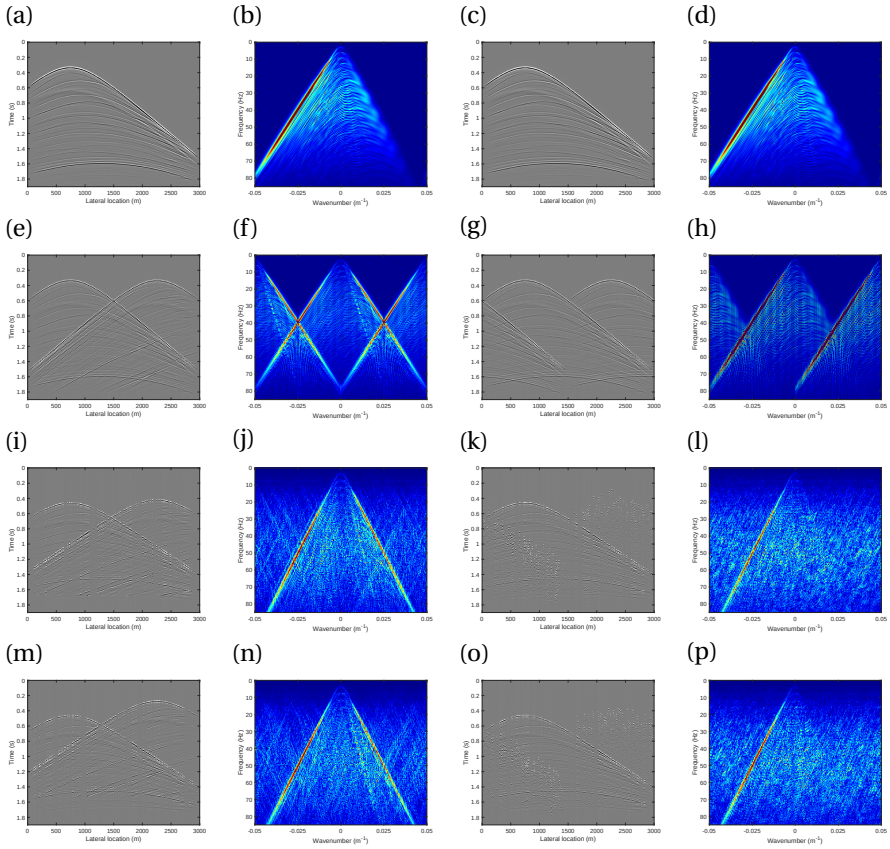

Figure 2.12: Shot and detector gathers in time-space and frequency-wavenumber domains with different blending and spatial sampling schemes. The first and second columns are shot records. The third and fourth columns are detector records. (a)-(d) Unblended and well-sampled data. (e)-(p) Pseudo-deblended data with 50% detector and source decimations with two overlapping sources. (e)-(h) Detectors and sources are regularly decimated, and no time dither is applied. (i)-(l) Detectors and sources are randomly decimated, and random time dither is applied. (m)-(p) RES is applied to derive detector and source decimation as well as time dither.

where the convergence to a global optimum does not have to be mandated. A solution in a local minimum is still acceptable as long as the pre-set criteria related to quality and economics are met. In our case, the ability to find acceptable solution(s) within an affordable turn-around time needs to be cultivated, which motivates us to implement the proposed integration of metaheuristics and machine learning along with the constraint in the solution space as described previously.

REFERENCES

[1] S. Nakayama, G. Blacquière, T. Ishiyama, and S. Ishikawa, *Blended-acquisition design of irregular geometries towards faster, cheaper, safer and better seismic surveying,* Geophysical Prospecting **67**, 1498 (2019).

[2] S. Nakayama, G. Blacquière, and T. Ishiyama, *Automated survey-design for blended-acquisition with irregular spatial sampling via the integration of a metaheuristic and deep learning,* Geophysics **84**, P47 (2019).

[3] S. Nakayama and G. Blacquière, *Automated Survey Design for Land Acquisition Using the Dispersed Source Array Concept,* New Advances in Land Geophysical Acquisition Technologies Workshop, Muscat, Oman (2019).

[4] G. Blacquière and S. Nakayama, *Optimum seismic acquisition geometry design with the help of artificial intelligence,* 89th SEG Annual Meeting, San Antonio, Texas, USA, Expanded Abstracts, 117 (2019).

[5] A. J. Berkhout, *Seismic migration, imaging of acoustic energy by wave field extrapolation, Part A: theoretical aspects* (Elsevier, 1982).

[6] A. J. Berkhout, *Review Paper: An outlook on the future of seismic imaging, Part I: Forward and reverse modelling,* Geophysical Prospecting **62**, 911 (2014).

[7] A. J. Berkhout, *Changing the mindset in seismic data acquisition,* The Leading Edge **27**, 924 (2008).

[8] S. Wu, G. Blacquière, and G.-J. A. van Groenestijn, *Shot repetition: An alternative seismic blending code in marine acquisition,* Geophysics **83**, P43 (2018).

[9] A. Mahdad, *Deblending of seismic data*, Ph.D. thesis, Delft University of Technology (2012).

[10] R. Abma and A. Ross, *Popcorn shooting: Sparse inversion and the distribution of airgun array energy over time,* 83rd SEG Annual Meeting, Houston, Texas, USA, Expanded Abstracts, 31 (2013).

[11] A. J. Berkhout, *Blended acquisition with dispersed source arrays,* Geophysics **77**, A19 (2012).

[12] S. Nakayama, G. Blacquière, and T. Ishiyama, *Acquisition design for direct reflectivity and velocity estimation from blended and irregularly-sampled data,* Geophysical Prospecting **67**, 2127 (2019).

[13] A. Cordsen, M. Galbraith, and J. Peirce, *Planning Land 3-D Seismic Surveys* (Society of Exploration Geophysicists, 2000).

[14] C. J. Regone, *Using 3D finite-difference modeling to design wide-azimuth surveys for improved subsalt imaging,* Geophysics **72**, SM231 (2007).

[15] G. J. O. Vermeer, *3D Seismic Survey Design, Second Edition* (Society of Exploration Geophysicists, 2012).

[16] S. Nakayama, G. Blacquière, T. Ishiyama, and S. Ishikawa, *Survey designing for blended acquisition with irregularly sub-sampled geometries,* 80th EAGE Conference and Exhibition, Copenhagen, Denmark, Extended Abstracts **Th A 14** (2018).

[17] C. R. Darwin, *On the Origin of Species by Means of Natural Selection, or the Preservation of Favoured Races in the Struggle for Life* (John Murray, London, 1859).

[18] J. H. Holland, *Adaptation in Natural and Artificial Systems* (University of Michigan Press, 1975).

[19] A. Monteagudo and J. Santos, *Evolutionary optimization of cancer treatments in a cancer stem cell context,* Genetic and Evolutionary Computation Conference 2015, 233 (2015).

[20] E. Davies, P. Tew, D. R. Glowacki, J. Smith, and T. Mitchell, *Evolving atomic aesthetics and dynamics,* Proceedings of the 5th International Conference on Evolutionary and Biologically Inspired Music, Sound, Art and Design, EvoMUSART 2016, Porto, Portugal, 17 (2016).

[21] S. H. Bak, N. Rask, and S. Risi, *Towards adaptive evolutionary architecture,* Proceedings of the 5th International Conference on Evolutionary and Biologically Inspired Music, Sound, Art and Design, EvoMUSART 2016, Porto, Portugal, 47 (2016).

[22] M. Scirea, J. Togelius, P. Eklund, and S. Risi, *Metacompose: A compositional evolutionary music composer,* Proceedings of the 5th International Conference on Evolutionary and Biologically Inspired Music, Sound, Art and Design, EvoMUSART 2016, Porto, Portugal, 202 (2016).

[23] D. Perez-Liebana, J. Dieskau, M. Hunermund, S. Mostaghim, and S. M. Lucas, *Open loop search for general video game playing,* Genetic and Evolutionary Computation Conference, Madrid, Spain, 337 (2015).

[24] O. Kramer, *Machine Learning for Evolution Strategies* (Springer, 2016).

[25] K. P. Murphy, *Machine Learning: A Probabilistic Perspective* (The MIT Press, 2012).

[26] G. Hinton, L. Deng, D. Yu, G. Dahl, A. rahman Mohamed, N. Jaitly, A. Senior, V. Vanhoucke, P. Nguyen, T. Sainath, and B. Kingsbury, *Deep neural networks for acoustic modeling in speech recognition: The shared views of four research groups,* IEEE Signal Processing Magazine **29**, 82 (2012).

[27] M. K. K. Leung, H. Y. Xiong, L. J. Lee, and B. J. Frey, *Deep learning of the tissue-regulated splicing code,* Bioinformatics **30**, i121 (2014).

[28] J. Schmidhuber, *Deep learning in neural networks: An overview,* Neural networks **61**, 85 (2015).

[29] F. Ahmadizar, K. Soltanian, F. AkhlaghianTab, and I. Tsoulos, *Artificial neural network development by means of a novel combination of grammatical evolution and genetic algorithm,* Engineering Applications of Artificial Intelligence **39**, 1 (2015).

[30] L. Xie and A. Yuille, *Genetic CNN,* IEEE International Conference on Computer Vision, 1379 (2017).

[31] Y. Tenne and C.-K. Goh, *Computational intelligence in expensive optimization problems* (Springer, 2010).

[32] O. Kramer, *Genetic algorithm essentials* (Springer, 2017).

[33] J.-L. Marcelin, *A metamodel using neural networks and genetic algorithms for an integrated optimal design of mechanisms,* The International Journal of Advanced Manufacturing Technology **24**, 708 (2004).

[34] J. Sreekanth and B. Datta, *Comparative evaluation of genetic programming and neural network as potential surrogate models for coastal aquifer management,* Water resources management **25**, 3201 (2011).

[35] S. Ibaraki, I. Tomita, and K. Sugimoto, *Aerodynamic design optimization of centrifugal compressor impeller based on genetic algorithm and artificial neural network,* Mitsubishi Heavy Industries Technical Review **52**, 77 (2015).

[36] T. Sato and M. Fujita, *An investigation of design optimization of electric devices supported by machine learning,* IEICE technical report **116**, 289 (2016).

[37] D. Sakaguchi, M. Tun, R. Numakura, and B. Wang, *Global optimization of recirculation flow type casing treatment in centrifugal compressors of turbochargers,* Proceedings of the Institution of Mechanical Engineers, Part C: Journal of Mechanical Engineering Science **232**, 4461 (2018).

[38] Y. LeCun, L. Bottou, Y. Bengio, and P. Haffner, *Gradient-Based Learning Applied to Document Recognition,* Proceedings of the IEEE **86**, 2278 (1998).

[39] R. H. Hahnloser, R. Sarpeshkar, M. A. Mahowald, R. J. Douglas, and H. S. Seung, *Digital selection and analogue amplification coexist in a cortex-inspired silicon circuit,* Nature **405**, 947 (2000).

[40] C. Bishop, *Pattern Recognition and Machine Learning* (Springer, 2006).

3

OPTIMUM DEBLENDING AND DATA RECONSTRUCTION

Blended acquisition along with efficient detector and source geometries allows for cost-effective operation. The outcome of subsequent deblending and data reconstruction is of primary importance in determining the technical success of this manner of data acquisition. Despite its advantages over conventional seismic surveys, finding optimum survey parameters is a difficult task. Although incorporating irregularity into spatial sampling and blending schemes leads to effective deblending and data reconstruction, it inherently provides a significantly large problem space. We introduce a survey design workflow to provide acquisition parameters that account for the source blending as well as the spatial sampling of detectors and sources in an automated manner. The proposed method involves an iterative scheme to derive the survey parameters that lead to an optimum deblending and data reconstruction quality. The approach deals jointly with deblending and data reconstruction via a sparse inversion in the frequency-wavenumber domain coupled with constraints based on causality and coherency. The residue from this process is subsequently used to update the survey parameters by integrating a genetic algorithm and a convolutional neural network. Bio-inspired operators enable the simultaneous updates of the blending and sampling operators. To relate the choice of survey parameters to the performance of deblending and data reconstruction, we utilize a convolutional neural network. The applied network architecture successfully rejects suboptimal solutions among newly generated ones from genetic operators. Consequently, only optimal ones are fed into the subsequent evaluation step, making the proposed approach computationally affordable. We apply our workflow to design a seismic survey that incorporates the dispersed source array concept. A comparison among different survey design strategies highlights the ability of the method to effectively derive optimum solutions. The resultant acquisition scenario derived from the proposed approach yields a notable enhancement of deblending and data reconstruction quality attributed solely to the choice of survey parameters. Additionally, to explicitly handle conflicting objectves in a seismic survey, i.e.,

Parts of this chapter are available in references [1–4].

quality and cost, we implement a non-dominated sorting genetic algorithm. A numerical example shows that this implementation derives optimum solutions along the Pareto optimal front of these two objectives, which subsequently allows us to identify the one that fits the purpose of the survey.

3.1. INTRODUCTION

In this chapter, we describe results from the proposed iterative scheme to design survey parameters related to both the blending and spatial sampling operators. The workflow incorporates a closed-loop approach that jointly estimates deblended and reconstructed data from blended and irregularly-sampled data. The residue for a given survey design is assigned as its objective function and is subsequently input into a survey-parameter update system based on the integration of a genetic algorithm (GA) and a convolutional neural network (CNN). Genetic operators that mimic the process of natural selection allow for simultaneous updates of the blending and sampling operators towards optimum solutions. A CNN is implemented for population management to select optimum candidates and reject undesired ones among newly generated solutions from genetic operators. Only designs classified as "high potential" by the applied CNN are fed into the evaluation of the objective function that involves deblending and reconstruction. Since the latter is computationally expensive, the classification effectively prevents wasteful computation of suboptimal solutions, which consequently enhances the performance of the overall optimization scheme. Numerical examples that incorporate the dispersed source array (DSA) concept [5, 6] outline the results of our approach. The proposed approach attempts to derive an acquisition geometry, leading to optimum deblending and reconstruction under given practical constraints such as the numbers of detectors, sources and blending fold. Additionally, we investigate application of the multi-objective optimization, aimed at obtaining solutions along the Pareto optimal front of conflicting objectives such as quality and business aspects.

3.2. SURVEY DESIGN WORKFLOW

As mentioned previously, Equation 2.7 indicates that, starting with $\mathbf{X}$, our forward model can be applied to simulate different blending and spatial sampling schemes by designing $\mathbf{D}$, $\mathbf{S}$ and $\mathbf{\Gamma}$.

Figure 3.1 illustrates the proposed iterative survey-design method for optimum deblending and data reconstruction quality. The procedure starts with $\mathbf{X}$. In this study, we assume $\mathbf{X}$ to be known as we deal with acquisition design. This is the case when the subsurface information is available, e.g., at a development or production stage, or when data from a previous acquisition are available. In practice, $\mathbf{X}$ is modelled data based on all available prior information of the subsurface. This makes the solution from our workflow subsurface dependent. The forward process in the blue box derives $\mathbf{P}'$ (application of $\mathbf{D}$, $\mathbf{S}$ and $\mathbf{\Gamma}$ to $\mathbf{X}$). The inverse process in the red box then estimates $\langle\mathbf{X}\rangle$ from $\mathbf{P}'$. The angled brackets $\langle$ and $\rangle$ indicate estimations.

The separation of blended data and the reconstruction of missing data can share a certain resemblance. Both cases are often treated as an inverse problem that involves iterative estimation of desired events and subtraction of undesired events, i.e.., blending and aliasing noise, in the model space domain. Li *et al.* [7], Cheng and Sacchi [8], Cao *et al.* [9] jointly dealt with deblending and reconstruction. Mahdad *et al.* [10] utilized an iterative deblending scheme using sparseness and coherency constraints. Ishiyama *et al.* [11] established a generalized blending model and reconstruction of deblended data based on this model. Following these studies, we formulate an inverse scheme

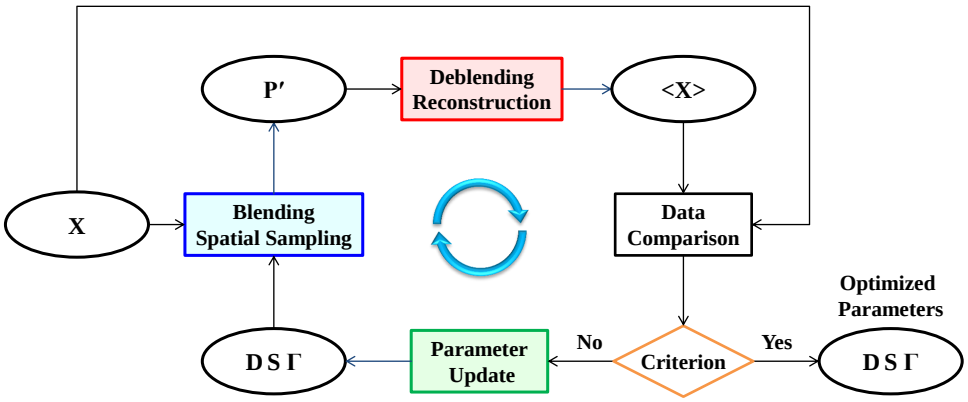

Figure 3.1: The survey design workflow. The iterative scheme aims to output the blending and sampling operators that can provide an improved deblending and reconstruction quality. The workflow starts with $\mathbf{X}$. The forward process in the blue box derives $\mathbf{P}'$ (application of $\mathbf{D}$, $\mathbf{S}$ and $\mathbf{\Gamma}$ to $\mathbf{X}$). The inverse process in the red box then estimates $\langle\mathbf{X}\rangle$ from $\mathbf{P}'$. The procedure stops if the misfit between $\mathbf{X}$ and $\langle\mathbf{X}\rangle$ is sufficiently small or the maximum number of iterations is reached. If not, $\mathbf{D}$, $\mathbf{S}$ and $\mathbf{\Gamma}$ are updated in the green box. Newly generated operators are carried into the next iteration.

based on the L1 norm optimization as:

$$\min \|\mathbf{L}\langle\mathbf{X}\rangle\|_1 \text{ s.t. } \mathbf{D}\langle\mathbf{X}\rangle\mathbf{S}' = \mathbf{P}', \tag{3.1}$$

where $\mathbf{L}$ is the transform operator. This inversion scheme promotes the sparsity of the solution in the transform domain (e.g., the frequency-wavenumber domain in our case), while minimizing the misfit between $\mathbf{D}\langle\mathbf{X}\rangle\mathbf{S}'$ and $\mathbf{P}'$, along with the constraints based on causality and coherency of the data. The detailed description of the deblending and data reconstruction procedure is available in Appendix A. It should be noted that any deblending and data reconstruction scheme can be flexibly accommodated in the proposed workflow, i.e., the red box in Figure 3.1.

The proposed workflow aims at finding optimum $\mathbf{D}$, $\mathbf{S}$ and $\mathbf{\Gamma}$that can minimize the objective function:

$$J = \sum_{\omega} \|\mathbf{X} - \langle\mathbf{X}\rangle\|_2^2. \tag{3.2}$$

If the residue between $\mathbf{X}$ and $\langle\mathbf{X}\rangle$ is sufficiently small, or if the maximum number of iterations is reached, the iterative procedure stops. If the criterion is not met, the blending and sampling operators, i.e., the survey design parameters, are updated in the green box of Figure 3.1 (see Algorithm 1 in Chapter 2 for more details on the way to update survey parameters). The workflow subsequently feeds newly generated parameters into the next iteration. Hence, the resultant survey design derived from our iterative scheme provides optimum deblending and reconstruction quality.

3.3. MARINE DSA EXAMPLE

A subset of synthesized 2D Marmousi data is used to numerically simulate several acquisition scenarios incorporating the DSA concept that utilizes a set of source units, each having a dedicated narrow frequency range [5]. Caporal *et al.* [6] discussed its benefits from different perspectives, some of which are reviewed as follows. The technique permits each narrow-band source to be independently deployed to satisfy its own spatial sampling criteria determined by its frequency range. This subsequently allows for proper sampling of entire frequency ranges and addresses both the oversampling of lower frequencies and the undersampling of higher frequencies. In a marine survey, the method minimizes destructive interference from a source ghost in the spectrum using so-called ghost matching. By towing narrowband sources at different and proper depth levels, source notches insignificantly overlap with the frequencies emitted from these sources.

Figure 3.2 shows a common shot gather and a common detector gather from a subset of 2D Marmousi data, which we consider as the reference data, $\mathbf{X}$ (transformed to the time domain). All the detectors and sources are regularly placed with a 10 m sampling interval. Each source generates a spatially uniform and broadband signature.

Different acquisition scenarios that employ the DSA concept are numerically simulated using $\mathbf{X}$. In this study, four types of source units are deployed, each unit being char-

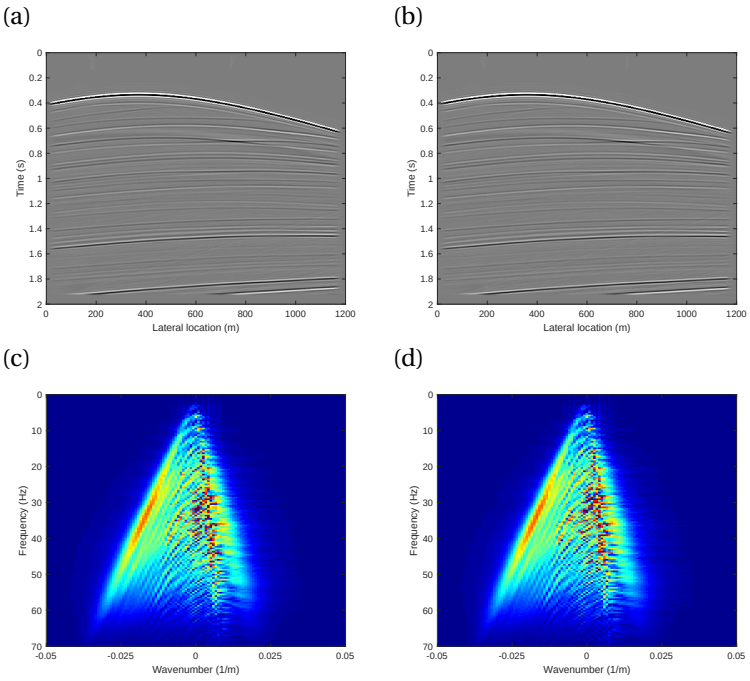

Figure 3.2: Unblended and well-sampled data (reference data). Common shot gather (the left column) and common detector gather (the right column): (a)-(b) in the time-space domain; and (c)-(d) in the frequency-wavenumber domain.

acterized by its own spatial sampling scheme and dedicated narrow frequency range as defined in Table 3.1. Together, the source units cover the complete frequency band of interest, including the very low frequencies.

Table 3.2 summarizes detector and source sampling schemes applied to $\mathbf{P}'$ as compared to the reference data $\mathbf{X}$. In addition to the spatial irregularity embedded into each DSA source, detectors are irregularly decimated by 20%. Figure 3.3a shows a 3D view of the reference data in which no deficiency in spatial sampling is recognizable. Two sections along the detector-x axis and the source-x axis correspond, respectively, to a common shot gather and a common detector gather. Figures 3.3b-e show unblended and irregularly-sampled data, being the response of four source units. As described in Tables 3.1 and 3.2, each source unit employs its own properties in space and frequency. Here, sources and detectors are randomly distributed. In this study, the blending scenario involves two active sources with 600 m spatial separation per blended experiment. Additionally, a time delay between 0 s and 0.256 s is applied to each source.

Source types	Number of sources	Frequency response (Hz)
Unit 1	8	2-4-6-10
Unit 2	16	4-8-12-20
Unit 3	32	8-16-24-40
Unit 4	64	16-32-48-80

Table 3.1: Properties of four DSA sources. Each source unit employs different spatial sampling requirements according to its frequency response specified by four corner frequencies (the low-cut, low-pass, high-pass and high-cut).

	$\mathbf{X}$	$\mathbf{P}'$
Detector interval	10 m at regular	irregular
Number of detectors	120	96 (20% decimation)
Source interval	10 m at regular	irregular
Number of sources	120	(see Table 3.1)
Number of activated sources	1	2 with 600 m separation

Table 3.2: Acquisition configurations applied to unblended and well-sampled data ($\mathbf{X}$) and blended and irregularly-sampled data ($\mathbf{P}'$). Spatial sampling of source for $\mathbf{P}'$ differs with the DSA source units (Table 3.1).

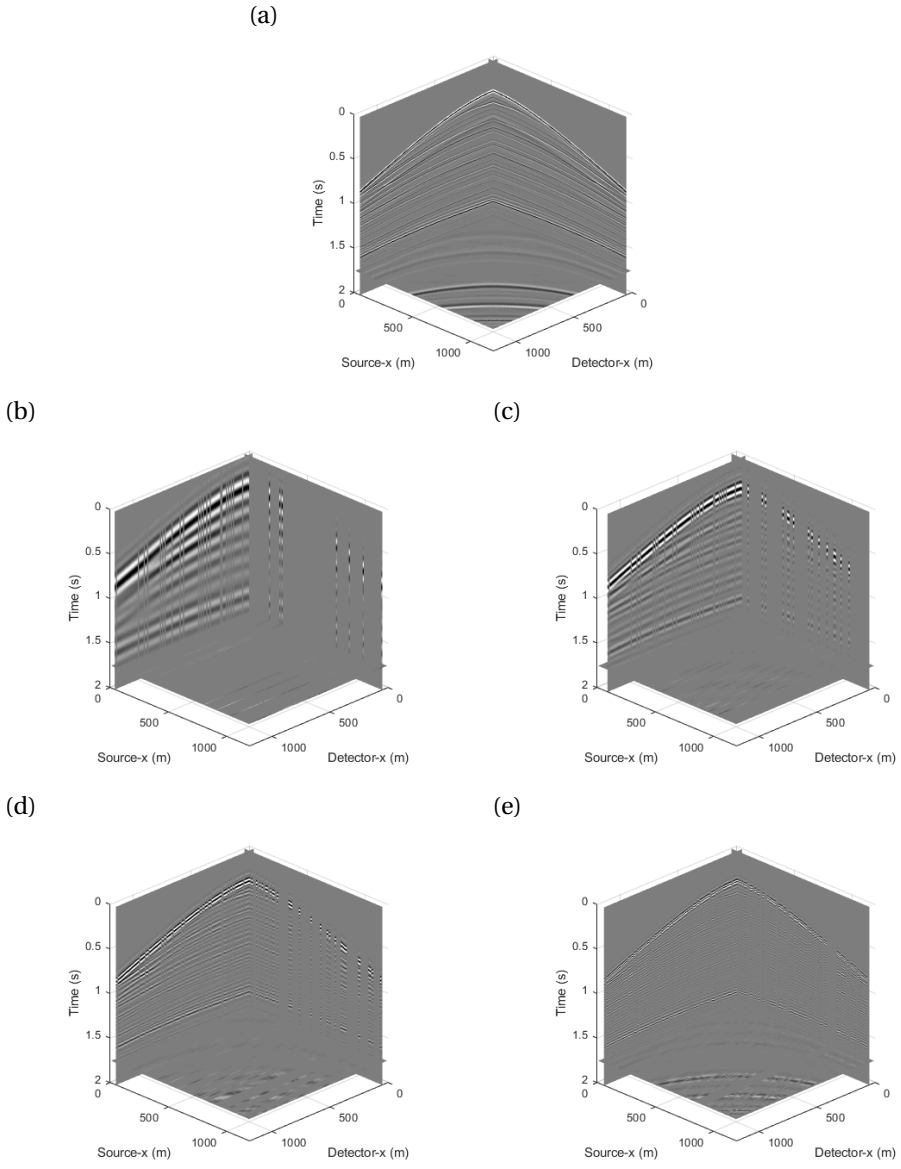

Figure 3.3: 3D view of data volume. (a) Well-sampled and broadband data. (b)-(e) Irregularly-sampled and narrow-band data from source unit 1, unit 2, unit 3 and unit 4, respectively. Seismic sections along the detector-x axis and the source-x axis correspond, respectively, to a common shot gather and a common detector gather. In (b)-(e), detectors are irregularly decimated by 20%. Property of each source unit is defined in Table 3.1.

The proposed approach aims to design survey parameters that, on the one hand, describe a cost-effective, blended, irregular, DSA acquisition geometry, while, at the other hand, enable the optimum retrieval of deblended and reconstructed data with large bandwidth. In addition to our optimized design, we also show some other results for comparison purposes. These designs employ blending and sampling operators generated by 800 realizations of uniformly-distributed random variables. We provide the median result, "P50", which we assume to be representative of the situation where a single random realization is used to incorporate irregularity into survey parameters. In addition, we provide the best result, "P1", which represents the outcome of a Monte Carlo approach.

Figures 3.4-3.6 show deblending and data reconstruction results from P50, P1 and our optimized design, respectively. Each realization consists of 100 iterations for deblending and data reconstruction. Although all three scenarios employ the same number of sources and detectors as well as the same blending fold [12], they show discernible differences, attributed solely to the choice of survey parameters. Some improvement is recognizable in P1 as compared to P50. Nonetheless, deblended and reconstructed data from both cases still show jitter in several reflections and some crossing events in the time-space domain. In the frequency-wavenumber domain, some energy spreads out the signal cone which is invisible in the reference data (Figure 3.2). Such effects are obviously indicative of errors in deblending and reconstruction. The optimized design, however, attains notable improvement in deblending and reconstruction such as an enhanced coherency of the seismic events along with a reduced cross talk. In particular, a comparison of difference plots among the three cases is self-evident (see the third columns in Figures 3.4-3.6). The results indicate that the proper design of survey parameters plays an important role in the performance of deblending and data reconstruction.

In addition to the observations made from seismic sections, Figure 3.7 quantitatively highlights the overall data quality of each scenario. This also confirms the superiority of the optimized design. The blue line shows the value of the objective function at each realization of our design approach, clearly demonstrating that it successfully minimizes the objective function through the course of the iterations. The red line shows the results from random realizations. The 653^{rd} realization is P1 that has the smallest objective function value among the 800 solutions. The dashed line indicates a median objective function value at each realization. After a couple of hundreds of realizations, no significant fluctuation is observable in the median value. This implies that P50 can reasonably represent the anticipated data quality in the case where we use a single random realization to design blending and sampling operators.

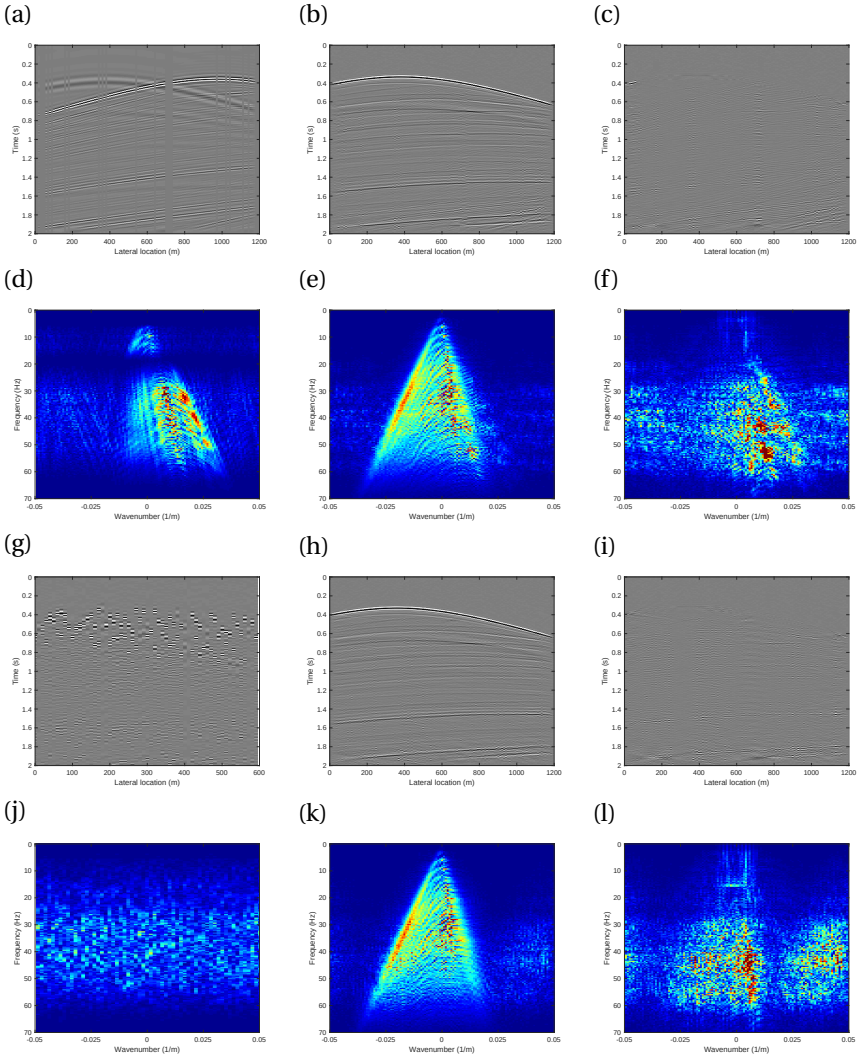

Figure 3.4: Blended and irregularly-sampled data (P50: the median result from 800 random realizations) in the time-space domain and the frequency-wavenumber domain. (a)-(f) Data in the common source domain. (g)-(l) Data in the common detector domain. The left and middle columns show data before and after deblending and data reconstruction, respectively. The right column shows differences between the reference and estimated data. Difference plots in the frequency-wavenumber domain (f and l) are amplified by a factor of three.

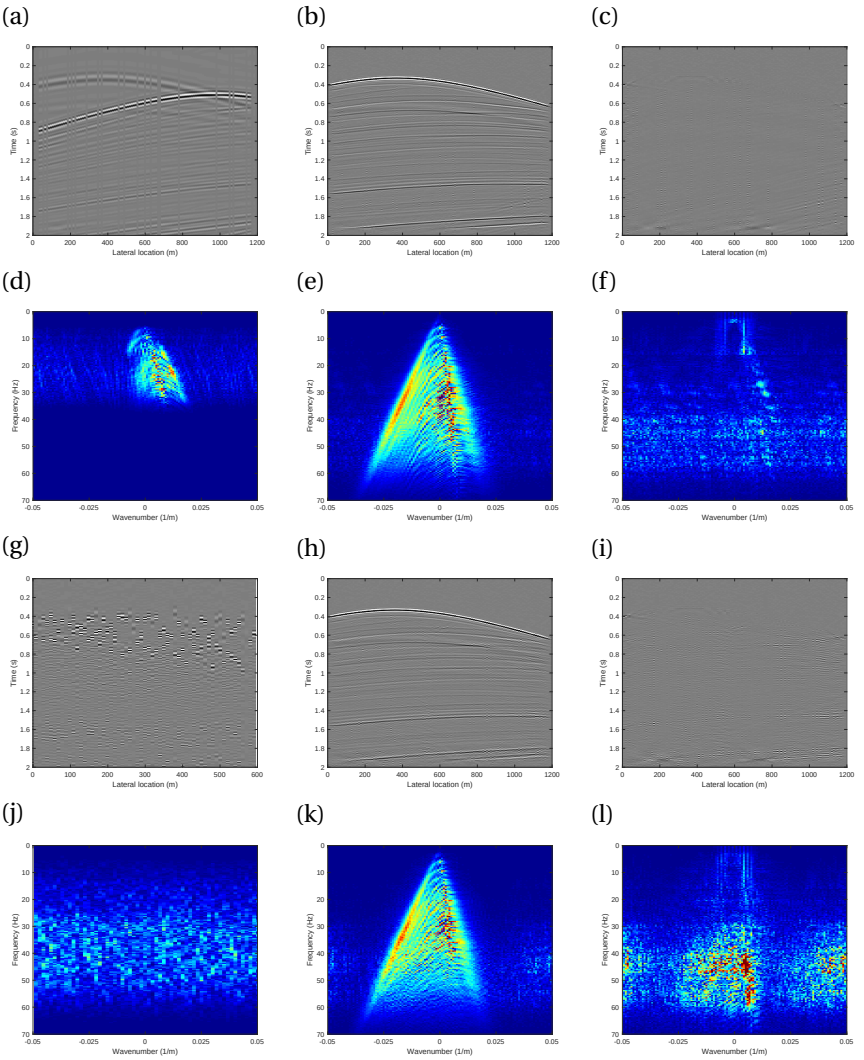

Figure 3.5: Blended and irregularly-sampled data (P1: the best result from 800 random realizations) in the time-space domain and the frequency-wavenumber domain. (a)-(f) Data in the common source domain. (g)-(l) Data in the common detector domain. The left and middle columns show data before and after deblending and data reconstruction, respectively. The right column shows differences between the reference and estimated data. Difference plots in the frequency-wavenumber domain (f and l) are amplified by a factor of three.

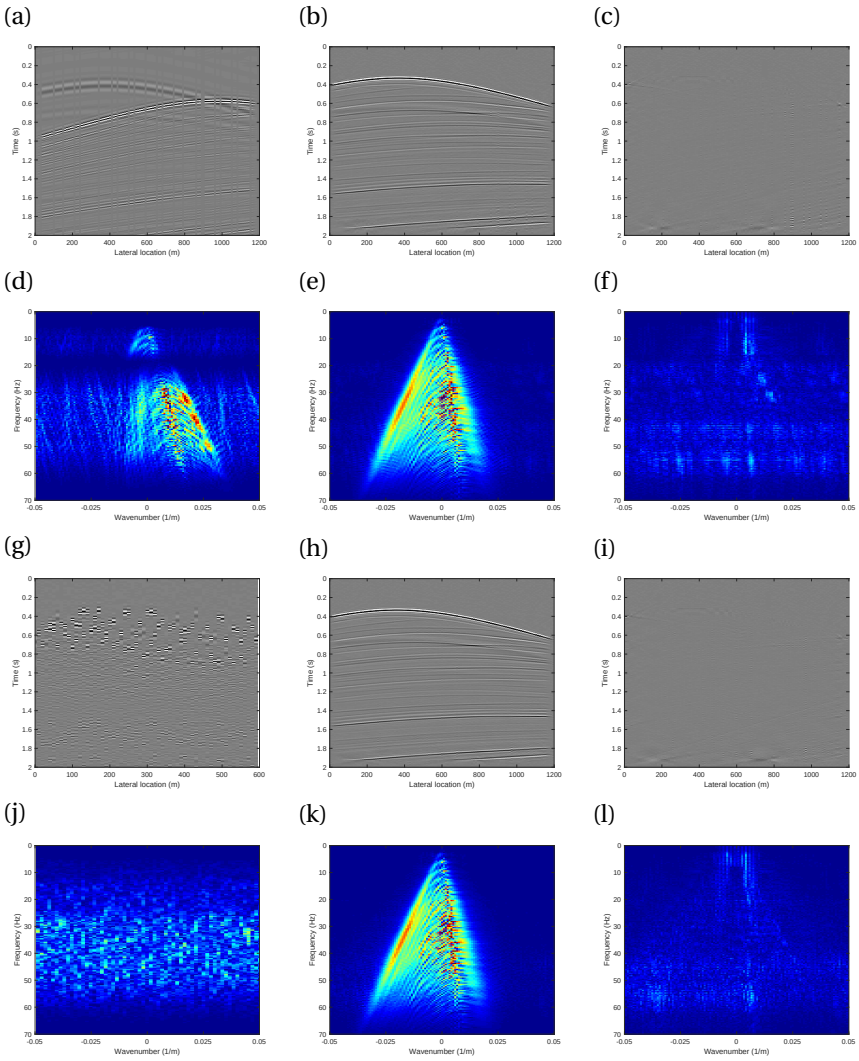

Figure 3.6: Blended and irregularly-sampled data (the proposed method) in the time-space domain and the frequency-wavenumber domain. (a)-(f) Data in the common source domain. (g)-(l) Data in the common detector domain. The left and middle columns show data before and after deblending and data reconstruction, respectively. The right column shows differences between the reference and estimated data. Difference plots in the frequency-wavenumber domain (f and l) are amplified by a factor of three.

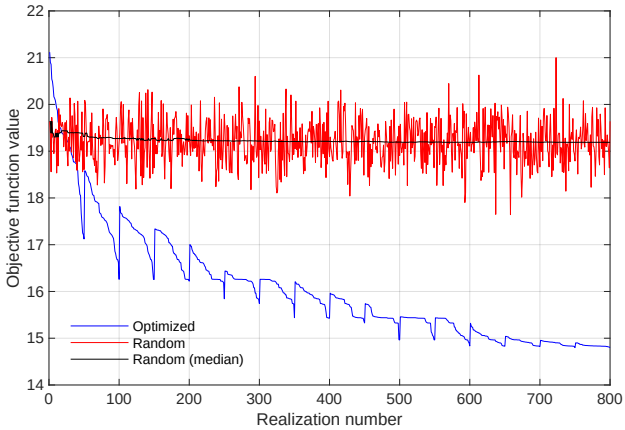

Figure 3.7: Objective function value at each realization. The blue and red lines represent objective function values from the proposed approach and random realization, respectively. The black dashed line indicates data having a median objective function value from random realizations.

The histogram in Figure 3.8 illustrates the distribution of objective function values from the 800 random realizations. The blue line is the probability density function (PDF) obtained from the normal distribution with the mean value of 19.2 and the standard deviation value of 0.47, respectively. It fits the actual data distribution reasonably well. If we assume that it correctly describes the PDF of the outcomes of Monte Carlo optimization schemes, we find that the cumulative probability of the objective function value of our optimized design becomes smaller than 10^{-20}. Although this observation may not be applicable to other problems, statistically, this suggests that a considerable number of random realizations are needed to obtain a result that is equivalent to our optimized design. This presents an obvious impracticality. On the other hand, our workflow is capable of deriving it with 800 realizations. As described previously, the computational burden of the GA and the CNN is insignificant. An extra effort, required to design the optimization framework such as the selection of parameters within the GA and the CNN, should be acceptable, provided that the previously mentioned cumulative probability density value reasonably describes the performance of our approach. The use of a single random realization is definitely the quickest and the simplest way. Nevertheless, it potentially provides a technically undesired outcome as indicated by P50. Hence, the result demonstrates the ability of the proposed approach to effectively optimize blending and sampling operators in a computationally affordable manner.

As described in section 2.2.2, our scheme involves an N-fold cross-validation to assess classification accuracies, while training the CNN. In this example, we perform a five-fold cross-validation at every 50 realizations (Figure 3.9). A vertical error bar de-

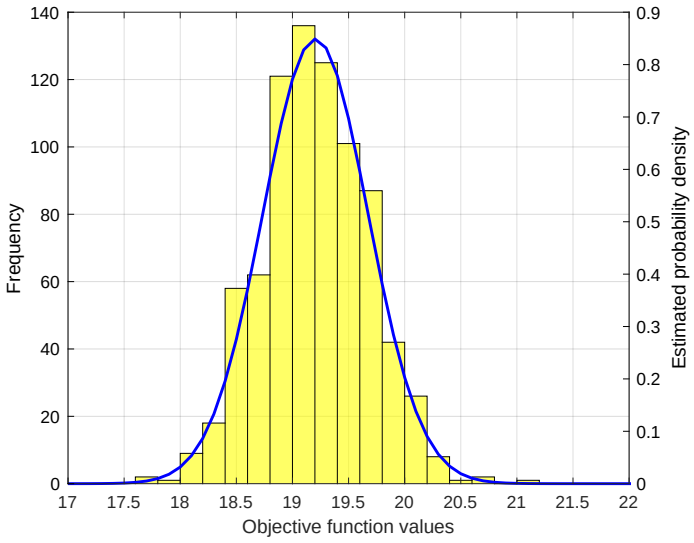

Figure 3.8: Frequency distribution of objective function values from 800 random realizations overlaid with estimated probability density function. The vertical axis on the left side indicates the frequency counts of yellow bins in the histogram. The blue line plotted against the vertical axis on the right side represents the probability density function derived from the normal distribution.

picts the minimum and the maximum accuracies obtained from each validation. Blue and red circle markers represent the mean value from five cross-validations for training and testing, respectively. Due to the limited number of samples at the early stage of the iterations, some discrepancy in accuracies between training datasets and testing datasets is still recognizable, which is presumably indicative of high variance in the predictive model. Since we alter a threshold value and some parameters within the CNN, the validation results among different stages are not fairly comparable. Nevertheless, the classification performance evidently improves through the course of the iterations. Additionally, the difference in accuracies between training sets and testing sets becomes insignificant after a couple of hundreds of realizations where the classification achieves roughly 90% average accuracy for both training and testing sets, with a small discrepancy between the minimum and the maximum values. This indicates that our network architecture along with selected hyperparameters manages the bias-variance trade-off reasonably well and successfully relates the choice of survey parameters to resultant deblending and data reconstruction quality.

3.4. LAND DSA EXAMPLE

The same synthesized dataset obtained from the 2D Marmousi model (Figure 3.2) is used to demonstrate a situation representing DSA acquisition in a land environment. The same DSA scenario (Table 3.1) and spatial sampling schemes (Table 3.2) are also applied.

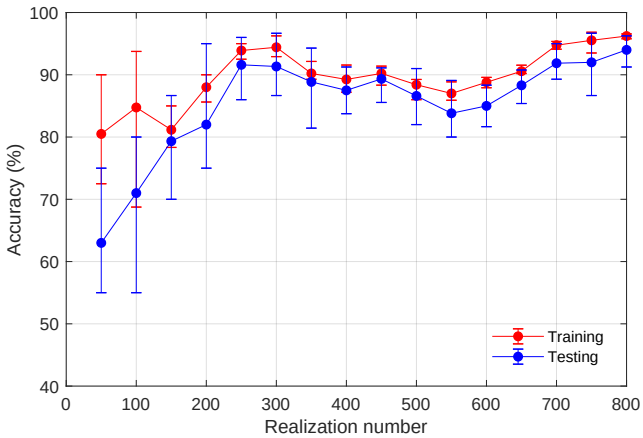

Figure 3.9: Classification accuracy of the predictive model at every 50 realizations. The red and blue markers represent mean accuracies at each five-fold cross-validation from training and testing sets, respectively. Error bars indicate the minimum and maximum accuracies obtained from each validation.

In addition to band limitation to accommodate the DSA concept, we encode a vibroseis sweep signature to make our example represent a land seismic survey as shown in Figure 3.10a. We also enhance the uniqueness of each encoded signature by the use of spatially variant time dither (Figure 3.10b), sweep length (Figure 3.10c) and phase modulation (Figure 3.10d). In this example, the blending scenario involves two active sources with 600 m spatial separation per blended experiment. We update the spatial distributions of detectors and four types of DSA source units (ultralow-, low-, mid- and high-frequency units) as well as encoded signatures applied to each shot such as time dither, sweep length and phase modulation.

In addition to our optimized design, we show some other results for comparison purposes. Like the previous section, these designs employ blending and sampling operators generated by 800 realizations of uniformly-distributed random variables. We provide the median result, "P50", which we assume to be representative of the situation where a single random realization is used to incorporate irregularity into parameters. We also show the best result, "P1", which represents the outcome of a Monte Carlo approach. These three scenarios employ the same number of sources and detectors as well as the same blending fold [12], while they employ different designs in terms of distributions of detectors and DSA sources as well as encoded source signatures.

Figures 3.11-3.13 show deblending and data reconstruction results from P50, P1 and our optimized design, respectively. Although data with encoded sweep signatures employ a larger record length, they are clipped for a display purpose. Similar to the observation made in the previous section, the optimized design clearly leads to a notable

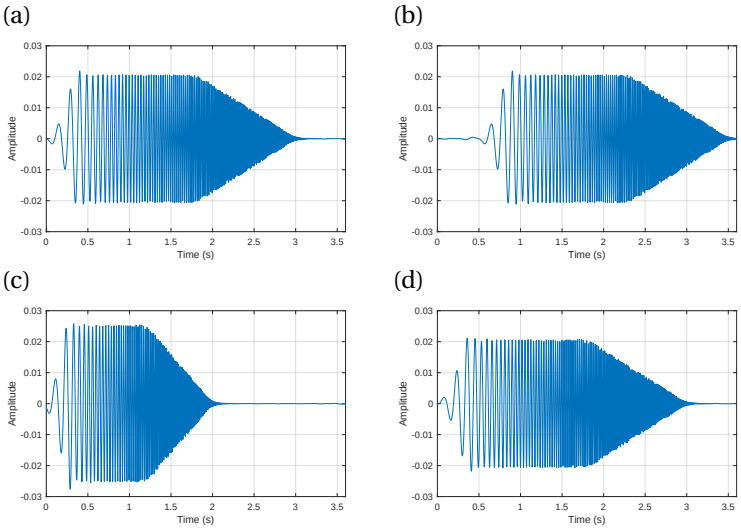

Figure 3.10: Encoded source signatures applied in a land example. (a) Base sweep signature. (b) Time shift. (c) Sweep length. (d) Phase rotation.

improvement in deblending and reconstruction quality. The difference plots evidently reflect these differences, where smaller recovery errors are easily recognizable in the optimized design (the right column in Figures 3.11-3.13).

Figure 3.14 quantitatively describes the overall data quality of each scenario. The red line shows the results from random realizations. The 28^{th} realization is considered as P1 having the smallest objective function value among the 800 solutions. The black line indicates a median objective function value at each realization. A design having the median value after 800 realizations is selected as P50. Similar to the previous marine DSA example, this land DSA example also demonstrates that the proposed approach effectively minimizes the objective function through the course of the iterations as indicated by the blue line.

Along with the previous section, this result confirms the viability of our approach for deriving the blending and sampling operators, leading to the improvement of deblending and data reconstruction for different blending and spatial sampling schemes. This also implies the wide applicability of the proposed method for acquisition in various situations. Our forward modelling can accommodate various types of encoded signatures. This accordingly enables us to simulate several scenarios that correspond to acquisition in different environments. The inverse model then makes robust deblending and reconstruction of these data achievable as described in Appendix A. The proposed scheme allows for the simultaneous updates of blending and sampling operators and subsequently derives an optimum design for scenarios having various blending codes coupled with spatial sampling criteria.

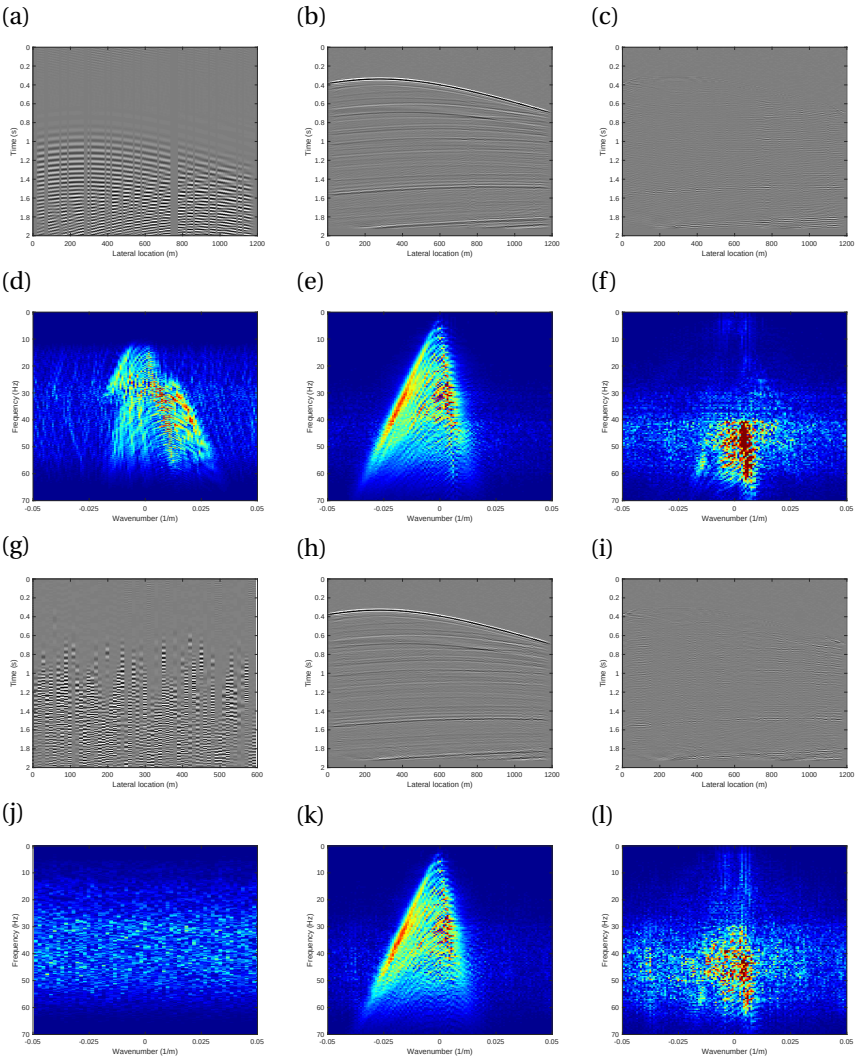

Figure 3.11: Blended and irregularly-sampled data (P50: the median result from 800 random realizations) in the time-space domain and the frequency-wavenumber domain. (a)-(f) Data in the common source domain. (g)-(l) Data in the common detector domain. The left and middle columns show data before and after deblending and data reconstruction, respectively. The right column shows differences between the reference and estimated data. Difference plots in the frequency-wavenumber domain (f and l) are amplified by a factor of three.

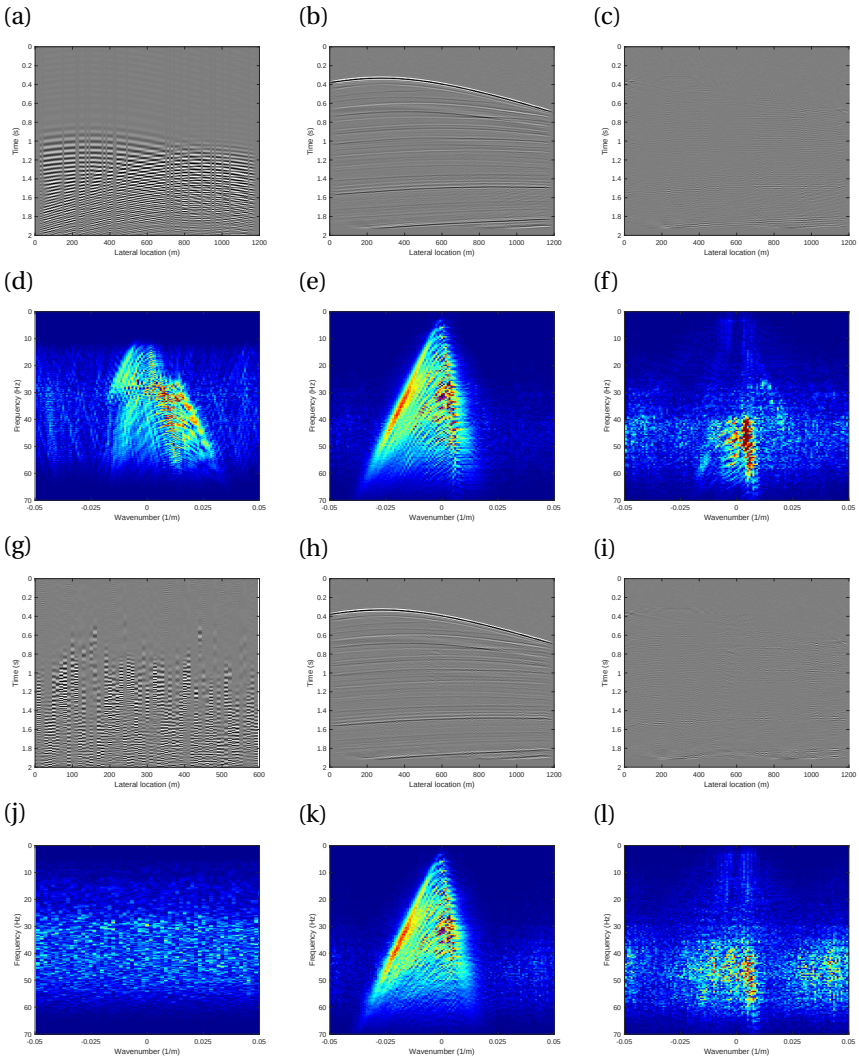

Figure 3.12: Blended and irregularly-sampled data (P1: the best result from 800 random realizations) in the time-space domain and the frequency-wavenumber domain. (a)-(f) Data in the common source domain. (g)-(l) Data in the common detector domain. The left and middle columns show data before and after deblending and data reconstruction, respectively. The right column shows differences between the reference and estimated data. Difference plots in the frequency-wavenumber domain (f and l) are amplified by a factor of three.

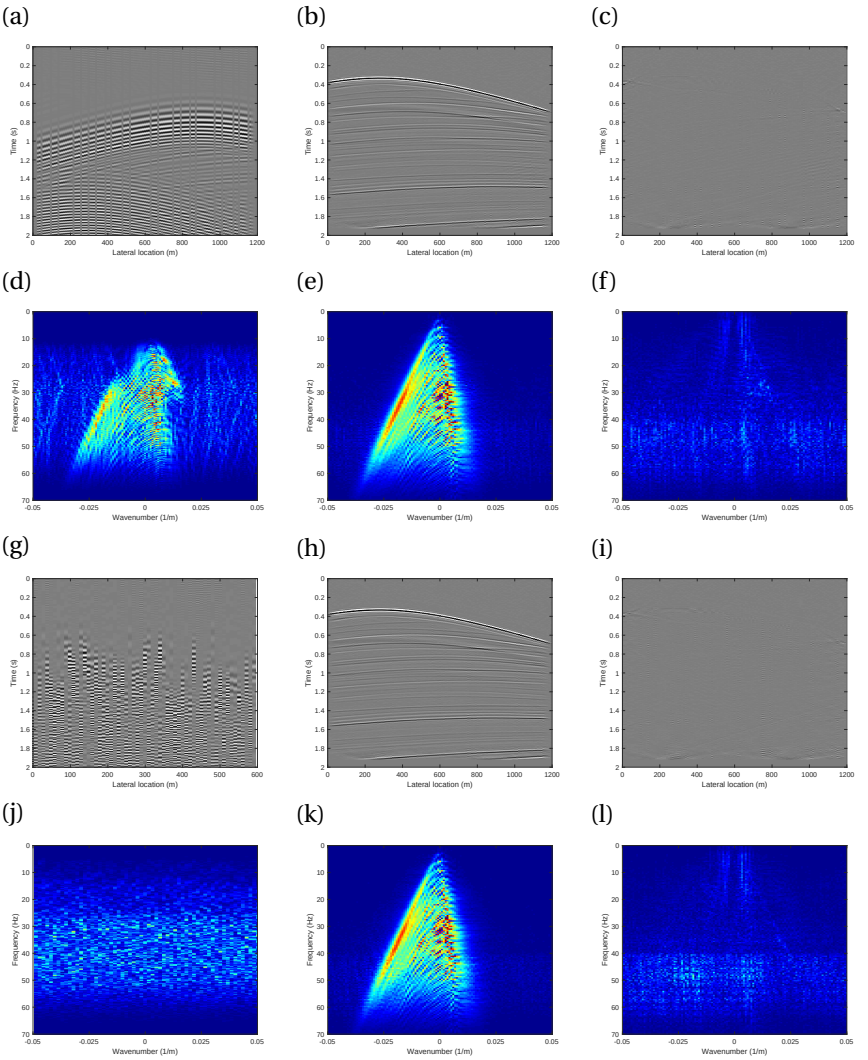

Figure 3.13: Blended and irregularly-sampled data (the proposed method) in the time-space domain and the frequency-wavenumber domain. (a)-(f) Data in the common source domain. (g)-(l) Data in the common detector domain. The left and middle columns show data before and after deblending and data reconstruction, respectively. The right column shows differences between the reference and estimated data. Difference plots in the frequency-wavenumber domain (f and l) are amplified by a factor of three.

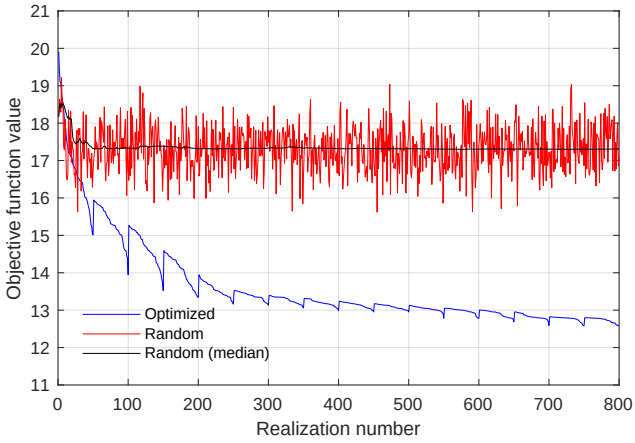

Figure 3.14: Objective function value at each realization. The blue and red lines represent objective function values from the proposed approach and random realization, respectively. The black dashed line indicates data having a median objective function value from random realizations.

3.5. OPTIMIZATION OF COST AND QUALITY

Seismic acquisition is almost always regarded as a trade-off between data quality and cost. These perspectives in a seismic survey are generally in conflict, where an improvement of one objective leads to a degradation of the other objective. In the previous sections, the numbers of blending fold, detectors and sources are kept constant throughout the iterations. They are implicitly regarded as budgetary constraints in our survey design problem. When there is an insufficient rationale for their choices, the procedure can also start with arbitrary selections. Further refinement of the constraints is quickly applicable to subsequent iterations based on the outcomes.

Another strategy for solving this trade-off problem is to find the Pareto optimal front via the use of multi-objective optimization. This allows us to choose the most appropriate solution from the Pareto front based on the current situation. Non-dominated sorting genetic algorithm (NSGA-II) is one of the widely-used approaches, in which the non-dominance concept was introduced into solution space [13].

This section describes an implementation of NSGA-II in a survey design problem that aims at deriving the Pareto optimal front of data quality and survey cost. The method seeks a set of optimal solutions that are equally good, known as Pareto-optimal solutions in terms of misfit, diversity and spread uniformity as shown in Figure 3.15.

The workflow used in this section attempts to design survey parameters responsible for source blending and spatial sampling of detectors and sources to match two con-

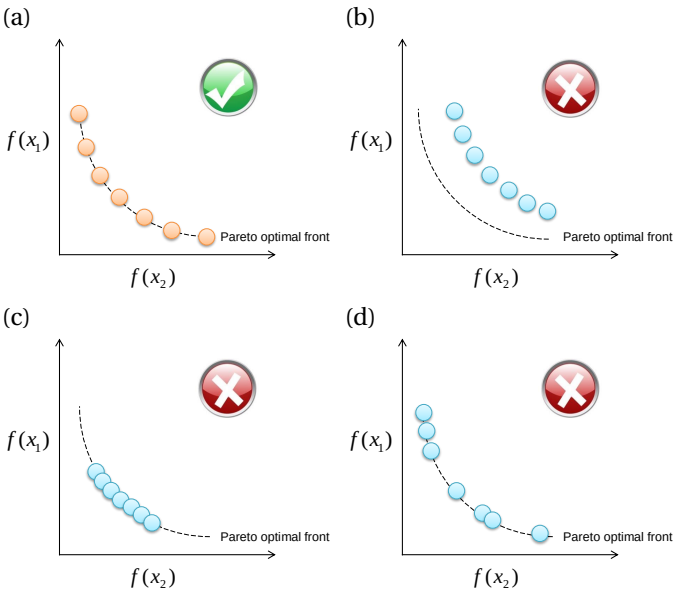

Figure 3.15: Schematics illustrating: (a) desired Pareto-optimal solutions and (b)-(d) undesired solutions in terms of misfit, diversity and spread uniformity, respectively.

tradictory objectives, i.e., quality and cost in a seismic survey. We derive an economic model of survey cost as functions of blending and spatial sampling schemes, which is used as one of two objectives to be optimized. Another objective is the quality of data recovery. Numerical examples using a 3D orthogonal geometry outline this implementation.

Based on the matrix notation proposed by Berkhout [14] and Kinneging *et al.* [15], Nakayama *et al.* [2] described the data arrangement for 3D geometries. In the 3D case, the data matrix consists of a set of submatrices, referred to as the cells (Figure 3.16). The x coordinates of detectors and the y coordinates of sources vary in the inner columns and rows within a cell, respectively. The y coordinates of detectors and the x coordinates of sources then vary in the outer columns and rows of the complete data matrix. 3D seismic data can be considered as a collection of 3D single-fold datasets such as 3D detector, shot and cross-spread gathers [16]. We assume no array response at detector or source side. A fully populated data matrix then equates to an ideal dataset with perfect spatial sampling, $\mathbf{X}$, where $\mathbf{D}$ and $\mathbf{S}$ become the identity matrices (see Equation 2.1). As shown in Figures 3.16b and c, each row and column of $\mathbf{X}$ represent a well-sampled 3D detector and shot gather, respectively. A given cell in $\mathbf{X}$ corresponds to a well-sampled cross-spread gather acquired by a perpendicular pair of one detector and one source line (Figure 3.16d).

For 3D geometries, we aim at an optimal retrieval of deblended and reconstructed single-fold data from blended and irregularly-sampled data. This study focuses on an

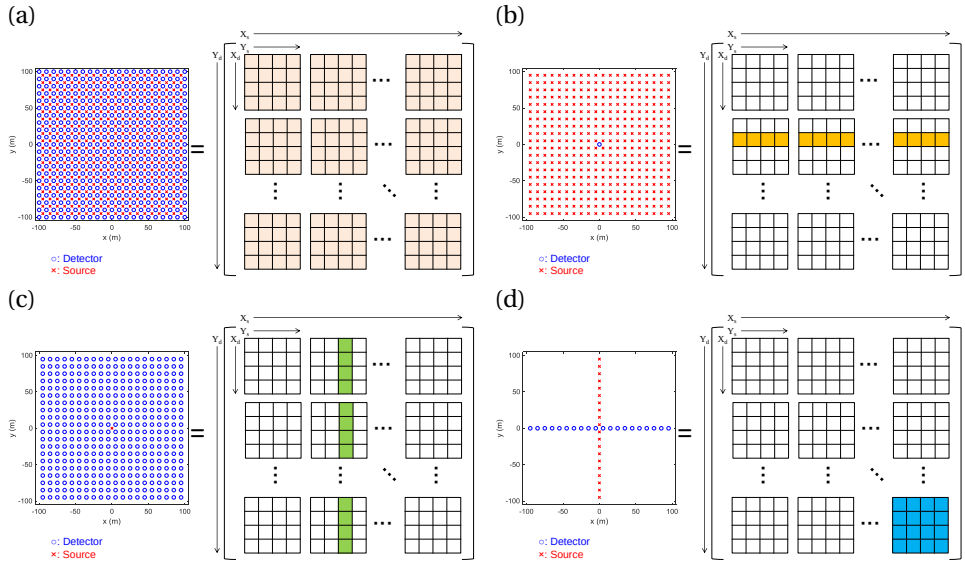

Figure 3.16: Matrix representation of 3D data. Xd, Yd, Xs and Ys indicate detector and source x-y coordinates. With perfect spatial sampling, each element of the complete data matrix becomes non-zero. Each row and column represent a 3D detector and shot gather, respectively. Each cell corresponds to a cross-spread gather.

orthogonal geometry that can be considered as a collection of 3D cross-spread gathers [16]. We describe a cross-spread gather acquired by the k^{th} detector line, and by the i^{th} source line as:

$$\mathbf{P}_i^k = \mathbf{D}_k \mathbf{X} \mathbf{S}_i. \tag{3.3}$$

As shown in Figure 3.16, when the k^{th} detector line and the i^{th} source line are well-sampled, $\mathbf{P}_i^k$ equates to one cell of $\mathbf{X}$. We describe a well-sampled cross-spread gather acquired by the k^{th} detector line and by the i^{th} source line as $\mathscr{X}_i^k$. With a 3D orthogonal geometry, multiple source lines can be acquired in a blended fashion [17]. In this case, a blended cross-spread gather can be defined by the contribution of a single detector line and multiple source lines. In this thesis, we consider a situation where a blended cross-spread gather is acquired by the k^{th} detector line as well as by the i^{th} and the j^{th} source lines as:

$$\mathbf{P'}^k_{i,j} = \mathbf{D}_k \mathbf{X} \mathbf{S'}_{i,j}, \tag{3.4}$$

where $\mathbf{S'}_{i,j}$ is the blended source matrix containing information on the i^{th} and the j^{th} source lines, which are acquired simultaneously. We applied our iterative scheme to design an optimum cross-spread geometry defined by $\mathbf{D}_k$ and $\mathbf{S'}_{i,j}$, which leads to satisfactory retrieval of $\langle \mathscr{X}_i^k \rangle$ and $\left\langle \mathscr{X}_j^k \right\rangle$ from $\mathbf{P'}^k_{i,j}$. The workflow tries to minimize the objective function based on the residual between ideal cross-spread gathers and estimated ones defined as:

$$J_{\text{Q}}(\mathbf{D}_k, \mathbf{S'}_{i,j}) = \sum_\omega \left\| \mathscr{X}_i^k - \left\langle \mathscr{X}_i^k \right\rangle \right\|_2^2 + \sum_\omega \left\| \mathscr{X}_j^k - \left\langle \mathscr{X}_j^k \right\rangle \right\|_2^2. \tag{3.5}$$

We also derive an economic model that describes a unit rate for blended acquisition. From an actual project that utilized 3D orthogonal geometries, we obtained survey rates (expressed in US dollar per square kilometer) with different detector and source densities, with different crew configurations, for both blended and unblended cases. This information allows us to estimate the following objective function responsible for a survey rate with given $\mathbf{D}_k$ and $\mathbf{S'}_{i,j}$:

$$J_{\mathrm{C}}(\mathbf{D}_k, \mathbf{S'}_{i,j}) = R_{\mathrm{s}} D_{\mathrm{s}} / F_{\mathrm{bl}} + (R_{\mathrm{d}} D_{\mathrm{d}} + \zeta F_{\mathrm{bl}} + \alpha) \times (T'/T), \tag{3.6}$$

where D_d and D_s indicate detector and source densities which are geometry dependent parameters. Terms R_{d} and R_{s} indicate rates that are related detector and source efforts, respectively. They are assumed to be proportional, respectively, to detector and source densities. Term F_{bl} is blending fold so this expression is also applicable to an unblended case where F_{bl} becomes one. As we assume source effort to be made solely during shooting, R_s is made inversely proportional to F_{bl}. Term ζ is a rate which increases proportionally with blending fold, e.g., source equipment. Terms T and T' are survey durations for a unblended case and a blended case with blending fold of F_{bl}, respectively. In Equation 3.6, D_{d}, D_{s} and F_{bl} are design-dependent parameters which can be obtained from $\mathbf{D}_k$ and $\mathbf{S'}_{i,j}$ whereas the remaining terms are project-dependent parameters. Due to the confidentiality, detailed figures cannot be disclosed. However, what can be mentioned here is that a linear trend line with intercept of zero and gradient of one achieves the r-squared value of 0.933 between actual survey rates and estimated ones using Equation 3.6. This indicates that our economic model fits to the real situation reasonably well. Nevertheless, the cost structure generally differs from one acquisition project to another. In practice, a tailored economical model that can fit each situation needs to be derived. Therefore, the ability of our approach to minimize J_{C} based on a given economic model should be focused in this section. Non-disclosure of actual survey rates has essentially no impact on assessing the capability of the proposed approach.

The overall acquisition-design scheme attempts to minimize J_{Q} and J_{C}:

$$\vec{J} = \begin{bmatrix} J_{\mathrm{Q}} \\ J_{\mathrm{C}} \end{bmatrix}. \tag{3.7}$$

To minimize the vectorized objective function in Equation 3.7, we utilize the NSGA-II approach [13]. Algorithm 2 illustrates the procedure to assess the individual solution. It starts with finding the first-rank solutions. This involves a calculation of two entities: (1) domination count $q_{g,p}$ (the number of solutions dominating a given solution, $\vec{C}_{g,p}$), and (2) a set of individuals, $\vec{Q}^0_{g,p}$, being dominated by $\vec{C}_{g,p}$. For all solutions with rank one, their domination counts become zero. For each member dominated by these solutions, its domination count is reduced by one. Any members having a zero domination count obtain rank two. This procedure is repeated until the ranks of all solutions are identified.

Additionally, to discriminate solutions with the same rank, we analyze their crowding distances. An infinite crowding distance is given to two solutions within the t^{th} rank having the maximum and the minimum value of a given objective function (in our case either J_{Q} or J_{C}). Crowding distance values for other solutions in the g^{th} generation are then calculated by the sum of individual distance values corresponding to each objective

function as:

$$d_{g,j} = \left| \frac{J_{\mathrm{Q}}(\vec{C}_{g,j+1}) - J_{\mathrm{Q}}(\vec{C}_{g,j-1})}{\max\limits_{j\in n_t} J_{\mathrm{Q}g,j} - \min\limits_{j\in n_t} J_{\mathrm{Q}g,j}} \right| + \left| \frac{J_{\mathrm{C}}(\vec{C}_{g,j+1}) - J_{\mathrm{C}}(\vec{C}_{g,j-1})}{\max\limits_{j\in n_t} J_{\mathrm{C}g,j} - \min\limits_{j\in n_t} J_{\mathrm{C}g,j}} \right|, \tag{3.8}$$

with

$$\forall\, j \in [2,\ldots,n_t-1], \quad \vec{C}_{g,j} \in \vec{F}_t, \tag{3.9}$$

where $\vec{F}_t$ is a set of solutions belonging to the t^{th} rank, and n_t is the number of solutions in $\vec{F}_t$. This ensures the diversity of the new generation by assigning a higher priority to a more isolated solution in the objective function space.

Figure 3.17 shows a velocity model consisting of horizontally flat layers along with a high-velocity geo-body. Figures 3.18a and b show synthesized cross-spread gathers derived from acoustic finite-difference modelling. They are considered as $\mathscr{X}_i^k$ and $\mathscr{X}_j^k$, respectively. Figures 3.18c and d show their detector and source geometries. A detector line and a source line are placed perpendicular to each other, along the x-axis and the y-axis, respectively. Detectors and sources are regularly deployed with a 10 m interval.

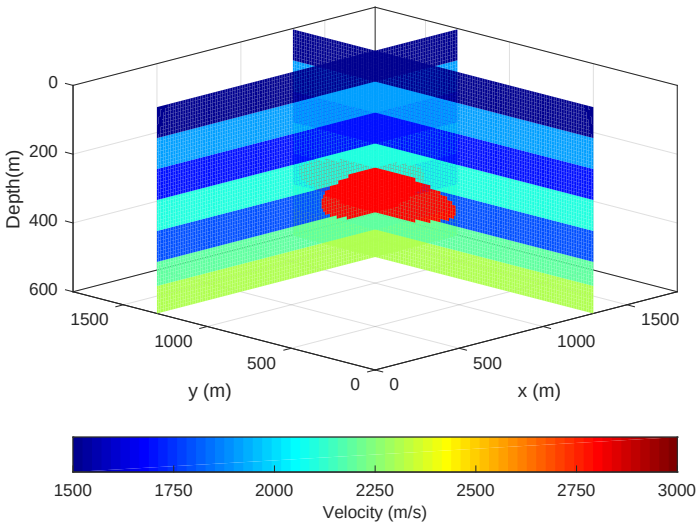

Figure 3.17: Velocity model used to derive synthetic datasets.

We update a set of three parameters responsible for spatial sampling of detectors and sources contributing to the two cross-spread gathers along with activation times applied to each source. We keep the blending fold of two where one source is activated along the i^{th} source line (x=600 m), while the other one travels along the j^{th} source line (x=1200 m). They employ a time shift ranging from 0 s to 0.256 s. Unlike examples in the previous sections, we allow the numbers of detectors and sources to be altered. An increase in these numbers can lead to minimizing J_{Q}, while it adversely affects J_{C}. Since

Algorithm 2 Fast non-dominated sort

Input: $\vec{C}_{0:g}(=\left[\vec{C}_0,\ldots,\vec{C}_g\right]^T)$ and $\vec{J}_{0:g}(=\left[\vec{J}_0,\ldots,\vec{J}_g\right]^T)$
Output: $\vec{F}_{1:t}(=\left[\vec{F}_1,\ldots,\vec{F}_t\right]^T)$

for each $\vec{C}_{k,h} \in \vec{C}_{0:g}$ **do**
  $\vec{Q}^0_{k,h} = \emptyset$ and $q_{k,h} = 0$
  for each $\vec{C}_{i,j} (\neq \vec{C}_{k,h}) \in \vec{C}_{0:g}$ **do**
    if $\vec{C}_{k,h}$ dominates $\vec{C}_{i,j}$ **then**
      Add $\vec{C}_{i,j}$ to a set of solutions, $\vec{Q}^0_{k,h}$
    else
      $q_{k,h} = q_{k,h} + 1$
    end if
  end for
  if $q_{k,h} = 0$ **then**
    Add $\vec{C}_{k,h}$ to solutions in the first rank, $\vec{F}_1$
  end if
end for
$t = 1$
while $\vec{F}_t \neq \emptyset$ **do**
  $\vec{Q} = \emptyset$
  for each $\vec{C}_{k,h} \in \vec{F}_t$ **do**
    for each $\vec{C}_{i,j} \in \vec{Q}^0_{k,h}$ **do**
      $q_{i,j} = q_{i,j} - 1$
      if $q_{i,j} = 0$ **then**
        Add $\vec{C}_{i,j}$ to a set of solutions, $\vec{Q}$
      end if
    end for
  end for
  $t = t + 1$
  Add $\vec{Q}$ to solutions in the t^{th} rank, $\vec{F}_t$
end while

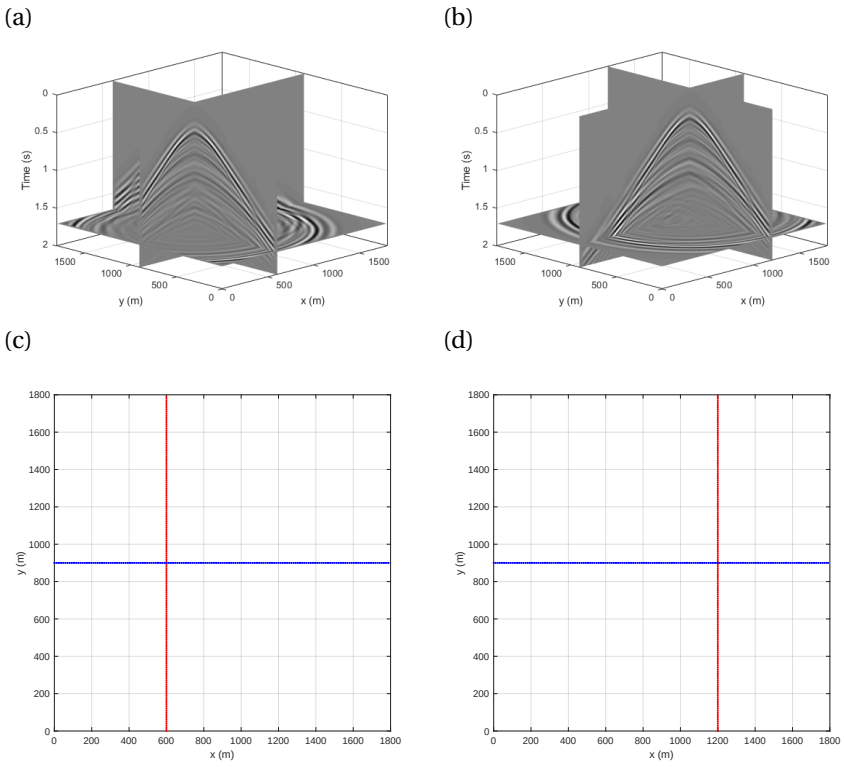

Figure 3.18: Input dataset (unblended and well-sampled cross-spread gathers). (a)-(b) 3D views of cross-spread gathers. (c)-(d) Applied detector (blue) and source (red) geometries

they apparently conflict with each other, we aim at attaining solutions along the Pareto optimal front of these two objective functions.

Figure 3.19 shows the optimization result. The vertical axis corresponds to the scaled survey rate which can be a representation of J_C. The horizontal axis then indicates the mean value of signal-to-noise ratio (SNR) values obtained from two deblended and reconstructed cross-spread gathers. The SNR of a cross-spread gather acquired by the k^{th} detector line and the i^{th} source line is given by:

$$\text{SNR}_i^k = 10\log_{10}\left(\frac{\sum_\omega \left\|\mathscr{X}_i^k\right\|_2^2}{\sum_\omega \left\|\mathscr{X}_i^k - \langle\mathscr{X}_i^k\rangle\right\|_2^2}\right). \tag{3.10}$$

This SNR definition enables a direct comparison between the desired output and estimated data. Since we deal with acquisition design, this permits $\mathscr{X}_i^k$ to be known, making this quantitative measurement applicable to our case.

The red circle markers indicate 50 realizations from the initial population where survey parameters are arbitrarily derived. The blue circle markers correspond to solutions from the latest population after 1000 realizations. We provide three results indicated by

magenta, cyan and green dots in Figure 3.19. The magenta dot is called "random design" which exemplifies a situation where we arbitrary derive survey parameters. The cyan dot, called "quality design", represents a case where we update survey parameters in a quality-oriented manner, while its survey rate is still comparable to that of the random design. The green dot, called "economic design", is the optimized solution for a cost-oriented purpose, while the resultant SNR value is still comparable to that of the random design.

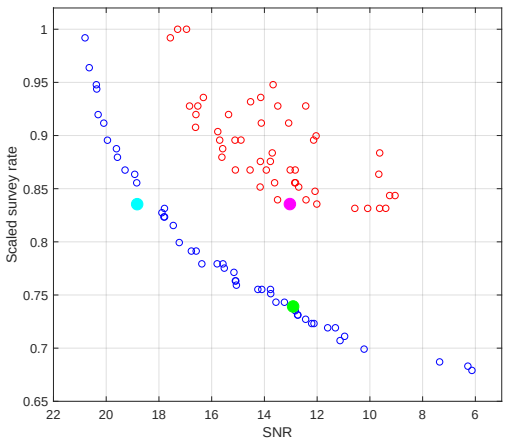

Figure 3.19: Optimization results. Red circle markers indicate 50 realizations from the initial population. Blue circle markers correspond to solutions from the latest population after 800 realizations. The magenta dot, the cyan dot and the green dot indicate results of "random design", "quality design" and "economic design", respectively.

Figure 3.20 compares acquisition geometries among three scenarios. Figures 3.21, 3.22 and 3.23 show shot records from sources located around y=900 m from the previously described three designs. Each case achieves reasonable deblending and data reconstruction. However, larger recovery errors are still recognizable in difference plots for the random and economic designs as compared to the quality design.

Wide-azimuth sampling corresponds to recording a full representation of the seismic wavefield. A broad range of azimuths is of substantial value in enhancing the illumination beneath complex geology. The technique is also capable of providing more insight into reservoir properties such as fracture and stress characteristics of the field. In wide-azimuth data, it is, hence, desirable to obtain satisfactory data quality among different offsets and azimuths. We analyze the SNR for different subsets within a 3D cross-spread gather, each of which consists of traces having similar offset and azimuth ranges. This subset is also known as an offset vector tile (OVT) [16]. We describe offset and azimuth ranges of a given OVT as a tile (l, m). The number l defines detectors contributing to a tile (l,m). These detectors are located from (l-1)×100 m to l×100 m along the x-axis. Similarly, tile number m defines sources contributing to a tile (l, m). These sources are

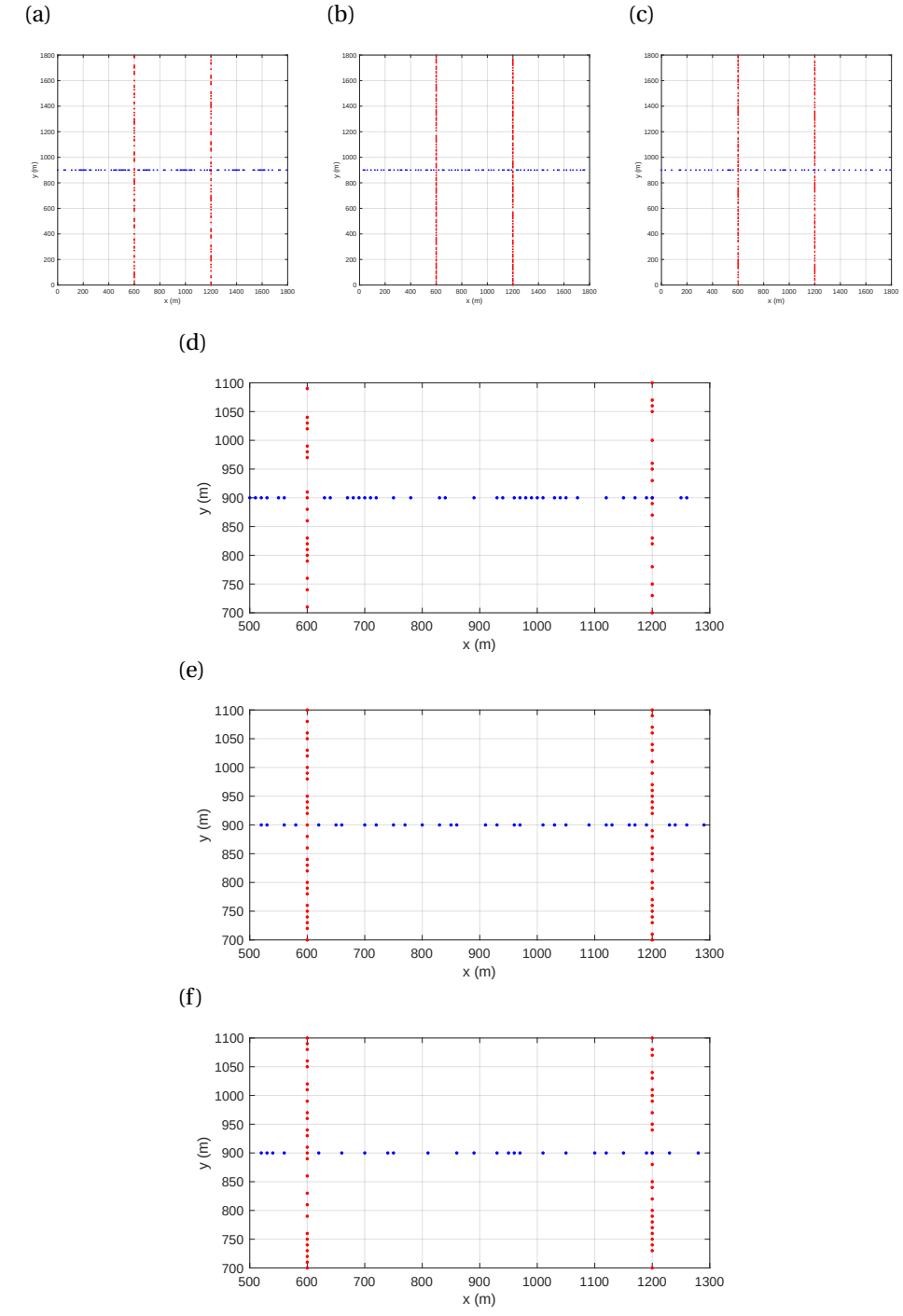

Figure 3.20: Comparison of acquisition geometries. (a)-(c) Random, quality and economic design, respectively. (d)-(e) zoomed views of top figures.

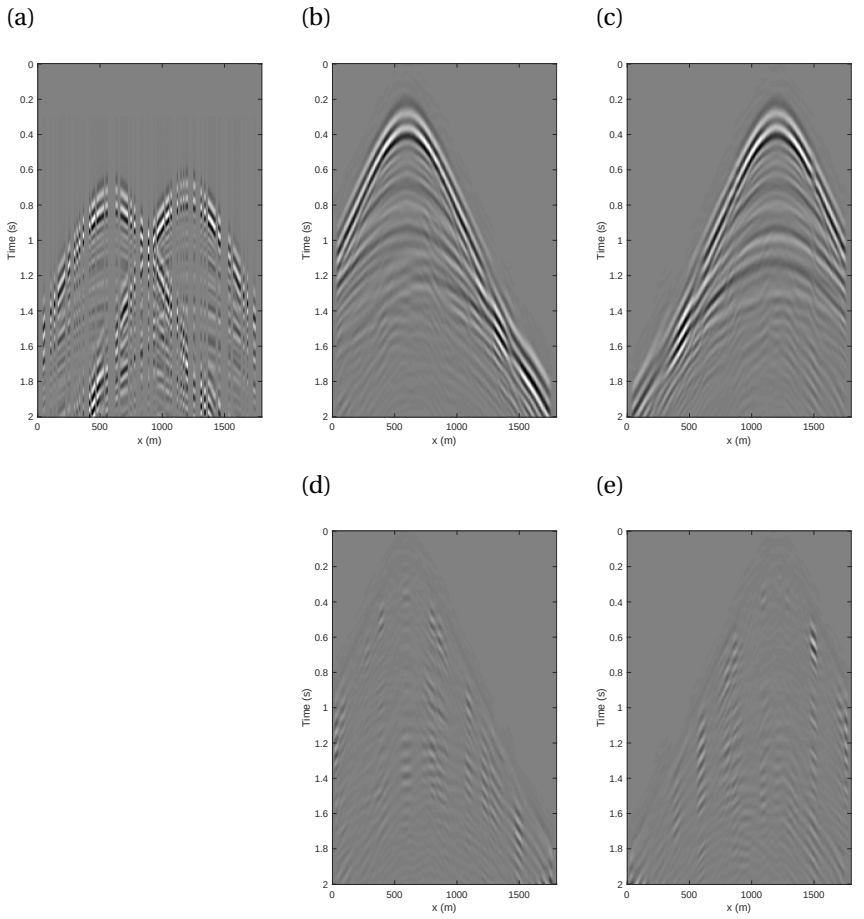

Figure 3.21: Shot records from random design. (a) Blended and irregularly-sampled data, $\mathbf{P'}^{k}_{i,j}$. (b) and (c) Deblended and reconstructed data, $\left\langle \mathscr{X}^{k}_{i} \right\rangle$ and $\left\langle \mathscr{X}^{k}_{j} \right\rangle$. (d) and (e) Difference, $\mathscr{X}^{k}_{i} - \left\langle \mathscr{X}^{k}_{i} \right\rangle$ and $\mathscr{X}^{k}_{j} - \left\langle \mathscr{X}^{k}_{j} \right\rangle$.

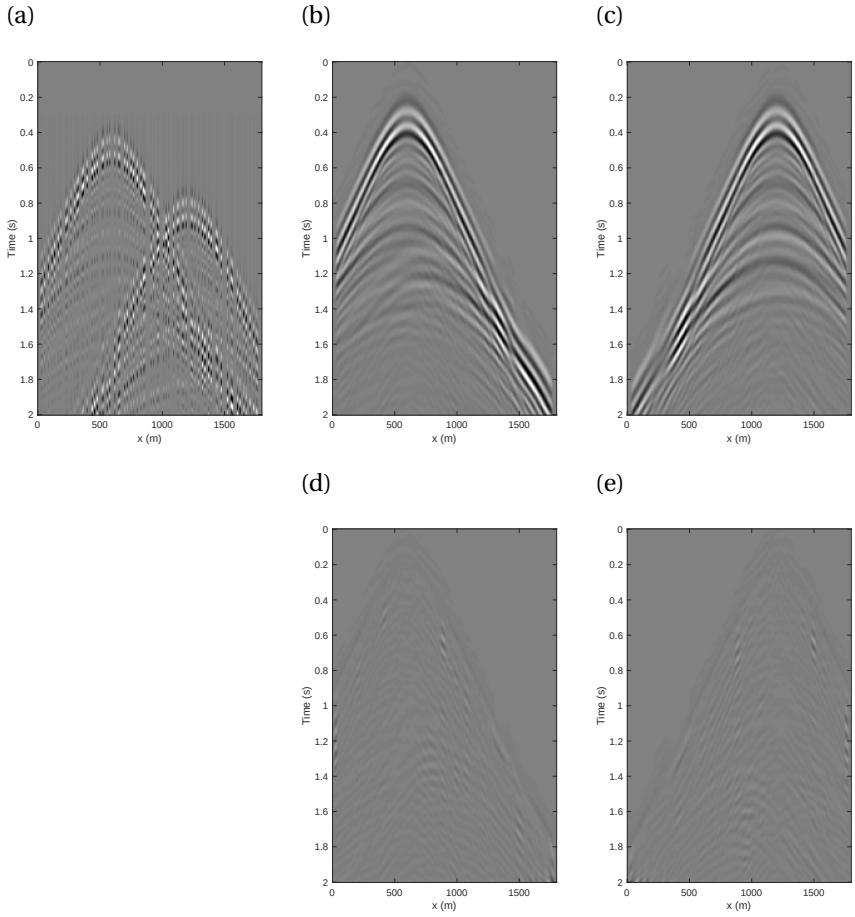

Figure 3.22: Shot records from quality design. (a) Blended and irregularly-sampled data, $\mathbf{P'}^{k}_{i,j}$. (b) and (c) Deblended and reconstructed data, $\left\langle \mathscr{X}_i^k \right\rangle$ and $\left\langle \mathscr{X}_j^k \right\rangle$. (d) and (e) Difference, $\mathscr{X}_i^k - \left\langle \mathscr{X}_i^k \right\rangle$ and $\mathscr{X}_j^k - \left\langle \mathscr{X}_j^k \right\rangle$.

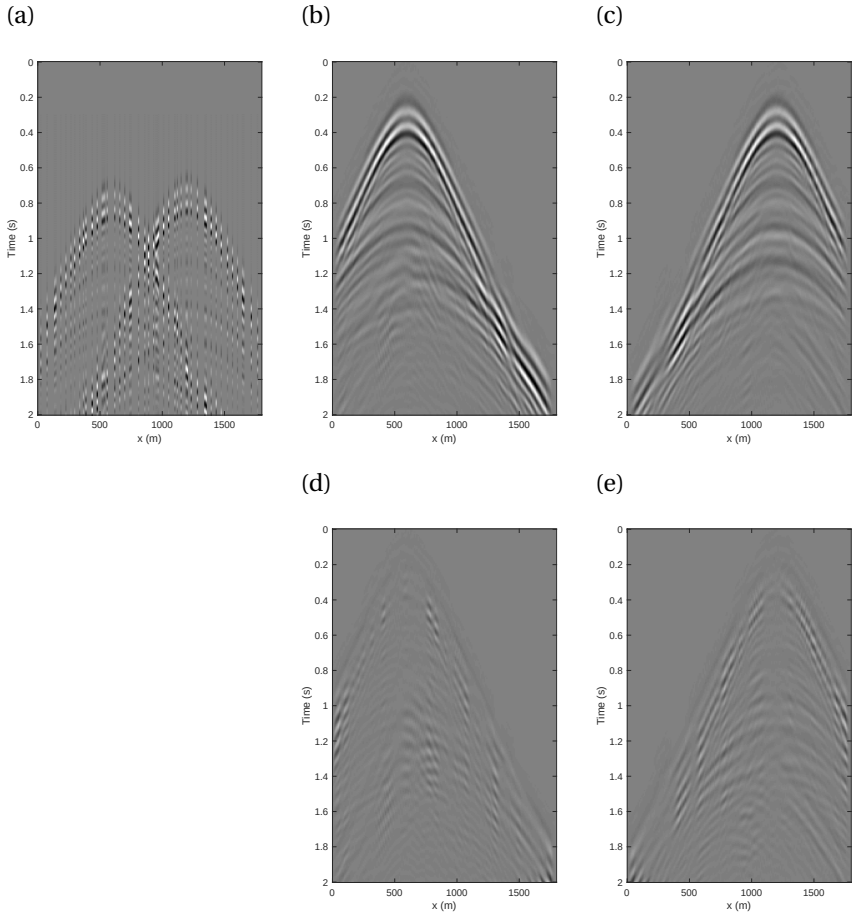

Figure 3.23: Shot records from economic design. (a) Blended and irregularly-sampled data, $\mathbf{P'}^{k}_{i,j}$. (b) and (c) Deblended and reconstructed data, $\left\langle \mathscr{X}^{k}_{i} \right\rangle$ and $\left\langle \mathscr{X}^{k}_{j} \right\rangle$. (d) and (e) Difference, $\mathscr{X}^{k}_{i} - \left\langle \mathscr{X}^{k}_{i} \right\rangle$ and $\mathscr{X}^{k}_{j} - \left\langle \mathscr{X}^{k}_{j} \right\rangle$.

located from (m-1)×100 m to m×100 m along the y-axis. For example, tile (1, 1) indicates the OVT acquired by detectors located from 0 m to 100 m along the x-axis and sources located from 0 m to 100 m along the y-axis. Figure 3.24 shows SNR values of different OVTs within cross-spread gathers for the three acquisition scenarios. The random design and economic design are fairly comparable although the economic design leads to roughly 12% reduction in the survey rate (Figure 3.19). The quality design attains higher SNR values in almost all the OVTs, which helps us to ensure amplitude variation with offset (AVO) fidelity and/or amplitude variation with offset and azimuth (AVOAz) fidelity of the data.

Figure 3.25 compares detector and source geometries for the solutions shown in Figure 3.19. The diamond markers indicate solutions from the initial population whereas the circle markers indicate solutions from the latest population. Plot colour in the three sub-plots indicates detector, source and trace density, respectively. For a well-sampled cross-spread gather, these density values become one. For solutions with a given SNR value or a given survey rate, the optimized designs tend to employ fewer detectors than the designs from the initial population (Figures 3.25a and b). In general, there is a certain imbalance between the detector and source effort, which is the case for the applied field example where deployment of detectors is more expensive than deployment of sources. This consequently makes detector decimation contribute more effectively to reducing the survey cost than source decimation. Based on this imbalance, the algorithm identifies optimum detector and source distributions that, on the one hand, contribute to reducing survey cost, yet, on the other hand, enhance data quality through the course of iterations. As shown in Figure 3.25c, optimized designs require smaller trace densities to attain equivalent SNR values as compared to random designs. Alternatively, optimized designs attain higher SNR values with equivalent trace densities and/or survey rates.

NSGA-II applied to this study is capable of handling two conflicting objectives, i.e., cost and quality. Our implementation successfully diversifies and spreads out the solutions, and consequently derives the Pareto optimal front of our acquisition design problem. All solutions along the Pareto optimal front can be regarded as equally desirable solutions. Among these solutions, we can make a decision to identify the one that fits the objective of the seismic survey.

3.6. DISCUSSION

In practice, certain acquisition errors in designed parameters are inevitably anticipated even when extensive quality control is provided in the field. The outcomes from our iterative process provide some insights into the sensitivity of the proposed workflow with respect to tolerance in $\mathbf{D}$, $\mathbf{S}$ and $\mathbf{\Gamma}$. To quantitatively describe a difference in survey parameters between two given designs, we define the following dimensionless parameter:

$$\kappa_{i,j} = \lambda_{\mathrm{d}} \frac{\psi^{(\mathrm{d})}_{i,j} - \min \psi^{(\mathrm{d})}_{i,j}}{\max \psi^{(\mathrm{d})}_{i,j} - \min \psi^{(\mathrm{d})}_{i,j}} + \lambda_{\mathrm{s}} \frac{\psi^{(\mathrm{s})}_{i,j} - \min \psi^{(\mathrm{s})}_{i,j}}{\max \psi^{(\mathrm{s})}_{i,j} - \min \psi^{(\mathrm{s})}_{i,j}} + \lambda_{\gamma} \frac{\psi^{(\gamma)}_{i,j} - \min \psi^{(\gamma)}_{i,j}}{\max \psi^{(\gamma)}_{i,j} - \min \psi^{(\gamma)}_{i,j}}, \quad (3.11)$$

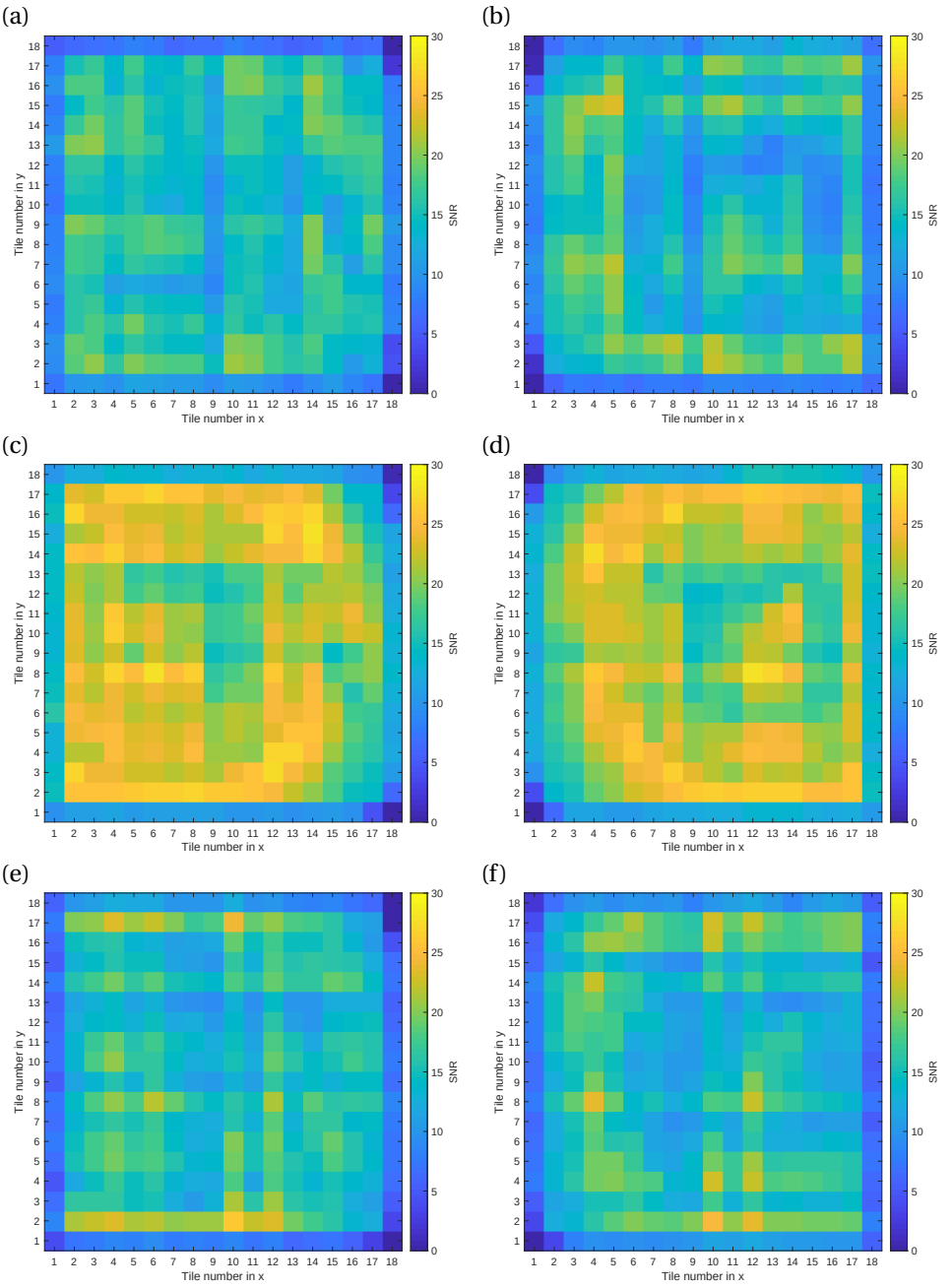

Figure 3.24: SNR values of OVTs. SNR values of $\left\langle \mathscr{X}_i^k \right\rangle$ and $\left\langle \mathscr{X}_j^k \right\rangle$, (a)-(b) for the random designs, (c)-(d) for the quality designs and (e)-(f) for the economic design.

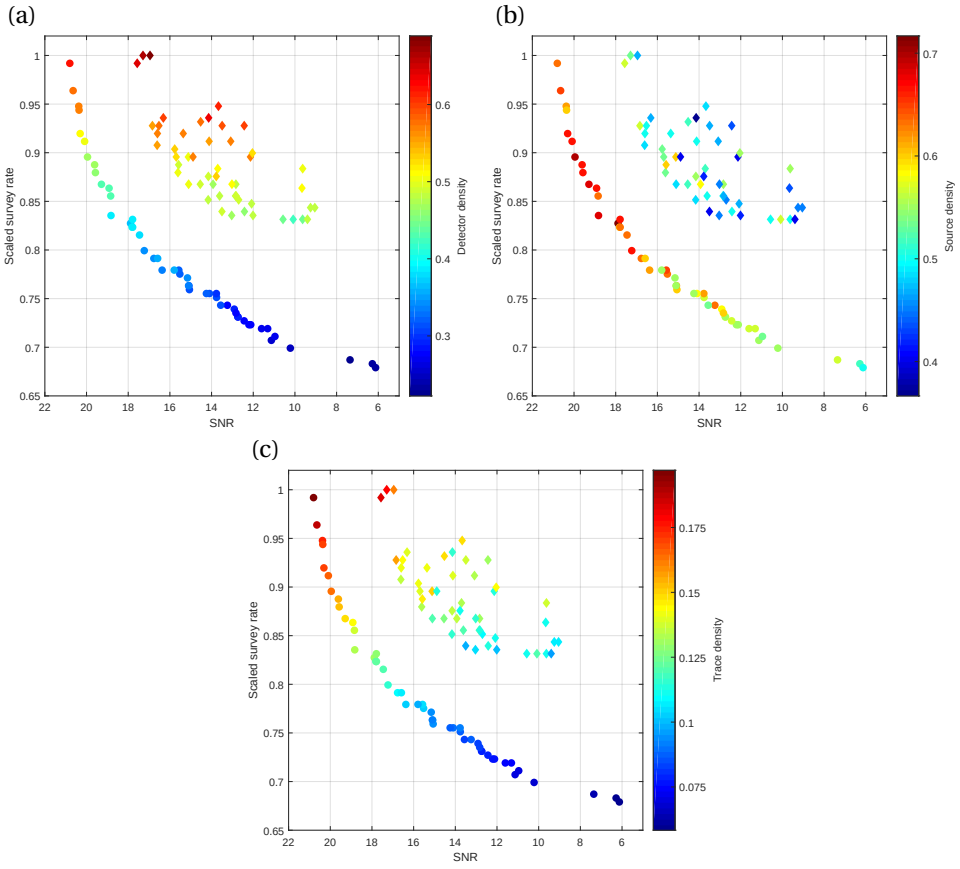

Figure 3.25: Comparison of acquisition geometries among solutions shown in Figure 3.19. (a) Detector density. (b) Source density. (c) Trace density. Diamond markers indicate solutions in the initial population. Circle markers indicate solutions in the latest population.

where

$$\psi_{i,j}^{(\mathrm{d})} = \frac{\vec{d}_i^T \cdot \vec{d}_j}{\left\|\vec{d}_i\right\|_2 \cdot \left\|\vec{d}_j\right\|_2}, \quad \psi_{i,j}^{(\vec{s})} = \frac{\vec{s}_i^T \cdot \vec{s}_j}{\|\vec{s}_i\|_2 \cdot \left\|\vec{s}_j\right\|_2}, \quad \psi_{i,j}^{(\tau)} = \frac{\vec{\gamma}_i^T \cdot \vec{\gamma}_j}{\left\|\vec{\gamma}_i\right\|_2 \cdot \left\|\vec{\gamma}_j\right\|_2}, \quad i \neq j. \tag{3.12}$$

Vectors $\vec{d}_i$, $\vec{s}_i$ and $\vec{\gamma}_i$ contain information on the spatial sampling of detectors, that of sources and blending codes applied to the i^{th} design, respectively (see Chapter 2 for more details on the way to derive $\vec{d}$, $\vec{s}$ and $\vec{\gamma}$). Terms $\psi_{i,j}^{(\mathrm{d})}$, $\psi_{i,j}^{(\mathrm{s})}$ and $\psi_{i,j}^{(\gamma)}$ indicate correlation between survey parameters applied to the i^{th} design and the j^{th} design in terms of $\vec{d}$, $\vec{s}$ and $\vec{\gamma}$, respectively. Terms λ_{d}, λ_{s} and λ_{γ} are user-defined weights. In this study, we weigh the three terms equally by setting each of them equal to one, making $\kappa_{i,j}$ vary from 0 to 3. A large value of $\kappa_{i,j}$ means that the i^{th} design and the j^{th} design employ similar survey parameters, while a small value of $\kappa_{i,j}$ indicates a large difference between the two. We analyze the best 300 designs among the 800 realizations derived from our workflow shown in the marine DSA example (section 3.3). This provides 194850 combinations of i and j in Equation 3.11, i.e., $\forall\, i \in \{1,2,\ldots,300\}$ and $\forall\, j \in \{2,3,\ldots,800\}$ where the solutions are sorted into ascending order according to their objective function values. Figure 3.26 contains a density plot of all 194850 $\kappa_{i,j}$ values versus the corresponding absolute difference between the objective function values of the i^{th} and j^{th} design-pair. This analysis infers possible consequences caused by a change in survey parameters from one design to another. There is a clear trend where the absolute differences are inversely proportional to κ values. This observation indicates that minor or partial alterations in acquisition parameters would not severely degrade the quality of deblending and data reconstruction. On the other hand, large acquisition errors likely lead to an unforeseeable consequence. Anticipated acquisition errors are subject to various factors including, but not limited to, the type of acquisition system, the environment, activities and operations within as well as around the field. Therefore, a case-by-case analysis is worthwhile to further envision significances of acquisition errors anticipated in the area of interest.

We also investigate applicability of the optimized parameters obtained from a given area to other areas having different geological contexts. Marine DSA scenarios are numerically simulated using eight different subsets within the Marmousi model. We first optimize the blending and sampling operators of the detectors and four DSA source units in a given subset called model 1. The optimized operators from model 1, $\mathbf{D}_1$, $\mathbf{S}_1$ and $\mathbf{\Gamma}_1$, are then applied to other subsets within the Marmousi model, called models 2-8 as:

$$\begin{pmatrix} \mathbf{P}_1{}' \\ \mathbf{P}_2{}' \\ \vdots \\ \mathbf{P}_8{}' \end{pmatrix} = \begin{pmatrix} \mathbf{D}_1\mathbf{X}_1\mathbf{S}_1\mathbf{\Gamma}_1 \\ \mathbf{D}_1\mathbf{X}_2\mathbf{S}_1\mathbf{\Gamma}_1 \\ \vdots \\ \mathbf{D}_1\mathbf{X}_8\mathbf{S}_1\mathbf{\Gamma}_1 \end{pmatrix}, \tag{3.13}$$

where $\mathbf{X}_i$ ($i = 1,2,\ldots,8$) indicates eight different subsets of the Marmousi model. These data are compared to those with randomly designed operators. Each dataset has the

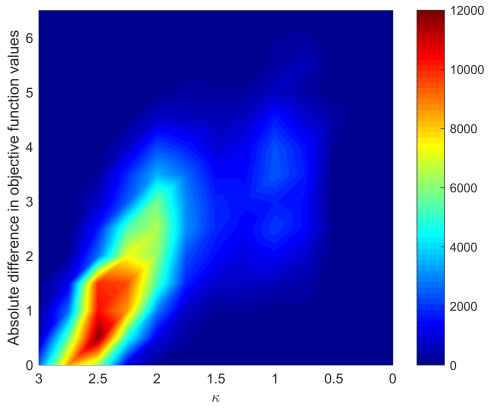

Figure 3.26: Density plot of κ and absolute difference in objective function values. The warmer colour indicates higher density having more data points within a given range of two variables. A clear trend where the absolute difference is inversely proportional to κ is easily recognizable. This indicates that a minor or partial tolerance in survey parameters would not severely affect the quality of deblending and data reconstruction. On the other hand, large acquisition errors likely lead to large uncertainty in the quality of the outcome.

same blending fold and the same numbers of detectors and sources. Figure 3.27 compares deblending and reconstruction results for each model. Although the operators are established using model 1, these parameters reasonably achieve a notable enhancement in all cases. This clearly illustrates that the optimized blending and sampling operators from model 1 provide a certain uplift on the deblending and reconstruction quality in other models. The difference in objective function values among models is presumably attributable to the subsurface complexity that varies from one model to another. For instance, models 6-8 cover faulting regions. These geological complexities likely make deblending and reconstruction more challenging. On the other hand, models 2-5 employ relatively simple structures . Nevertheless, optimized operators yield better deblending and reconstruction results for all models. This suggests that optimized operators using our approach possibly enhance these processes for an area having similar subsurface responses. Although further study is required, this possibly implies that optimization at certain locations representing the area of interest sufficiently provides effective operators applicable to the entire field without the need for the location-by-location update of the survey parameters.

Even though the forward and inverse models used in our workflow can be applied to various types of seismic surveys, the proposed workflow is also capable of accommodating alternative deblending and data reconstruction schemes. Additionally, the implementation of other optimization methods for updating survey parameters is fairly straightforward. Hence, the contents of the proposed workflow are freely and easily adjustable to make it suitable for a specific purpose in the area of interest. The selection can be subject to geological and geophysical contexts, operational and regulatory requirements, available resources and even any technical preferences. Nevertheless, the

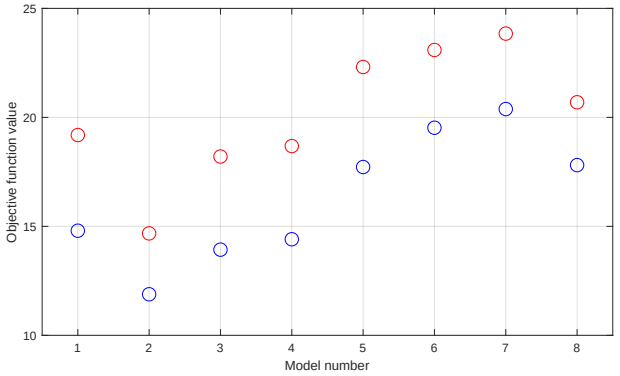

Figure 3.27: Objective function values from different models. Blue circles indicate objective functions from the optimized design, while red circles indicate objective functions from random designs. For results represented by blue circles, sampling and blending operators are established with model 1 and then applied to other models.

proposed approach can effectively and efficiently deal with the significantly large problem space that is inherent to the optimization of blending and sampling operators. As demonstrated in this study, our workflow successfully provides optimum solutions that enhance the performance of deblending and data reconstruction. Both GAs and CNNs possess a great advantage of flexibility allowing us to adapt them to particular problem domains. Although the proposed workflow does not necessarily guarantee the global convergence, acceptable solutions are attainable in a computationally efficient manner.

In sections 3.3 and 3.4, the numbers of blending fold, detectors and sources are kept constant throughout the iterations. They are implicitly regarded as budgetary constraints in our survey design problem. When there is an insufficient rationale for their choices, the procedure can also start with arbitrary selections. Further refinement of the constraints is quickly applicable to subsequent iterations based on the outcomes. The use of multi-objective optimizations such as NSGA-II can be considered as a good alternative when a reliable economic model for a given project is available. In the provided example (section 3.5), our implementation successfully diversifies and spreads out the solutions, and consequently derives survey designs along the Pareto optimal front of cost and quality. This consequently allows us to find a suitable option that can satisfy both geophysical and business objectives in the project.

The proposed workflow can be of help to a health, safety and environment (HSE) perspective. As mentioned previously, improvement of survey efficiency by the use of blending and sparse geometries leads to reduction of the operational risks and environmental footprint in the field. Furthermore, properly designed source signatures utilizing the DSA concept prevent unnecessary acoustic exposures to the environment, while satisfactory data quality is still attainable. The proposed workflow helps us to design blending operators including technically, operationally and environmentally favourable encoded signatures. In addition, the spatial distribution of the detectors and encoded

sources can be optimized to comply with HSE requirements, while ensuring the quality of the subsequent deblending and data reconstruction.

3.7. CONCLUSIONS

The iterative scheme for acquisition design applied in this chapter aims to find optimum survey parameters that define the source blending and the spatial sampling of detectors and sources. The results from this study clearly show the variation of deblending and data reconstruction quality, attributable solely to the design of survey parameters. Optimizing them enhances the performance of deblending and data reconstruction. The proposed approach integrates a GA and a CNN to make optimization feasible within an affordable computation time. Genetic operators are capable of simultaneously updating the survey parameters, even in the case of complex blending and irregular spatial sampling schemes that employ the DSA concept. The network architecture used for this study successfully relates the performance of deblending and data reconstruction to the choice of survey parameters. The classification through the CNN helps us to minimize the computation of suboptimal designs, while keeping the optimal ones in the iterative scheme. The proposed method is widely applicable. Our forward modelling enables us to simulate several scenarios that resemble acquisition in different environments. The inverse model then makes robust deblending and reconstruction of these data achievable. A possible solution to optimize conflicting multi-objectives, i.e., cost and quality in data acquisition, is also described using NSGA-II for the case where an economic model of a survey is available. The iterative scheme presented in this chapter provides survey parameters that lead to improved deblending and reconstruction quality. As a consequence, resultant acquisition scenarios allow us to properly manage the demanding objectives in terms of quality, cost, efficiency and HSE perspectives.

REFERENCES

[1] S. Nakayama, G. Blacquière, T. Ishiyama, and S. Ishikawa, *Blended-acquisition design with irregular geometries for wide-azimuth sampling,* 88th SEG Annual Meeting, Anaheim, California, USA, Expanded Abstracts, 126 (2018).

[2] S. Nakayama, G. Blacquière, T. Ishiyama, and S. Ishikawa, *Blended-acquisition design of irregular geometries towards faster, cheaper, safer and better seismic surveying,* Geophysical Prospecting **67**, 1498 (2019).

[3] S. Nakayama, G. Blacquière, and T. Ishiyama, *Automated survey-design for blended-acquisition with irregular spatial sampling via the integration of a metaheuristic and deep learning,* Geophysics **84**, P47 (2019).

[4] S. Nakayama and G. Blacquière, *Automated Survey Design for Land Acquisition Using the Dispersed Source Array Concept,* New Advances in Land Geophysical Acquisition Technologies Workshop, Muscat, Oman (2019).

[5] A. J. Berkhout, *Blended acquisition with dispersed source arrays,* Geophysics **77**, A19 (2012).

[6] M. Caporal, G. Blacquière, and M. Davydenko, *Broadband imaging via direct inversion of blended dispersed source array data,* Geophysical Prospecting **66**, 942 (2018).

[7] C. Li, C. C. Mosher, L. C. Morley, Y. Ji, and J. D. Brewer, *Joint source deblending and reconstruction for seismic data,* 83rd SEG Annual Meeting, Houston, Texas, USA, Expanded Abstracts, 82 (2013).

[8] J. Cheng and M. D. Sacchi, *Separation and reconstruction of simultaneous source via iterative rank reduction,* Geophysics **80**, V57 (2015).

[9] J. Cao, E. Verschuur, H. Gu, and L. Li, *Joint deblending and data reconstruction with focal transformation,* Geophysics **84**, V219 (2019).

[10] A. Mahdad, P. Doulgeris, and G. Blacquière, *Separation of blended data by iterative estimation and subtraction of blending interference noise,* Geophysics **76**, Q9 (2011).

[11] T. Ishiyama, M. Y. Ali, S. Ishikawa, G. Blacquière, and S. Nakayama, *Research note: Deblended-data reconstruction using generalized blending and deblending models,* Geophysical Prospecting **67**, 1852 (2019).

[12] A. J. Berkhout and G. Blacquière, *Effect of noise in blending and deblending,* 83rd SEG Annual Meeting, Houston, Texas, USA, Expanded Abstracts, 94 (2013).

[13] K. Deb, A. Pratap, S. Agarwal, and T. Meyarivan, *A fast and elitist multiobjective genetic algorithm: NSGA-II,* IEEE Transactions on Evolutionary Computation **6**, 182 (2002).

[14] A. J. Berkhout, *Seismic migration, imaging of acoustic energy by wave field extrapolation, Part A: theoretical aspects* (Elsevier, 1982).

[15] N. A. Kinneging, V. Budejicky, C. P. A. Wapenaar, and A. J. Berkhout, *Efficient 2D and 3D shot record redatuming,* Geophysical Prospecting **37**, 493 (1989).

[16] G. J. O. Vermeer, *3D Seismic Survey Design, Second Edition* (Society of Exploration Geophysicists, 2012).

[17] S. Nakayama, G. Mercado, M. Benson, K. Belaid, and M. Garden, *Field-wide implementation of time and distance separated source techniques on a 3D OBC survey offshore Abu Dhabi, UAE,* First Break **33**, 47 (2015).

4

TOWARDS OPTIMUM SUBSURFACE PROPERTY ESTIMATION

Blended acquisition along with efficient spatial sampling is capable of providing high-quality seismic data in a cost-effective and productive manner. While deblending and data reconstruction conventionally accompany this way of data acquisition, alternatively, the recorded data can be processed directly to estimate subsurface properties. We establish a workflow to design survey parameters that account for the source blending as well as the spatial sampling of sources and detectors. The proposed method involves an iterative scheme to derive the survey design, leading to optimum reflectivity and velocity estimation via joint migration inversion. In the workflow, we extend the standard implementation of joint migration inversion to cope with the data acquired in a blended fashion along with irregular detector and source geometries. This makes a direct estimation of reflectivity and velocity models feasible without the need of deblending or data reconstruction. During the iterations, the errors in reflectivity and velocity estimates are used to update the survey parameters by integrating a genetic algorithm and a convolutional neural network. Bio-inspired operators enable the simultaneous updates of the blending and sampling operators. To relate the choice of survey parameters to the performance of joint migration inversion, we utilize a convolutional neural network. The applied network architecture discards suboptimal solutions among newly generated ones. Conversely, it carries optimal ones to the subsequent step, which improves the efficiency of the proposed approach. The resultant acquisition scenario yields a notable enhancement in both reflectivity and velocity estimation attributable to the choice of survey parameters.

Parts of this chapter are available in a reference [1].

4.1. INTRODUCTION

In this chapter, we describe a survey design workflow that iteratively optimizes the survey parameters related to both the blending and spatial sampling of detectors and sources, leading to satisfactory reflectivity and velocity estimation via joint migration inversion (JMI). JMI is an inversion process that derives a high-resolution subsurface reflectivity model as well as a migration velocity model by estimating two independent operators responsible for reflection and propagation [2, 3]. We extend the standard JMI implementation to handle blended and irregularly-sampled data, which is then incorporated into the proposed survey design. The workflow utilizes errors in reflectivity and velocity estimates from the JMI process for a given survey design. They are assigned to its objective function and are subsequently input into a survey-parameter update system based on the integration of a genetic algorithm (GA) and a convolutional neural network (CNN) as described in Chapter 2. Stochastic operators in the GA that imitate the theory of natural evolution allow for simultaneous updates of the blending and sampling operators towards optimum JMI results. The implementation of the CNN aids the population management in our GA by selecting high potentials, while discarding low potentials among newly generated solutions from genetic operators. Only survey designs classified as high potentials in the CNN are fed into the subsequent step that involves the evaluation of the objective function through JMI. Since JMI is computationally expensive, the use of an antecedent classifier effectively prevents wasteful computation incurred to suboptimal solutions, which consequently enhances the performance of the overall scheme. We also incorporate the dispersed source array (DSA) concept [4] in the proposed survey design. This technique utilizes a plurality of source types, each having a dedicated narrow bandwidth. This permits each narrow-band source to be independently deployed to satisfy its own spatial sampling criteria determined by its frequency range and noise considerations. Caporal *et al.* [5] extensively discussed its advantages in terms of geophysical, operational and environmental perspectives.

In our acquisition design, the aim is to find the optimum blending and spatial sampling schemes, contributing to efficiency, economics and health, safety and environment (HSE), that satisfy the geophysical objectives without relying on an expensive survey acquired in an unblended and regularly well-sampled fashion. Our main objective in this chapter is twofold: (1) to explore the effect of the choice of survey parameters on the performance of JMI, and (2) to illustrate the proposed workflow. Numerical examples provide the results of our approach that aims to enhance the JMI results by simultaneously updating different survey parameters involved in DSA acquisition.

4.2. SURVEY DESIGN WORKFLOW

Figure 4.1 illustrates the proposed survey design to find optimum $\mathbf{D}$, $\mathbf{S}$ and $\mathbf{\Gamma}$, while we assume $\mathbf{R}$ and $\mathbf{W}$, which represent all relevant seismic information of the subsurface, to be available as prior information. Such information is available, e.g., at the development or production stage, or when data from a previous acquisition and appropriate well logs are available. It means that the approach is subsurface dependent.

The blue-filled step in Figure 4.1 corresponds to the forward process to generate blended data $\mathbf{P}'$ from $\mathbf{R}$ and $\mathbf{W}$ along with the current survey parameters, $\mathbf{D}$, $\mathbf{S}$ and $\mathbf{\Gamma}$. This

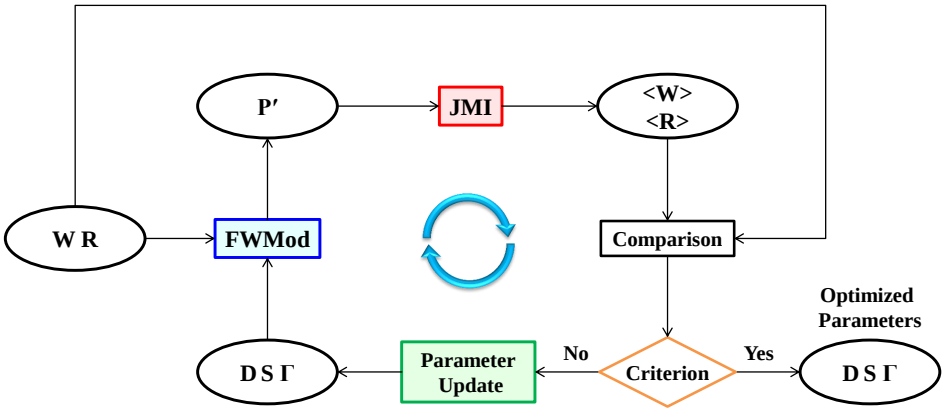

Figure 4.1: The survey design workflow. The iterative scheme aims to output the blending and sampling operators that provide the optimum deblending and reconstruction quality. The workflow starts with **R** and **W**. The forward process in the blue-filled step derives $\mathbf{P}'$ using FWMod. The inverse process in the red box then estimates $\langle\mathbf{R}\rangle$ and $\langle\mathbf{W}\rangle$ from $\mathbf{P}'$ using JMI. The procedure stops if the misfits between **R** and $\langle\mathbf{R}\rangle$ as well as between **W** and $\langle\mathbf{W}\rangle$ are sufficiently small or the maximum number of iterations is reached. If not, **D**, **S** and $\mathbf{\Gamma}$ are updated in the green box and subsequently used in the next iteration.

forward-modelling engine is called full-wavefield modelling (FWMod) [6]. In FWMod, reflection and transmission are assumed to take place at each depth level, described by the reflection operator **R**, whereas, in-between the depth levels, the wavefields propagate via the propagation operator **W**.

The red-filled step is the inverse process, i.e., JMI, to obtain $\langle\mathbf{R}\rangle$ and $\langle\mathbf{W}\rangle$ from $\mathbf{P}'$, where the angled brackets $\langle$ and $\rangle$ indicate estimation. JMI iteratively derives both reflectivity and velocity models using FWMod as its forward engine [3]. The implementation of FWMod and JMI in our study is based on [2, 7], which updates and estimates one single reflectivity parameter per grid point in **R** and one single slowness parameter per grid point in **W**. The detailed description of JMI is also available in Appendix B. It should be noted that proving the viability of the applied JMI algorithm is not the objective of this study. Our main focus is on exploring and understanding the effect of acquisition design on the performance of JMI.

Staal [7] suggested the JMI framework can be extended to blended acquisition. In this study, we formulate the objective function in JMI as:

$$J_{\mathrm{JMI}} = \sum_{\omega} \left\| \Delta\mathbf{P}' \right\|_2^2 = \sum_{\omega} \left\| \mathbf{P}' - \langle \mathbf{P}' \rangle \right\|_2^2. \tag{4.1}$$

Here, we feed $\mathbf{P}'$ directly into the JMI process. We perform JMI on the spatially regular and well-sampled detector grid determined by **X**. Each blended and irregularly-sampled shot record can be stored on this grid, yet the information is only present at active detector locations defined by **D**. Note that this choice means that our solution is spatially irregular in the sense that not all grid points contain detectors. However, all detectors coincide with grid points. By taking the grid size in **X** sufficiently small, the consequences

of this choice can be largely mitigated. Together with the current reflectivity and slowness estimates, FWMod simulates each blended shot record based on the given **S** and **Γ** at the regular, well-sampled detector grid. By selecting traces from the modelled shot records according to **D**, $\langle \mathbf{P}' \rangle$ can be obtained. This subsequently allows us to compute the residual between $\mathbf{P}'$ and $\langle \mathbf{P}' \rangle$ as described in Equation 4.1. The JMI procedure iteratively minimizes the data misfit via a gradient descent scheme. At each iteration, reflectivity and propagation operators are updated by cross-correlating wavefields, i.e., the back-propagated residual wavefield and the forward-modelled wavefield, in the opposite directions and in the same direction, respectively [8]. In our case, empty traces corresponding to detector locations that are not present in **D** are also used in the back-propagation in JMI along with the forward-propagation of the blended source wavefield determined by **S** and **Γ**.

The overall acquisition-design scheme attempts to minimize the residue between **R** and ⟨**R**⟩ as well as **W** and ⟨**W**⟩:

$$\vec{J} = \begin{bmatrix} J_{\mathrm{R}} \\ J_{\mathrm{W}} \end{bmatrix} = \begin{bmatrix} \sum_{\omega} \left\| \Delta \hat{\mathbf{R}} \right\|_2^2 \\ \sum_{\omega} \left\| \Delta \mathbf{W} \right\|_2^2 \end{bmatrix} = \begin{bmatrix} \sum_{\omega} \left\| \hat{\mathbf{R}} - \langle \hat{\mathbf{R}} \rangle \right\|_2^2 \\ \sum_{\omega} \left\| \mathbf{W} - \langle \mathbf{W} \rangle \right\|_2^2 \end{bmatrix}, \tag{4.2}$$

where $\vec{J}$ is the objective function vector containing errors in $\hat{\mathbf{R}}$ and **W**. The term $\hat{\mathbf{R}}$ represents a scalar reflectivity field converted to the space-time domain such that any undesired effects from errors in ⟨**W**⟩ on J_{R} are avoided.

The green-filled step in Figure 4.1 updates the blending and sampling operators that are subsequently carried into the next iteration. The procedure stops once the objective function is sufficiently small, or the maximum number of iterations is exceeded. Therefore, our approach iteratively computes the acquisition design parameters **D**, **S** and **Γ** that minimize the objective function vector, meaning that optimum reflectivity and velocity estimates can be obtained. Since FWMod is also used in the forward model engine of JMI, errors in the JMI results are attributable fundamentally to the choice of survey parameters.

To minimize the vectorized objective function in equation 4.2, we utilize non-dominated sorting and crowding distance approaches [9]. Algorithm 2 in Chapter 3 illustrates the procedure to assess the individual solution. To discriminate solutions with the same rank, we analyze their crowding distances. As mentioned previously, an infinite crowding distance is given to two solutions within the t^{th} rank having the maximum and the minimum value of a given objective function (in our case either J_{R} or J_{W}). Crowding distance values for other solutions in the g^{th} generation are then calculated by the sum of individual distance values corresponding to each objective function as:

$$d_{g,j} = \left| \frac{J_{\mathrm{R}}(\vec{C}_{g,j+1}) - J_{\mathrm{R}}(\vec{C}_{g,j-1})}{\max\limits_{j \in n_t} J_{\mathrm{R}\,g,j} - \min\limits_{j \in n_t} J_{\mathrm{R}\,g,j}} \right| + \left| \frac{J_{\mathrm{W}}(\vec{C}_{g,j+1}) - J_{\mathrm{W}}(\vec{C}_{g,j-1})}{\max\limits_{j \in n_t} J_{\mathrm{W}\,g,j} - \min\limits_{j \in n_t} J_{\mathrm{W}\,g,j}} \right|, \tag{4.3}$$

with

$$\forall\, j \in [2, \ldots, n_t - 1], \quad \vec{C}_{g,j} \in \vec{F}_t. \tag{4.4}$$

This ensures optimization of J_{R} and J_{W} along with the diversity of the new generation by assigning a higher priority to a more isolated solution in the objective function space.

4.3. NUMERICAL EXAMPLE

We numerically simulated four acquisition scenarios: one representing standard blended acquisition and the other three incorporating the DSA concept. Table 4.1 summarizes the spatial sampling schemes used in this study. In the standard scenario, detectors and sources are deployed regularly, while, in the other three scenarios, the geometries are irregular. Additionally, the three DSA scenarios employ fewer shot points than the standard one. Figure 4.2 and Table 4.2 compare the source properties of the standard and DSA scenarios. The standard scenario uses a spatially-uniform source signature with a wide frequency range. On the contrary, the DSA scenarios employ three source types, each having a dedicated narrow frequency bandwidth and a spatial sampling scheme according to its frequency range. This illustrates that the DSA scenarios emit significantly less energy in both space and frequency. Note that we applied dedicated low frequency sources, called DSA source type 1, whose frequency range, starting at 2 Hz, is not well covered by the source used in the standard scenario whose frequency range starts at 4 Hz (Figure 4.2 and Table 4.2). The DSA concept allows a lower-frequency source to be more coarsely sampled and a higher-frequency one to be more densely sampled. This effectively prevents both the oversampling of the lower frequencies and undersampling of the higher frequencies [4, 5]. Additonally, the sampling scheme can be adjusted to noise requirements in the particular frequency bands.

	Standard	DSA
Detector interval	40 m at regular	irregular
Number of detectors	50	50
Source interval	20 m at regular	irregular
Number of sources	100	70 (see Table 4.2)

Table 4.1: Detector and source sampling in standard and DSA scenarios.

	Frequency range (Hz)	Number of sources
Standard source	4-8-24-40	100
DSA source type 1	2-4-6-10	10
DSA source type 2	4-8-12-20	20
DSA source type 3	8-16-24-40	40

Table 4.2: Source properties in standard and DSA scenarios. Four corner frequencies: (1) low-cut, (2) low-pass, (3) high-pass and (4) high-cut, describe the frequency rage of each source type. As compared to the standard scenario, the DSA scenario employs fewer sources, each having a limited bandwidth.

Figure 4.3 shows a blended shot record from the standard scenario and one from a DSA scenario that exemplifies our blending and spatial sampling schemes. Unlike the standard scenario shown in Figure 4.3a, sources with different frequency responses are blended in the DSA scenario shown in Figure 4.3b. Our synthetic data contain both primary and multiple reflections. These data are directly fed into the JMI process to obtain

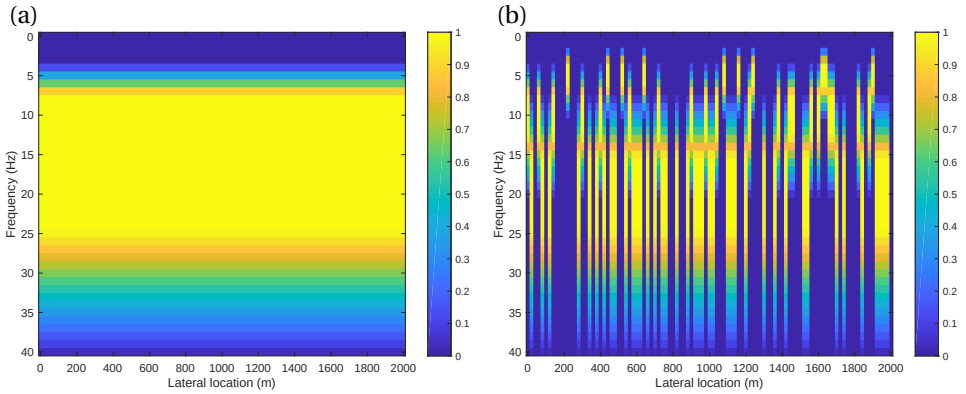

Figure 4.2: Source responses in the frequency-space domain. (a) Standard scenario using spatially uniform source signatures with a large bandwidth. (b) DSA scenario using three types of source units, each having specific spatial sampling and a dedicated small bandwidth.

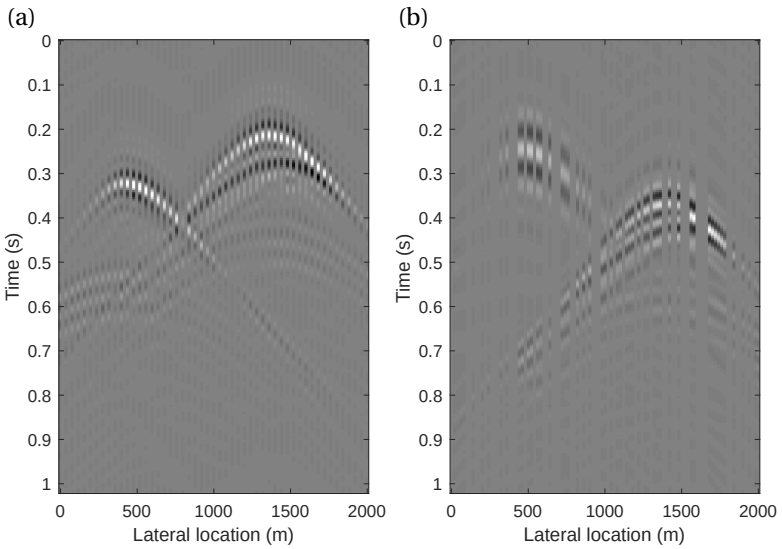

Figure 4.3: Blended shot record. (a) A blended shot record from the standard case where two sources employ the same signature with a regular detector interval. (b) A blended shot record from the DSA case where two sources employ different bandwidths and activation times with an irregular detector interval.

reflectivity and velocity estimates, i.e., without separation of overlapping shots and reconstruction of missing traces.

For comparison purposes, we provide three DSA scenarios, two of which are obtained from blending and sampling operators created by 800 realizations of uniformly-distributed, random variables. We derived the probability density function (PDF) by kernel density estimation using the 800 realizations. We show one result, called "P50",

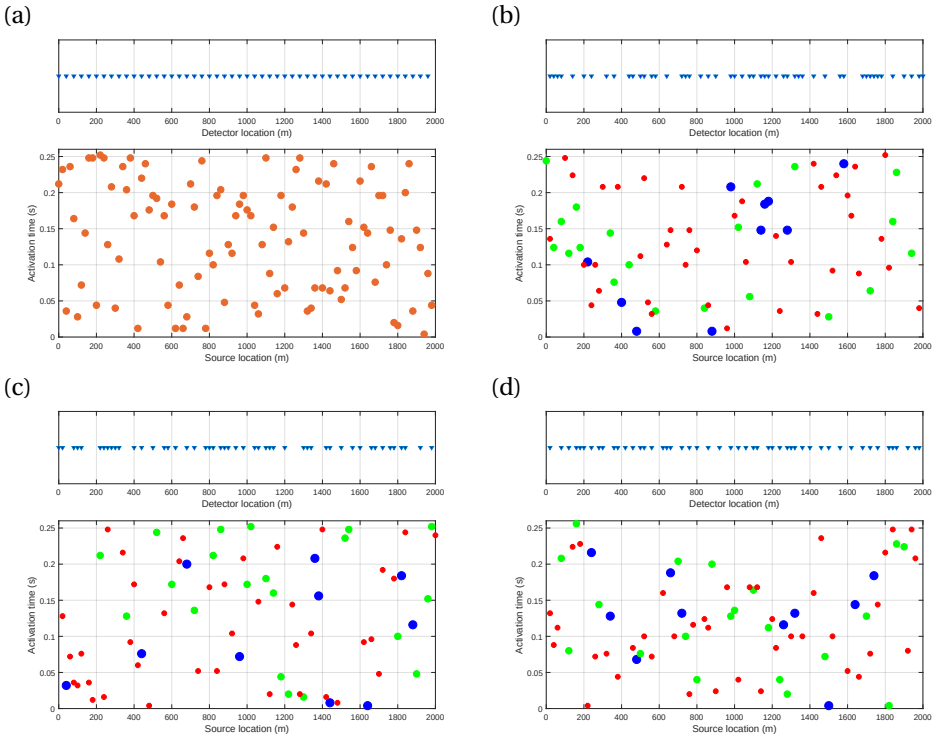

Figure 4.4: Acquisition scenarios used in this study: (a) Standard, (b) P50, (c) P1 and (d) optimized designs. Each figure contains two plots: spatial sampling of detectors (top) and that of sources as well as activation times (bottom). In the standard scenario, all sources employ the same signature with irregular activation times and with a regular detector interval. In three DSA scenarios, blue, green and red circle markers with different marker sizes correspond to DSA source type 1, 2 and 3, respectively. Activation times of these DSA sources are irregular with an irregular detector interval.

having the mode value in the estimated PDF, which we assume to be representative for the situation where we rely on a single random realization to embed irregularity into blending and sampling operators. In addition, we provide the best result, "P1", which is assumed to represent the outcome of a Monte Carlo approach. The three scenarios (standard, P50 and P1) are compared with the result from our optimized design derived from 800 realizations.

Figure 4.4 shows the acquisition configurations applied to the standard and three DSA scenarios, respectively. In our examples, the detectors and sources are placed at the surface ($z_d = z_s = 0$ m). The detectors are stationary, making the maximum offset in the data 2000 m. All scenarios use the same number of detectors, yet they are deployed differently. In each record of this study, two active sources are blended with a 1000 m distance separation, having different activation times ranging from 0 s to 0.256 s. In the DSA scenarios, three types of source units are irregularly distributed (see also Table 4.2).

Figures 4.5a-b show the true subsurface properties used in this study in terms of reflectivity and velocity, respectively. The model contains a lens-shaped high-velocity

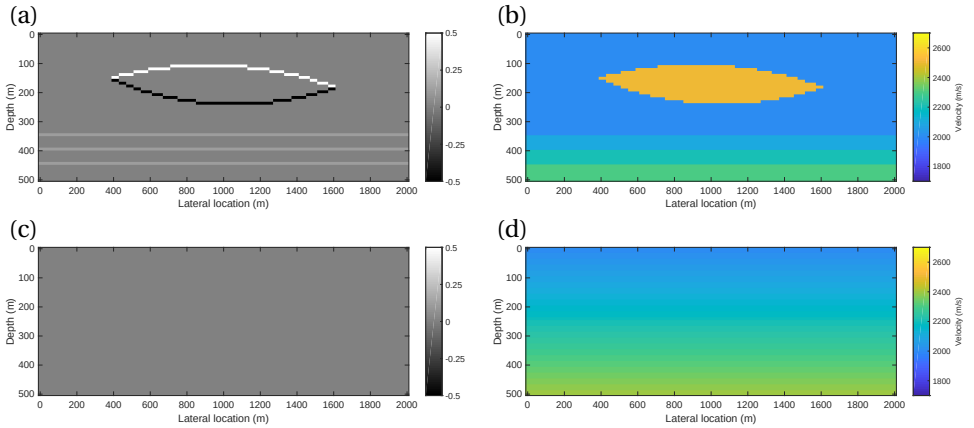

Figure 4.5: Subsurface model used in this study: (a) true reflectivity model, (b) true velocity model; (c) initial reflectivity model, and (d) initial velocity model.

body above three, weak horizontal reflectors. Figures 4.5c-d show the initial reflectivity model, which involves no contrast, and the initial velocity model, which contains a gradient only. The estimation by JMI starts with these models having (almost) no indication of true geological features.

Figures 4.6a-b show the JMI results from the standard acquisition design. Although some oblique lineaments are still recognizable below the lens body, both reflectivity and velocity models are estimated reasonably well. Figures 4.6c-d show the JMI results from P50. This scenario apparently accentuates linear artefacts, leading to some jitter on the three horizontal reflectors. The lateral velocity variation, particularly beneath the high-velocity lens, adversely affects the kinematics of wave propagation. This explains the undesired structural undulations on the three reflectors. As compared to P50, some improvements are observable in P1 (Figures 4.6e-f). However, it still is hard to find a justifiable rationale for the applied DSA scheme as compared to the standard one in terms of the JMI quality. The optimized design, however, attains notable enhancement in the JMI results (Figures 4.6g-h). The lens-shaped body can be easily delineated in both reflectivity and velocity estimates. Reduction of artefacts improves the coherency of the reflectors. The optimized design also achieves a robust estimation of the velocity model, which enables all the reflectors to be recovered close to their actual locations. Particularly, we can notice clear enhancement in flatness of three horizontal reflectors beneath the lens body. Even edge effects are well reduced in the optimized design as compared to the other three scenarios.

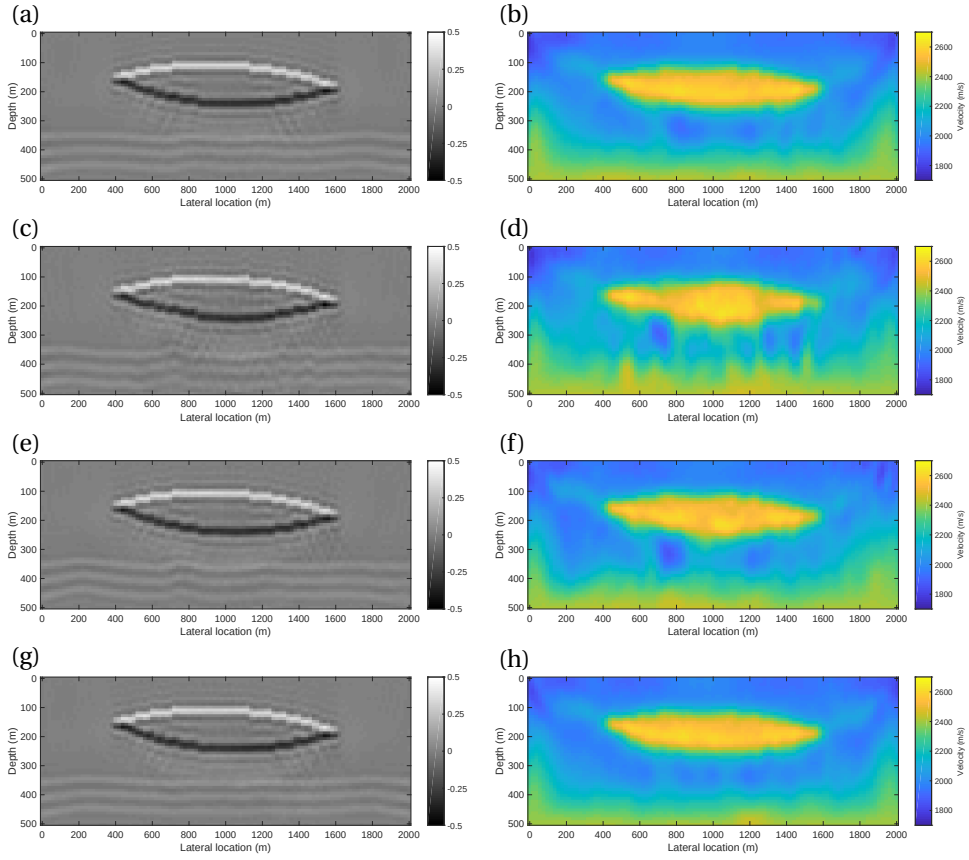

Figure 4.6: Estimated reflectivity and velocity models: (a)-(b) standard, (c)-(d) P50, (e)-(f) P1, and (g)-(h) optimized design, respectively. The notable enhancement in the performance of JMI due solely to the choice of survey parameters is easily recognizable.

In addition to the observations made from reflectivity and velocity estimates, Figure 4.7 quantitatively differentiates the overall data quality of each scenario. Figure 4.7a shows a cross plot of J_R against J_W from 800 random realizations. The colours of the circle markers indicate the number of the realization. The blue, green, red and cyan squares represent the standard, P50, P1 and optimized design, respectively. The three dashed lines in Figure 4.7a are constant probability density contours each of which represents the boundary of the area that contains a certain percentage (25%, 50% and 75% from the inner to the outer contour) of the estimated PDF. It shows a close to unimodal distribution indicating an increase in data points towards a single peak in the $J_R - J_W$ space. This implies that P50 obtained from the mode value in the PDF is expected to reasonably represent the anticipated data quality in the case where we use a single random realization to design blending and sampling operators. If it is assumed that the PDF based on the outcome of our Monte Carlo optimization procedure is correct, we observe that the cumulative probability of the objective-function values from our optimized design turns out to be smaller than 10^{-13}. Statistically, this suggests that an enormous number of random realizations are needed to reach a result that is equivalent to our optimized design. On the other hand, our workflow is capable of obtaining it with 800 realizations. Figure 4.7b shows a cross plot of J_R against J_W from our approach. This clearly demonstrates that the proposed workflow effectively and efficiently minimizes both J_R and J_W through the course of iterations. The optimized DSA acquisition scenario consequently leads to proper reflectivity and velocity estimates even when compared to the standard design, which employs more source effort.

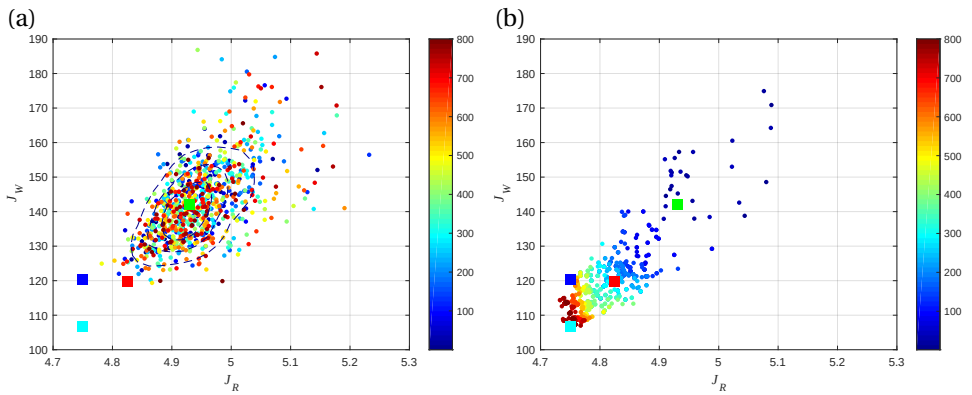

Figure 4.7: The progress of the optimization from (a) random realization and (b) proposed approach. Plot colours indicate the realization number. The blue, green, red and cyan squares are the results from the standard, P50, P1 and optimized design, respectively. In (a), the three dashed lines are constant probability density contours from kernel density estimation each of which represents the boundary of the area that contains a certain percentage of data points (25%, 50% and 75% from the inner to the outer contour).

As described previously, we performed a five-fold cross-validation at every 50 realizations to evaluate classification accuracies, while training the CNN (Figure 4.8). A vertical error bar indicates the minimum and the maximum accuracies obtained from each validation. Blue and red circle markers represent the mean value from five cross-validations

for training and testing, respectively. Although we adjusted the regularization strength applied on each weight in the network and the number of epochs to obtain a reliable model, due to the insufficient number of samples, the testing results still exhibit some indication of overfitting at the early stage of the iterative procedure. Since we altered the threshold criterion and some parameters within the CNN as mentioned previously, the validation results among different stages are not directly comparable. Nevertheless, the classification performance evidently improves through the course of iterations. Additionally, the difference in accuracies between training sets and testing sets becomes insignificant after a couple of hundred realizations, where the classification achieves accuracies well above 90% for both training and testing sets with a small discrepancy between the minimum and the maximum values. This indicates that our network architecture, along with the chosen hyperparameters, manages the bias-variance trade-off reasonably well and successfully relates the survey parameters to the resultant JMI quality.

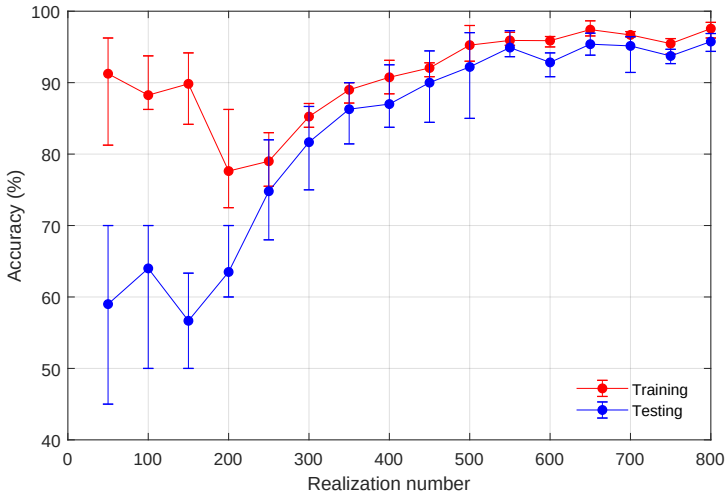

Figure 4.8: Classification accuracy of the predictive model at every 50 realizations. The red and blue markers represent mean accuracies at each five-fold cross-validation from training and testing sets, respectively. Error bars indicate the minimum and maximum accuracies obtained from each validation.

4.4. DISCUSSION

Insufficiencies in quality and quantity of available subsurface information potentially cause uncertainty in **R** and **W** used to optimize survey parameters in the proposed workflow although its degree varies with the situations. In this respect, we investigated the effect of this uncertainty on the JMI results. Figure 4.9a depicts velocity perturbations applied to the true model where we randomly modified the velocity of each layer with a value in the range of ±100 m/s. These velocity perturbations enable each subsurface

model to employ different **R** and **W**. For each arbitrarily derived subsurface model, we performed FWMod to simulate four different datasets $\mathbf{P}'$ using the four survey designs discussed earlier (standard, P50, P1 and optimized). We then applied JMI to these four datasets to obtain different reflectivity and velocity estimates. As shown in Figure 4.9b, this procedure was applied to the twelve subsurface models. Figure 4.10 shows a comparison among the JMI results from the four different acquisition scenarios for each subsurface model. The vertical axes of Figures 4.10a-b indicate relative differences in J_{R} and J_{W}, respectively, with respect to the corresponding objective function values from the optimized design. A negative value indicates that the optimized design attains the smaller misfit. The figure clearly shows that our optimized design achieves proper reflectivity and velocity estimates for all the models. Although certain variations can be observed among different subsurface models, the relative relationship among the four designs in terms of JMI quality still holds. For the reflectivity estimation, the standard and optimized designs attain comparable results. Next, P1 produces a somewhat less optimal outcome, followed by P50. For the velocity estimation, a distinct improvement can be seen in the optimized design. It clearly outperforms the standard design as well as the P1 design, the two of which provide almost comparable results. Then, the P50 result is suboptimal for all the subsurface models. Hence, this potentially indicates that blending and sampling operators derived from our approach can still provide optimum JMI results even when prior subsurface properties used for the survey design are not precisely known.

One of the unique properties of JMI is its ability to explain and utilize multiple reflections. They can provide subsurface illumination at different angles from the same shot and may carry information on areas that primaries cannot reach [10, 11]. Internal multiples are also capable of illuminating the subsurface in downward and upward directions [12]. By treating multiples as signal, they can also assist primaries in the subsurface illumination, provided that proper processing algorithms are implemented. For instance, Berkhout and Verschuur [13] illustrated a contribution of multiples by comparing JMI results with and without the use of multiples. Seismic surveys are often designed to sample primary reflections. On the contrary, less emphasis is given to multiples as they are usually to be attenuated in the subsequent processing. Exploiting features of multiples potentially allows us to ease the sampling requirements in data acquisition [11]. Alternatively, it can enhance the subsurface illumination with the same acquisition effort [14]. The proposed workflow, aimed at improving the JMI results, then enables us to derive acquisition scenarios that can account for the effect of both primary and multiple reflections in the area of interest.

In this study, we utilize the standard implementation of JMI based on [2, 7], which disregards certain subsurface characteristics. In this respect, some recent studies have been carried out towards exploring phenomena which are not explained in the standard framework such as mode conversion [3], angle-dependent reflectivity [15], horizontal wave propagation [16] and anisotropy [17]. The research has been also extended to other perspectives such as applications to 3D data [18], time-lapse data [19] and integration of JMI and full-waveform inversion (FWI) [20]. Furthermore, the presented numerical examples were designed fundamentally to demonstrate the proposed survey design scheme. To this end, a simple 2D subsurface model was chosen, which may not

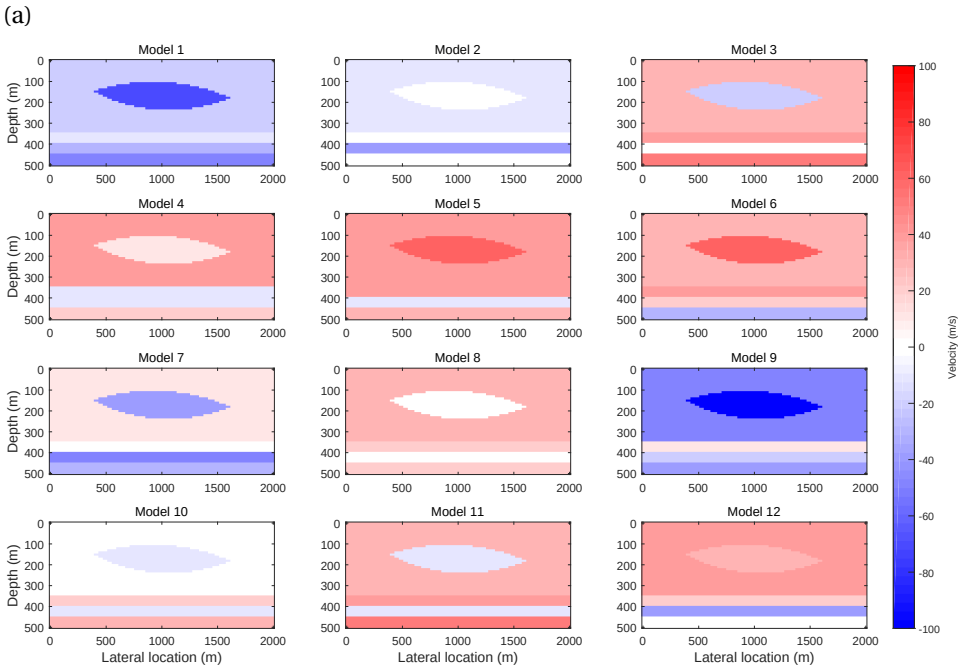

Figure 4.9: Analysis on the effect of uncertainty in prior subsurface information. (a) Various velocity perturbations applied to the subsurface model. (b) Procedure of the analysis for the i^{th} subsurface model. For subscripts in matrices, "Std", "P1", "P50" and "Opt" refer to the applied acquisition scenario.

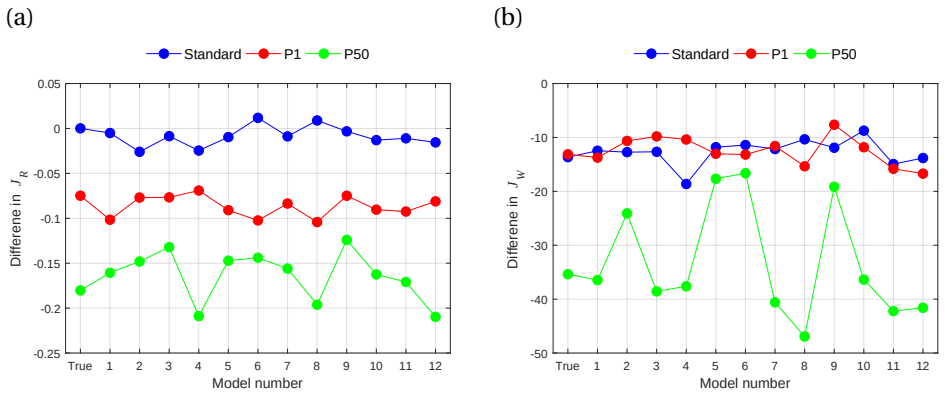

Figure 4.10: JMI results for different designs from different subsurface models: (a) reflectivity estimate and (b) velocity estimate. The plots in blue, red and green show relative differences between JMI results with respect to the optimized design for the standard, P1 and P50 design, respectively.

reflect the geological complexity encountered in actual fields. Hence, our future work is aligned with the recent developments in JMI, coupled with the use of more complex and realistic 3D subsurface scenarios.

This study demonstrates that optimally designed survey parameters lead to JMI results that are better than the results obtained with the standard scenario. Alternatively, the same results could have been obtained with the optimum survey in a more efficient and cost-effective manner. Furthermore, the implementation of DSA is of help in contributing to a health, safety and environment (HSE) perspective [5]. The emission of acoustic energy may incur a potential environmental risk, particularly in marine surveys. Sound pressure level (SPL) and sound exposure level (SEL) are of primary concern to determine the effects of an acoustic source on the marine environments, in particular on marine mammals [21]. Airgun clusters that generate an impulsive signal are widely used in the industry. As a broad frequency range of acoustic energy is instantaneously generated, the technique inevitably accentuates the peak pressure. Furthermore, these conventional marine sources inevitably emit high frequency components, e.g., well above 100 Hz, which are normally discarded in seismic imaging yet significantly overlap with the hearing ranges of odontocetes and pinnipeds [21]. The use of dedicated narrow-band sources decreases both the peak amplitude and the total energy for each shot. It is also capable of preventing a seismic survey from the emission of unnecessary frequency components, yet of acquiring the information needed to characterize the subsurface. Hence, the technique contributes to reducing both SPL and SEL. The optimized DSA scenario uses reduced source locations without adversely affecting the data quality. These elements lower the total energy accumulated over the survey duration, known as cumulative SEL. Reduced survey duration with the DSA concept also contributes to minimizing HSE risks in the field. In a certain number of shot locations, heavy and large devices, required for generating broad frequency range, can be replaced with light and compact devices, dedicated to generating the high-frequency range. This likely enhances the manoeuvrability of source units, which potentially allows

for safer operations. Our optimization scheme is, therefore, capable of designing an efficient, cost-effective and environmentally favourable seismic survey that also enhances the performance of JMI.

4.5. CONCLUSIONS

The survey design introduced in this study simultaneously optimizes parameters that determine the source blending and the spatial sampling of detectors and sources, which incorporate the DSA concept. The numerical examples in this study demonstrate that the JMI results can vary with the design of survey parameters. Optimally designed parameters lead to the enhancement of both reflectivity and velocity models estimated directly from blended and irregularly-sampled data. The proposed approach integrates a GA and a CNN to make the optimization of survey designs feasible within an affordable computation time. Genetic operators coupled with non-dominated sorting are capable of minimizing errors in reflectivity and velocity models by simultaneously updating the survey parameters. The workflow can effectively deal with complex blending and spatial sampling schemes that employ the DSA concept. The neural network architecture applied to this study successfully relates the performance of JMI to the choice of survey parameters. It helps us to minimize the computation of suboptimal designs while keeping the optimal ones into the iterative scheme. The proposed approach provides survey parameters to enhance the results of JMI that have been obtained by directly processing blended and irregularly-sampled data without the need for deblending or data reconstruction. The resultant acquisition scenarios allow us to optimally estimate subsurface properties at an affordable cost and with a low environmental footprint.

REFERENCES

[1] S. Nakayama, G. Blacquière, and T. Ishiyama, *Acquisition design for direct reflectivity and velocity estimation from blended and irregularly-sampled data,* Geophysical Prospecting **67**, 2127 (2019).

[2] X. R. Staal and D. J. Verschuur, *Joint migration inversion, imaging including all multiples with automatic velocity update,* 75th EAGE Annual Meeting, London, UK, Extended Abstracts **Tu 02 16** (2013).

[3] A. J. Berkhout, *Review Paper: An outlook on the future of seismic imaging, Part III: Joint Migration Inversion,* Geophysical Prospecting **62**, 950 (2014).

[4] A. J. Berkhout, *Blended acquisition with dispersed source arrays,* Geophysics **77**, A19 (2012).

[5] M. Caporal, G. Blacquière, and M. Davydenko, *Broadband imaging via direct inversion of blended dispersed source array data,* Geophysical Prospecting **66**, 942 (2018).

[6] A. J. Berkhout, *Review Paper: An outlook on the future of seismic imaging, Part I: Forward and reverse modelling,* Geophysical Prospecting **62**, 911 (2014).

[7] X. R. Staal, *Combined imaging and velocity estimation by Joint Migration Inversion* (Delft University of Technology, Ph.D Thesis, 2015).

[8] D. J. Verschuur, X. R. Staal, and A. J. Berkhout, *Joint migration inversion: Simultaneous determination of velocity fields and depth images using all orders of scattering,* The Leading Edge **35**, 1037 (2016).

[9] K. Deb, A. Pratap, S. Agarwal, and T. Meyarivan, *A fast and elitist multiobjective genetic algorithm: NSGA-II,* IEEE Transactions on Evolutionary Computation **6**, 182 (2002).

[10] A. J. Berkhout, *Combining full wavefield migration and full waveform inversion, a glance into the future of seismic imaging,* Geophysics **77**, S43 (2012).

[11] D. J. Verschuur and A. J. Berkhout, *From removing to using multiples in closed-loop imaging,* The Leading Edge **34**, 744 (2015).

[12] M. Davydenko and D. J. Verschuur, *Full wavefield migration, using internal multiples for undershooting,* 83rd SEG Annual Meeting, Houston, Texas, USA, Expanded Abstracts, 3741 (2013).

[13] A. J. Berkhout and D. J. Verschuur, *Enriched seismic imaging by using multiple scattering,* The Leading Edge **35**, 128 (2016).

[14] A. Kumar, G. Blacquière, M. W. P. Pedersen, and A. Goertz, *Full-wavefield marine survey design using all multiples,* Geophysics **81**, P1 (2016).

[15] S. Qu, Y. Sun, and D. J. Verschuur, *Mitigating amplitude versus ray-parameter effect in joint migration inversion using a zero-lag cross-correlation objective function of redatumed wavefields,* 88th SEG Annual Meeting, Anaheim, California, USA, Expanded Abstracts, 1133 (2018).

[16] S. Masaya and D. J. Verschuur, *Seismic modeling refracted and reflected waves including internal multiples by one-way propagators,* 87th SEG Annual Meeting, Houston, Texas, USA, Expanded Abstracts, 4138 (2017).

[17] A. A. Alshuhail and D. J. Verschuur, *Robust estimation of vertical symmetry axis models via joint migration inversion: Including multiples in anisotropic parameter estimation,* Geophysics **84**, C57 (2019).

[18] B. El-Marhfoul and D. J. Verschuur, *High-resolution, integrated 3D Joint Migration Inversion of Surface and VSP Data,* 86th SEG Annual Meeting, Dallas, Texas, USA, Expanded Abstracts, 672 (2016).

[19] S. Qu and D. J. Verschuur, *Simultaneous joint migration inversion for semi-continuous time-lapse seismic data,* 87th SEG Annual Meeting, Houston, Texas, USA, Expanded Abstracts, 5808 (2017).

[20] Y. Sun, Y. S. Kim, S. Qu, D. J. Verschuur, A. Almomin, and R. van Borselen, *Angle-dependent full wavefield migration based upon full waveform inversion and joint migration inversion,* 88th SEG Annual Meeting, Anaheim, California, USA, Expanded Abstracts, 4357 (2018).

[21] B. L. Southall, J. J. Finneran, C. Reichmuth, P. E. Nachtigall, D. R. Ketten, A. E. Bowles, W. T. Ellison, D. P. Nowacek, and P. L. Tyack, *Marine mammal noise exposure criteria: updated scientific recommendations for residual hearing effects,* Aquatic Mammals **45**, 125 (2019).

5

APPLICATION THROUGH THE FIELD LIFE

Acquisition of multiple seismic datasets at different moments in time, often called 4D or time-lapse seismic, is capable of satisfying the continuously increasing demand for high-quality subsurface images to reveal both static and dynamic elements during the field development. However, in practice, challenges of pursuing this strategy lie in different perspectives related to budgetary, operational and regulatory constraints. Seismic surveys, performed in a compressed manner in time and/or space, can provide high-quality seismic datasets in a cost-effective and productive manner. This way of acquisition normally accompanies decompression of recorded data such as deblending and/or data reconstruction. The performance of this recovery process is of fundamental importance in determining the technical success of compressed measurements. Our proposed approach aims at realizing the benefits from compression in data acquisition, contributing to cost, efficiency, health, safety and environment perspectives, while recovering deblended and reconstructed data of sufficient quality. The approach deals jointly with deblending and data reconstruction via a sparse inversion in the frequency-wavenumber domain, coupled with constraints on causality and coherency. Additionally, we formulate a single objective function aimed at sharing static information among vintages and, at the same time, at extracting dynamic changes in the reservoir of interest according to prior subsurface information. We apply the proposed approach to both synthetic and real data. A comparison with a strategy that independently recovers compressed datasets demonstrates the viability of the proposed simultaneous method to effectively enhance the quality of recovered data and extract reliable time-lapse signatures. We subsequently examine the effect of acquisition parameters on the recovery results. As compared to arbitrarily selected parameters, the iterative survey design proposed in this thesis derives compressed time-lapse measurements that enable each individual vintage to attain an enhanced subsurface image and time-lapse responses that are reasonably consistent with the dynamics in the field.

Parts of this chapter are available in references [1–3].

5.1. INTRODUCTION

It is well-recognized that seismic data are indispensable in hydrocarbon exploration. The information from seismic data also plays a vital role in various phases in the field development. Multiple seismic datasets are often acquired at different stages, from the exploration phase all the way to the improved oil recovery/ enhanced oil recovery (IOR/EOR) phase. The increasing demands towards high-quality seismic data during the field development profile leads to the need of considerable investment in data acquisition. Meanwhile, there is also a continuous requirement in cost reduction. The acquisition of data in a compressed manner in space and time, e.g., via the application of blended acquisition and/or sparse geometries, has drawn considerable attention as the approach is capable of enhancing operational efficiency as well as data quality [4–10]. Furthermore, the enhancement in the survey productivity contributes to minimizing health safety and environment (HSE) exposure in the field.

The outcome from subsequent decompression of recorded data, comprising of deblending and/or data reconstruction, is of primary importance in implementing this way of data acquisition. To realize its benefits throughout field development, this chapter introduces a method to recover compressed, time-lapse datasets. The proposed framework jointly applies deblending and data reconstruction to multiple time-lapse datasets in a simultaneous fashion. We formulate an iterative scheme to promote sparsity of solutions while minimizing data misfits. Additionally, it enables different vintages to communicate with each other to share static elements, which are considered to be time-invariant during the time-lapse measurements, and to extract production-related dynamic changes in the area of interest according to prior subsurface information. In addition to blending and irregular spatial sampling of both detectors and sources, the acquisition scenarios of our study incorporate the dispersed source array (DSA) concept [11, 12]. We also explore the effect of survey design on the performance of simultaneous data recovery. We utilize the iterative survey design to understand how the optimization of acquisition geometries can contribute to enhancing data recovery results in terms of image quality of each vintage as well as retrieval of time-lapse information. This section also discusses the potential benefits of compressed data acquisition along with subsequent simultaneous recovery, i.e., satisfying the increasingly demanding geophysical requirements during the field development while contributing to the business and HSE perspectives.

5.2. DATA RECOVERY FOR TIME-LAPSE DATASETS

The processes of separating blended data and reconstructing missing data share a certain resemblance. Both processes are often treated as inverse problems that involve iterative estimation of desired signals and subtraction of undesired ones, i.e., blending and aliasing noise, respectively, in the model space domain. Kutscha and Verschuur [13], for instance, imposed an L1 constraint in the Focal domain to handle the reconstruction problem. Kontakis and Verschuur [14] then extended this scheme to deblending. Additionally, Li *et al.* [15], Cheng and Sacchi [16], Cao *et al.* [17] jointly dealt with deblending and reconstruction. Oghenekohwo *et al.* [18], Wason *et al.* [19] presented synthetic studies that simultaneously recover time-lapse datasets acquired with compressed source

sampling. Our recovery algorithm essentially follows [2, 20] which utilized a sparse inversion in the frequency-wavenumber domain, coupled with constraints on causality and data coherency (see Appendix A for more details on the data recovery process). Similarly to the approach of [21], we introduce the following objective function of an inversion scheme for time-lapse datasets:

$$\begin{aligned} J &= \sum_{n=1}^{N} \sum_{\omega} \left\| \mathbf{P}'^{(n)} - \mathbf{D}^{(n)} \left\langle \mathbf{X}^{(n)} \right\rangle \mathbf{S}'^{(n)} \right\|_2^2 \\ &+ \sum_{n=1}^{N} \sum_{\omega} \lambda_1 \left\| \mathbf{L} \left\langle \mathbf{X}^{(n)} \right\rangle \right\|_1 \\ &+ \sum_{n=1}^{N} \sum_{t} \lambda_2 \left\| \Lambda^{(n)} \circ (\left\langle \hat{\mathbf{X}}^{(n)} \right\rangle - \left\langle \hat{\mathbf{X}}_{\mathrm{m}} \right\rangle) \right\|_2^2, \end{aligned} \tag{5.1}$$

where the first term corresponds to the associated least-squares minimization of data misfits for all the vintages ($n = 1, 2, ..., N$, with $n = 1$ indicating the baseline). Matrix $\mathbf{L}$ is the transform operator to the wavenumber domain where we perform deblending and data reconstruction. The second term promotes sparsity of the solutions in the transform domain. The third term poses an L2 constraint on time-lapse differences among all the surveys. This enables us to impose an anticipated production profile and subsequently to let all the vintages communicate with each other during the minimization process. Matrix Λ is a spatial weighting operator in the space-time domain derived from prior subsurface information, and $\circ$ denotes the Hadamard product. Matrix $\langle \hat{\mathbf{X}} \rangle$ indicates an estimate of the deblended and reconstructed data converted to the space-time domain. Matrix $\langle \hat{\mathbf{X}}_{\mathrm{m}} \rangle$ is a suitably chosen estimate that contains data related to static elements during the field production. Parameters λ_1 and λ_2 are weighting factors applied to the second and third term, respectively. In this study, we assume a proper version of Λ to be available by the time of processing of the second survey, which is often planned after the areal extent and thickness of hydrocarbon accumulations are reasonably well determined.

5.3. DATA RECOVERY RESULTS

5.3.1. SYNTHETIC DATA EXAMPLE

We numerically simulated time-lapse datasets acquired at five different acquisition times using full wavefield modelling [22]. Figure 5.1 shows the velocity and reflectivity models used to simulate the baseline survey, i.e., the 1$^{\mathrm{st}}$ vintage, in this study. Figure 5.2 then describes velocity and reflectivity perturbations applied to the subsequent four surveys. The model exhibits relatively simple anticline structures. While a good rule of thumb for seismic detection is that acoustic impedance changes between surveys should be larger than 4% [23], the applied scenario employs a slightly smaller response. Figure 5.3a shows unblended and well-sampled data, considered as the reference data. As shown in Figure 5.3b incoherent noise is added to the reference data. They are fed into the proposed recovery scheme. Figures 5.3c and d compare time-lapse responses from the 1$^{\mathrm{st}}$ vintage to the 5$^{\mathrm{th}}$ vintage without and with the noise. It is evident that the level of the applied noise is strong enough to mask the time-lapse signatures.

Our acquisition scenarios incorporate the DSA concept. Fig 5.4 shows blended and irregularly-sampled shot records from five vintages. Incoherent noise is added after we

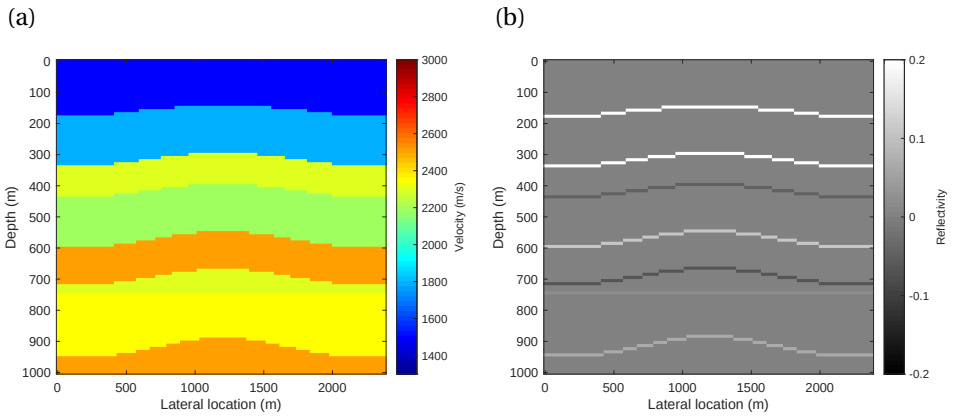

Figure 5.1: Velocity and reflectivity models at the time of the 1st survey.

5

generate blended and irregularly-sampled data from noise-free, unblended and well-sampled data. The DSA scenarios employ three source types, each having a dedicated narrow frequency bandwidth and a spatial sampling scheme according to its frequency range. The DSA concept allows a lower-frequency source to be more coarsely sampled and a higher-frequency one to be more densely sampled. This effectively prevents both the oversampling of the lower frequencies and undersampling of the higher frequencies[11, 12]. In our examples, detectors and sources are placed at the surface ($z_0 = 0$ m). The detectors are stationary, causing the maximum offset in the data to be 2400 m. All scenarios use the same number of detectors, yet they are deployed differently in an irregular and sparse fashion (Table 5.1). In each record of this study, two sources are blended having different activation times ranging from 0 s to 0.256 s. Three types of DSA source units (type 1: low-frequency, type 2: mid-frequency, type 3: high-frequency) are irregularly distributed according to the requirements defined in Table 5.1. We arbitrarily select these survey parameters using realizations from random variables according to a discrete uniform distribution in which no particular attention is involved in the replication of detector positioning or source positioning. We also enable different DSA source types to be deployed at the same location in different vintages. This means that source responses are not repeatable in our case.

Figure 5.5 shows the acquisition configurations applied to the five vintages. These survey parameters lead to a significant reduction in the size of $\mathbf{P}'$ with respect to the reference data. In this numerical example, we compress the size of the data matrix to roughly 12% of its original size. This number can be potentially translated to the amount of time, cost and HSE exposure that the applied acquisition strategy is able to minimize. In this study, we aim at retrieving a deblended, regularly and well-sampled, broadband dataset from the acquired blended, irregularly and sparsely sampled, DSA dataset.

Figure 5.6 shows deblended and reconstructed data as well as difference plots for the so-called independent approach. In this approach, each estimate is derived separately without communicating with each other. This means that N in Equation 5.1 is set at one for recovering each dataset. Note that a mute has been applied to remove all noise

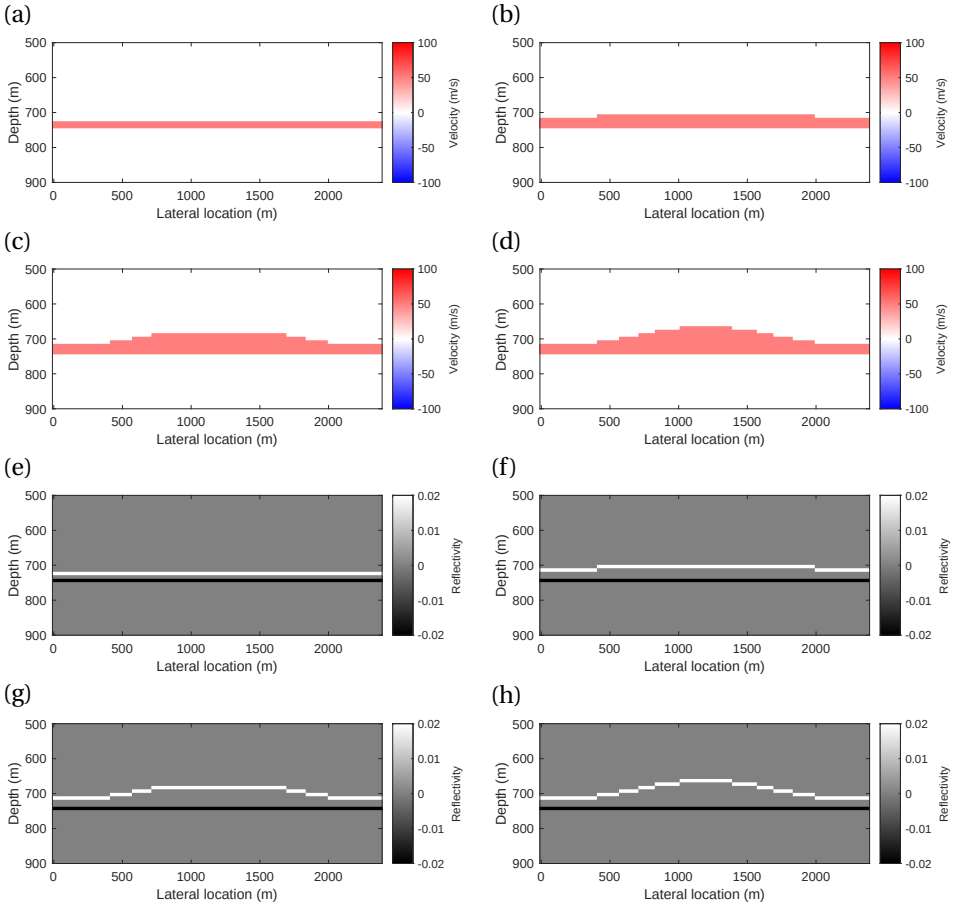

Figure 5.2: Time-lapse changes in subsurface properties throughout time-lapse measurements. (a)-(d) Velocity perturbations at the times of the 2nd to the 5th surveys with respect to the 1st survey. (e)-(f) Reflectivity perturbations at the times of the 2nd to the 5th surveys with respect to the 1st survey. The applied time-lapse scenario leads to slightly smaller than 4% acoustic impedance change.

	$\mathbf{X}$	$\mathbf{P}'$
Detector interval	20 m at regular	irregular
Number of detectors	120	60
Source interval	20 m at regular	irregular
Number of sources	120	56 (8-16-32)

Table 5.1: Detector and source sampling schemes applied to synthetic data examples for unblended and well-sampled data ($\mathbf{X}$) and blended and irregularly-sampled data ($\mathbf{P}'$). Three numbers within round brackets correspond, respectively, to the numbers of DSA source type 1 (low frequency), DSA source type 2 (mid frequency) and DSA source type 3 (high frequency).

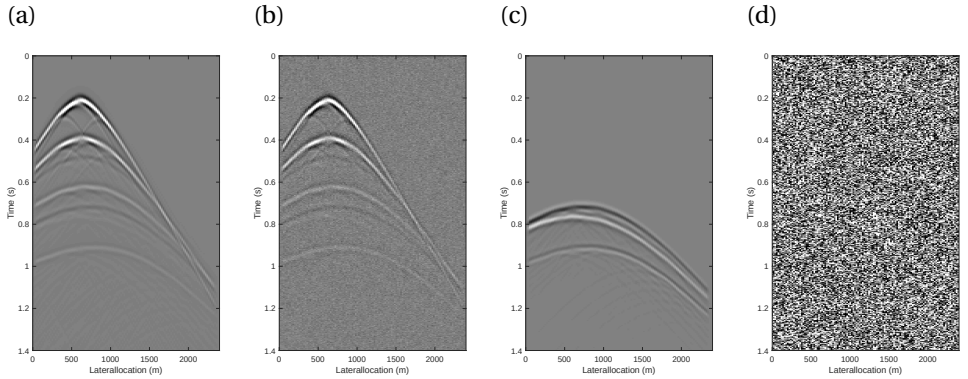

Figure 5.3: Unblended and well-sampled data. (a)-(b) Unblended and well-sampled shot records from the 1st survey without and with incoherent noise. (c)-(d) Time-lapse responses between the 1st and the 5th surveys without and with incoherent noise, both of which are amplified by a factor of ten.

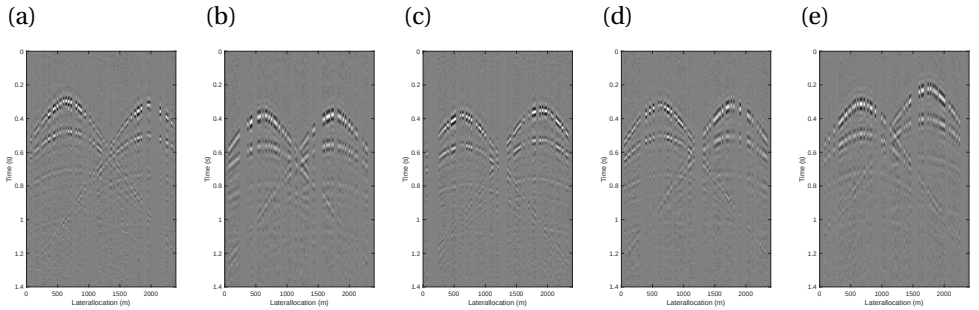

Figure 5.4: Blended and irregularly-sampled data. (a)-(e) Blended and irregularly-sampled shot records from the 1st through the 5th survey, respectively. Each vintage employs different blending and spatial sampling schemes.

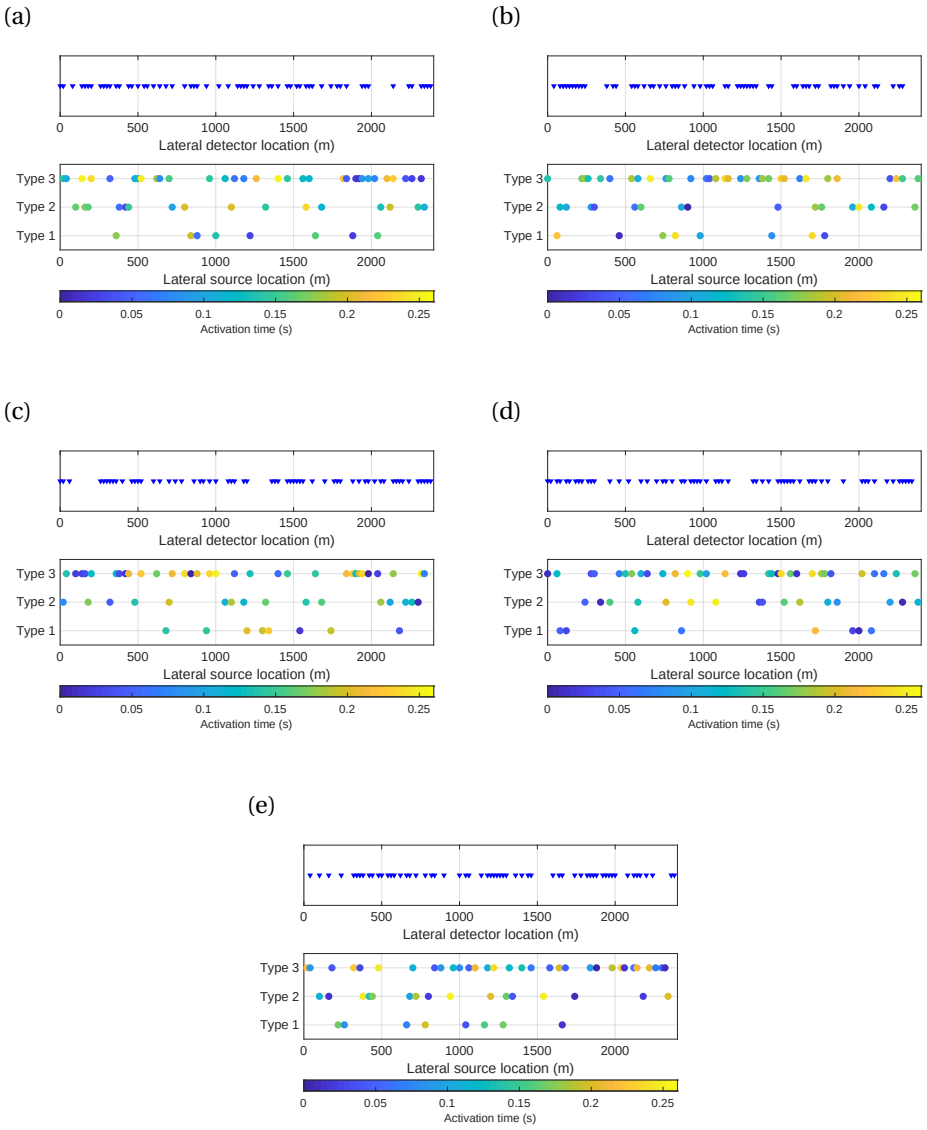

Figure 5.5: Acquisition scenarios applied to synthetic data examples. (a)-(e) Plots showing the spatial sampling of detectors (top) and that of three DSA source types as well as activation times (bottom) from the 1st through the 5th survey, respectively.

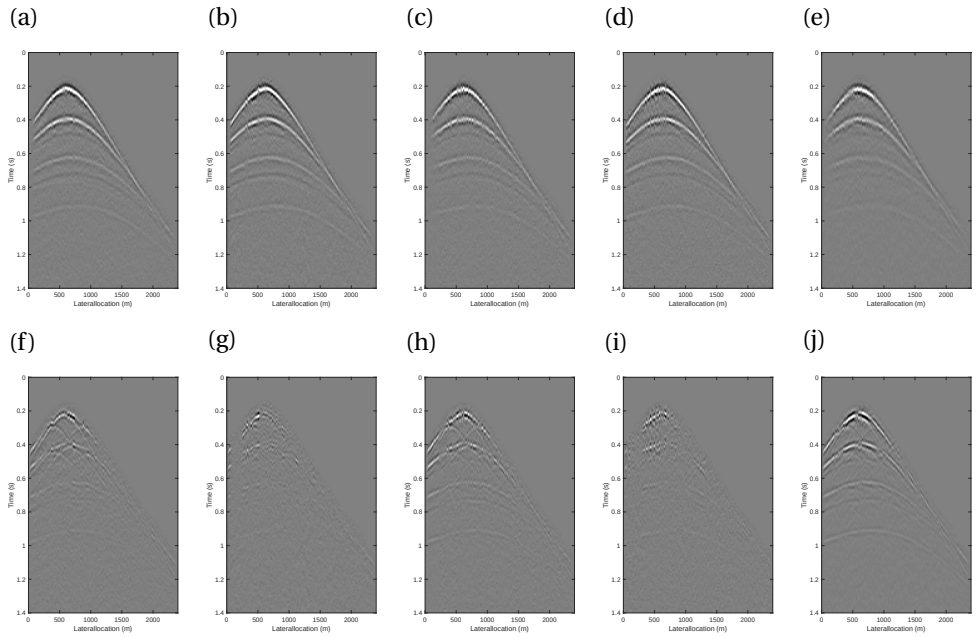

Figure 5.6: Deblended and reconstructed data (Independent approach). (a)-(e) Recovered shot records from the 1st through the 5th survey, respectively. (f)-(j) Difference plots (noise-free, unblended and well-sampled data minus recovered data) from the 1st through the 5th survey, respectively.

prior to the first arrival. Figure 5.7 shows the results obtained via the proposed scheme, called the simultaneous approach. They show discernible differences, attributed solely to the way the information from different vintages is utilized. The simultaneous approach clearly leads to improved data recovery for all vintages. Table 5.2 summarizes the signal-to-noise ratio (SNR) values from the different scenarios defined as:

$$\text{SNR} = 10\log_{10}\left(\frac{\sum_\omega \|\mathbf{X}\|_2^2}{\sum_\omega \|\mathbf{X} - \langle \mathbf{X} \rangle\|_2^2}\right). \tag{5.2}$$

Results from the first row of Table 5.2 represent the performance of the independent approach, allowing no information to be shared among vintages. The second to fifth rows correspond to the results from the proposed simultaneous approach, each using datasets available at the time of acquisition. For instance, the SNR values in the third row indicate deblending and reconstruction results using vintages 1, 2 and 3. We can clearly observe the enhancement of the SNR values as more time-lapse datasets are fed into the simultaneous recovery scheme.

Figure 5.8 shows two migrated sections of recovered data from the 1st survey, for the independent approach and the simultaneous approach, respectively. In both cases, we use the true velocity model for imaging. Despite a notable difference in the pre-stack quality, the two migrated sections are fairly comparable. This implies that the independent approach can still provide sufficient quality required in an early exploration phase

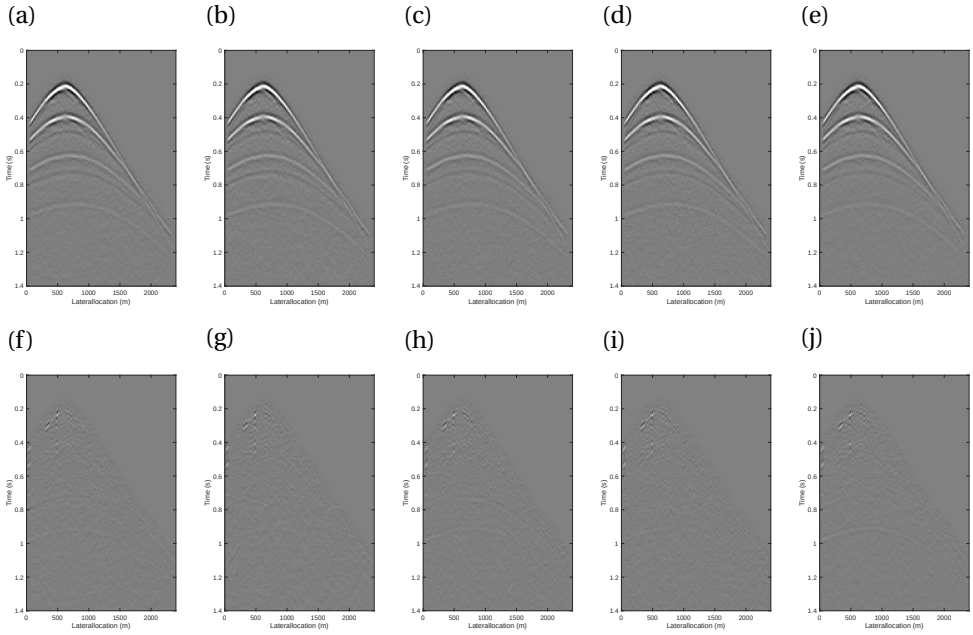

Figure 5.7: Deblended and reconstructed data (Simultaneous approach). (a)-(e) Recovered shot records from the 1st through the 5th survey, respectively. (f)-(j) Difference plots (noise-free, unblended and well-sampled data minus recovered data) from the 1st through the 5th survey, respectively.

	1st survey	2nd survey	3rd survey	4th survey	5th survey
Independent	6.64	7.26	6.50	6.78	6.72
Simultaneous (1st & 2nd)	9.75	9.75			
Simultaneous (1st to 3rd)	11.12	11.13	11.09		
Simultaneous (1st to 4th)	12.42	12.41	12.36	12.39	
Simultaneous (1st to 5th)	13.01	13.00	12.94	12.96	13.04

Table 5.2: SNR values from different scenarios in synthetic data examples. As compared to the independent scenario, the simultaneous scenarios achieve higher SNR values. Improvement in SNR values is recognizable in the simultaneous approach as more time-lapse datasets are fed into the recovery scheme.

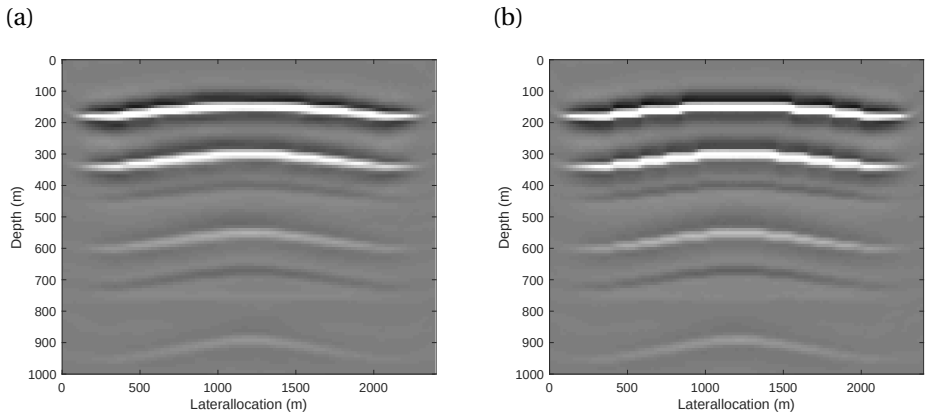

Figure 5.8: Migrated sections of recovered data from the 1st survey. (a) Independent approach and (b) Simultaneous approach.

such as interpretation of key geological events. Nevertheless, a close inspection of the migrated sections reveals some detailed differences between the two. With the use of a uniform grid spacing in subsurface models, dipping reflectors are inherently described as step-like ("staircase") interfaces. These are well imaged with the simultaneous approach. In the independent approach, these structural details are smeared, although the same migration parameters were applied in both cases. These deficiencies may adversely affect the subtle reservoir definition required at a later stage in the field development.

In Figures 5.9 and 5.10, the time-lapse responses between the two approaches are compared. In the independent approach, undesired events, some of which evidently have a stronger amplitude than the true time-lapse signatures, are clearly visible, likely due to errors in the data recovery. On the other hand, each vintage provides a time-lapse signal that is in good agreement with the true response at each time interval as shown in Figures 5.1 and 5.2. These examples also infer the value of time-lapse measurements at frequent intervals by detecting dynamic changes occurring over short time periods, which may contribute to development decisions in a timely fashion.

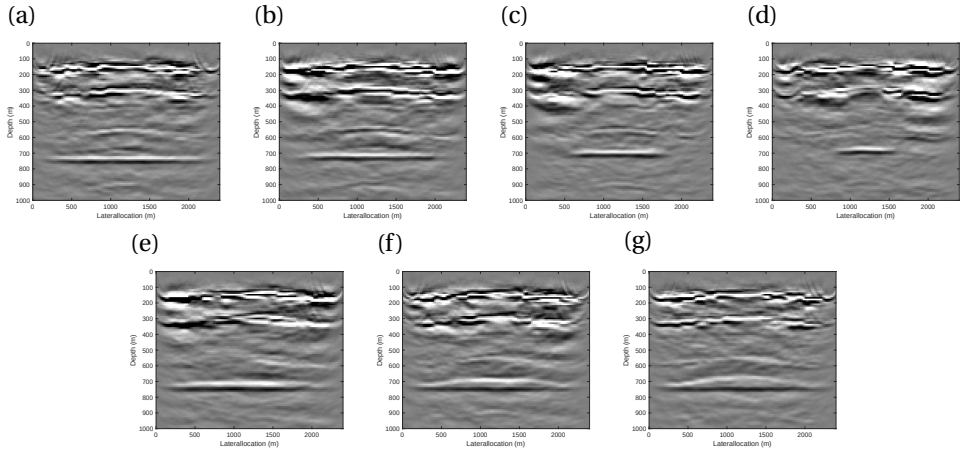

Figure 5.9: Differences in migrated sections from synthetic data examples (Independent approach). (a) 2^{nd}-1^{st} surveys; (b) 3^{rd}-2^{nd} surveys; (c) 4^{th}-3^{rd} surveys; (d) 5^{th}-4^{th} surveys; (e) 3^{rd}-1^{st} surveys; (f) 4^{th}-1^{st} surveys; (g) 5^{th}-1^{st} surveys.

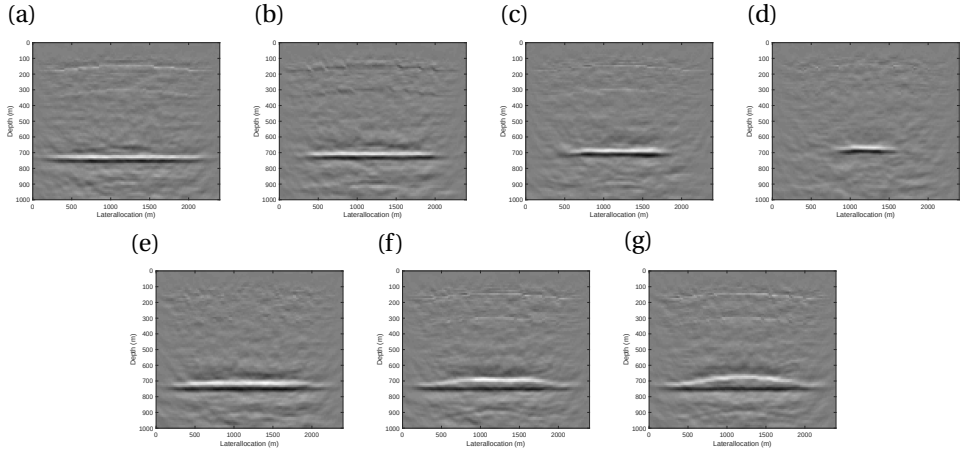

Figure 5.10: Differences in migrated sections from synthetic data examples (Simultaneous approach). (a) 2^{nd}-1^{st} surveys; (b) 3^{rd}-2^{nd} surveys; (c) 4^{th}-3^{rd} surveys; (d) 5^{th}-4^{th} surveys; (e) 3^{rd}-1^{st} surveys; (f) 4^{th}-1^{st} surveys; (g) 5^{th}-1^{st} surveys.

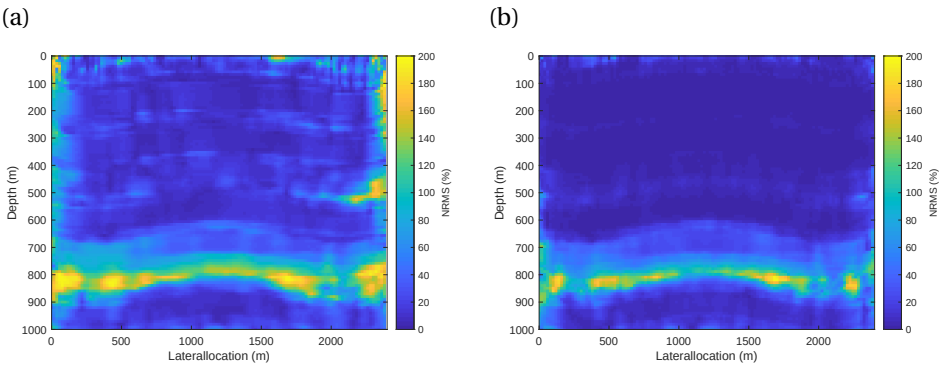

Figure 5.11: NRMS attributes of migrated sections from the 1st and the 5th surveys. (a) Independent approach and (b) Simultaneous approach. A depth window of ±30 m is used to compute NRMS values.

5

The normalized root mean square (NRMS) attribute [24] is used to quantify the likeness of traces from two vintages within a given window, $\vec{a}$ and $\vec{b}$, as:

$$\text{NRMS} = 200\frac{RMS(\vec{a}-\vec{b})}{RMS(\vec{a})+RMS(\vec{b})}. \tag{5.3}$$

Figure 5.11 shows NRMS values of migrated sections computed from the 1st survey and the 5th survey for the independent approach and the simultaneous approach, respectively. For the computation of NRMS at a given subsurface point, we apply a depth window of ±30 m (beginning 30 m above and ending 30 m below a point of interest). The NRMS attributes highlight the superiority of the proposed approach, leading to lower values of NRMS in the "static" overburden areas and a better stand-out of the time-lapse difference at the reservoir levels, while considerably large time-lapse errors in the "static" areas are clearly present in the independent approach.

5.3.2. FIELD DATA EXAMPLE

A subset of time-lapse datasets from 2D towed-streamer marine surveys acquired in the Troll field offshore Norway is selected. The baseline survey and monitor survey were performed in 1997 and 2002, respectively. Both datasets employ 25 m detector and source intervals. First, we applied some preprocessing such as near offset interpolation, surface-related multiple elimination and trace equalization. Additionally, we arranged the data into a fixed-spread geometry using source-detector reciprocity. The red box in Figure 5.12 depicts the subset of the field data used in this study in relation to the original data and the data obtained by applying reciprocity.

Figure 5.13 shows shot records from two vintages and their difference after preprocessing. They are considered as the reference data in this section. Although various events in the two vintages are easily correlatable, the difference plot in Figure 5.13c suggests the time-lapse signal is indiscernible in the pre-stack data. Using the reference data, we generate $\mathbf{P}'$ with the DSA concept consisting of three DSA source types (type 1: low-frequency, type 2: mid-frequency, type 3: high-frequency). As compared to the reference data, detectors and sources are decimated by 40% and 30%, respectively (Table 5.3). Additionally, with the DSA concept, each shot employs a dedicated narrow bandwidth instead of the wide bandwidth used in the reference data. In each shot record, two sources are blended along with a time delay in the interval from 0 s to 0.256 s. As compared to the reference data, the applied survey parameters compress the size of $\mathbf{P}'$ to 21% of its original size.

Figures 5.14 and 5.15 show blended and irregularly-sampled data of the baseline survey and the monitor survey along with the applied acquisition parameters. Detectors and sources are irregularly and sparsely distributed without paying any attention to the replication of geometry. Figure 5.16 shows deblending and data reconstruction results from the independent approach and the simultaneous approach, respectively. We

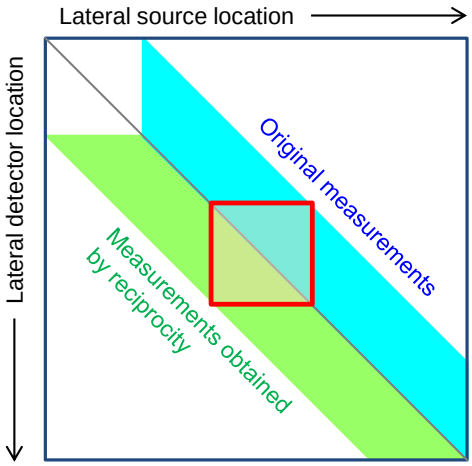

Figure 5.12: Schematic illustrating arrangement of field dataset. A red square represents a subset of data used in this study.

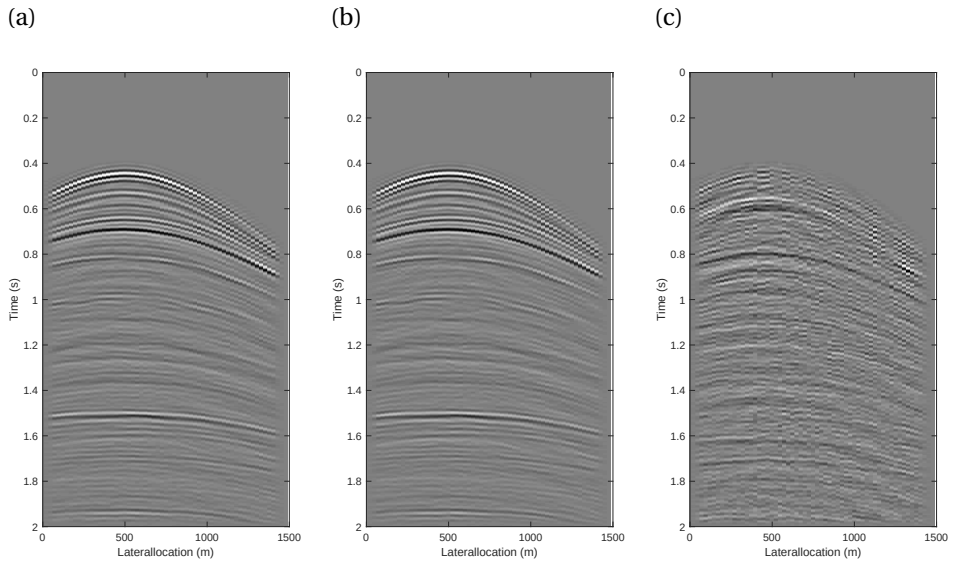

Figure 5.13: Unblended and well-sampled data. (a) Baseline survey; (b) Monitor survey and (c) Difference plot. Difference plot is amplified by a factor of five, showing an indiscernible response related to the field production.

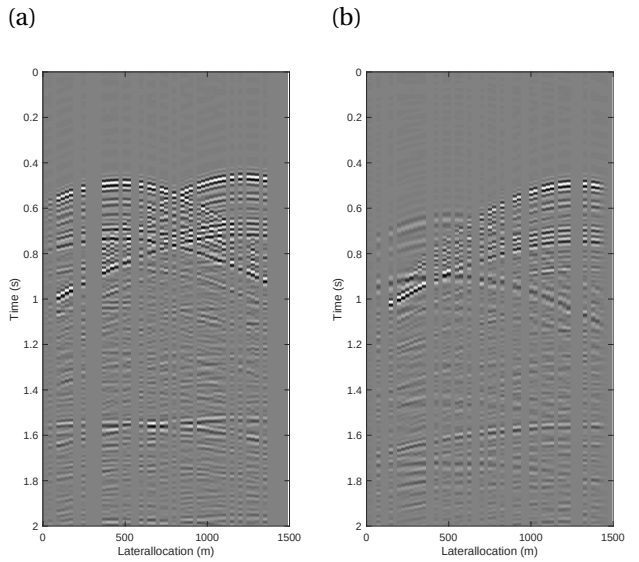

Figure 5.14: Blended and irregularly-sampled data. (a) Baseline survey and (b) Monitor survey. Two vintages employ different blending and spatial sampling schemes. With the DSA concept, different sources can employ different spectral properties.

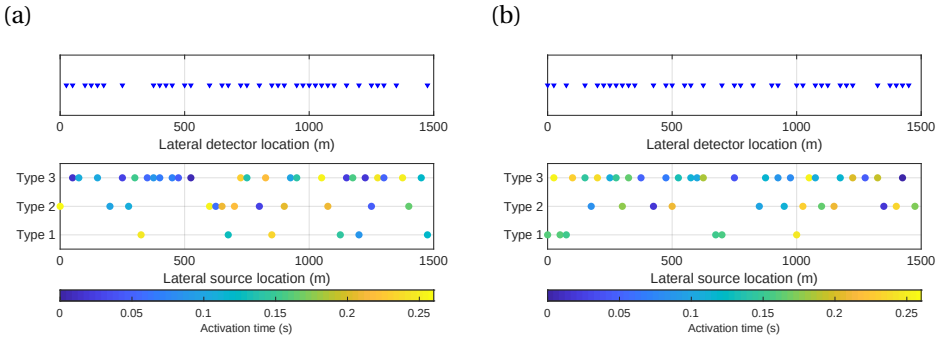

Figure 5.15: Acquisition scenarios applied to real data examples. (a)-(b) Plots showing spatial sampling of detectors (top) and that of three DSA source types as well as activation times (bottom) applied to baseline survey and monitor survey, respectively.

	$\mathbf{X}$	$\mathbf{P}'$
Detector interval	25 m at regular	irregular
Number of detectors	60	36
Source interval	25 m at regular	irregular
Number of sources	60	42 (6-12-24)

Table 5.3: Detector and source sampling schemes applied to real data example for unblended and well-sampled data ($\mathbf{X}$) and blended and irregularly-sampled data ($\mathbf{P}'$). Three numbers within round brackets correspond, respectively, to the numbers of DSA source type 1 (low frequency), DSA source type 2 (mid frequency) and DSA source type 3 (high frequency).

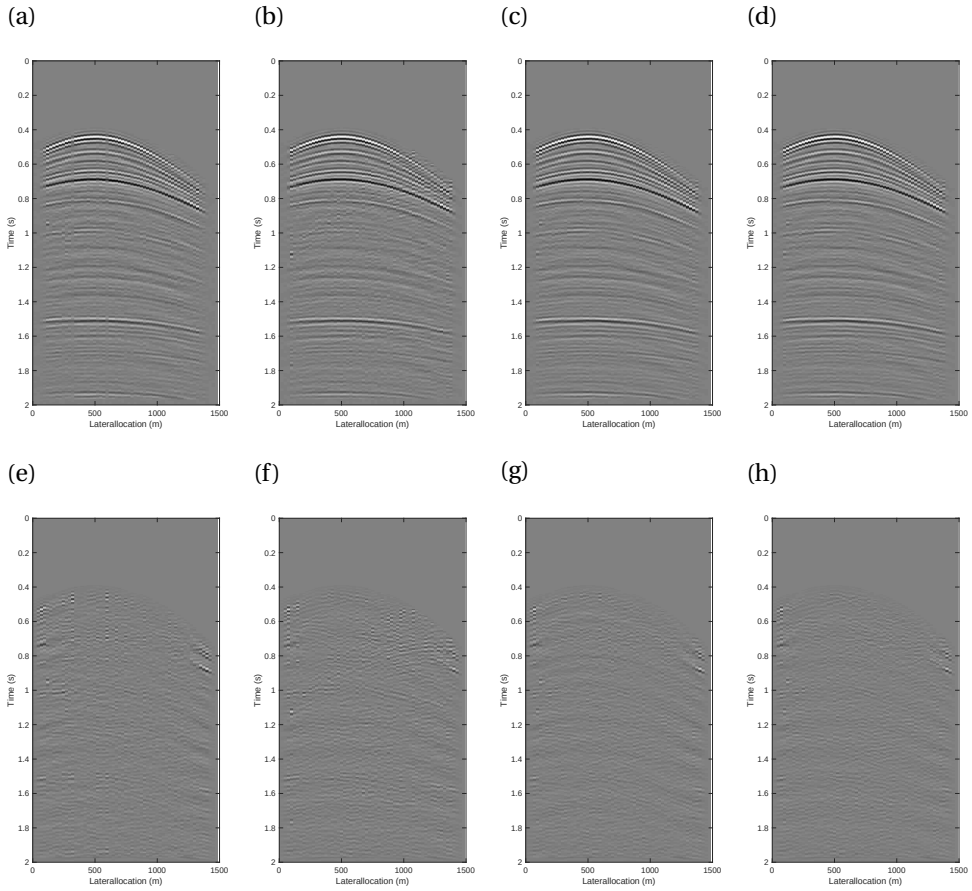

Figure 5.16: Deblended and reconstructed results. The first and second columns: baseline and monitor surveys from independent approach; the third and fourth columns: baseline and monitor surveys from the simultaneous approach. The top row shows deblended and reconstructed shot records. The bottom row shows difference plots from the reference datasets.

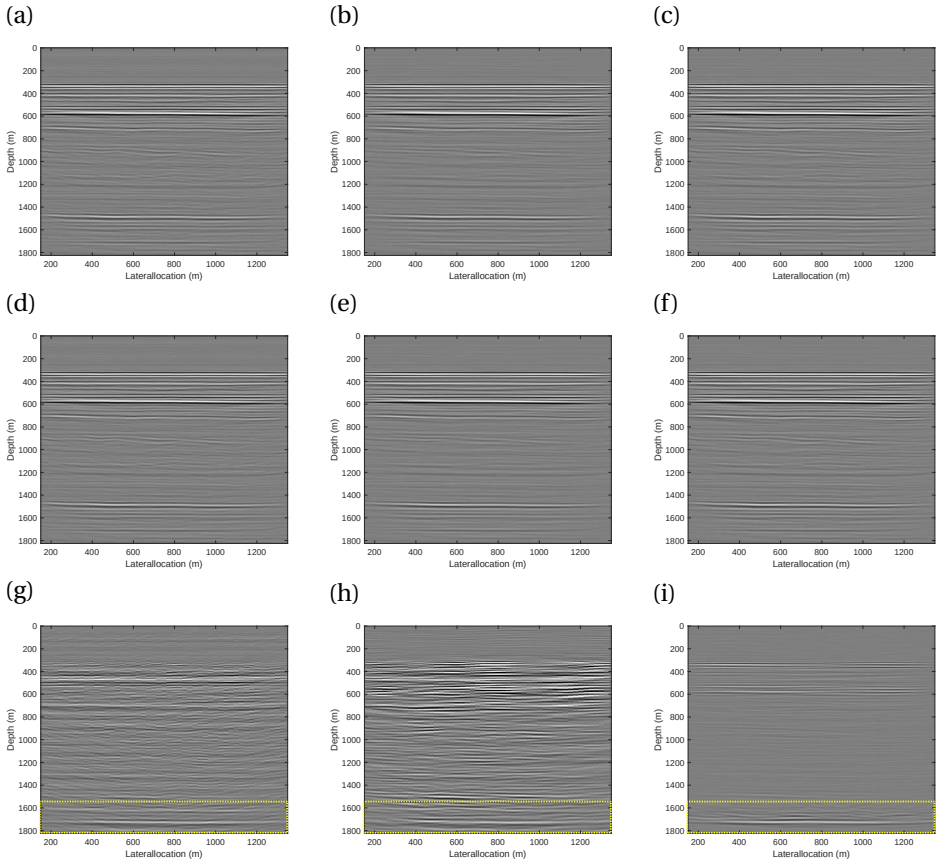

Figure 5.17: Migrated sections from real data examples. Three columns differentiate sections from reference data (left); independent approach (middle) and simultaneous approach (right). Three rows indicate sections from the baseline survey (top), the monitor survey (middle) and the time-lapse difference (bottom). Difference plots are amplified by a factor of ten. Yellow dashed rectangles in difference plots indicate the reservoir level.

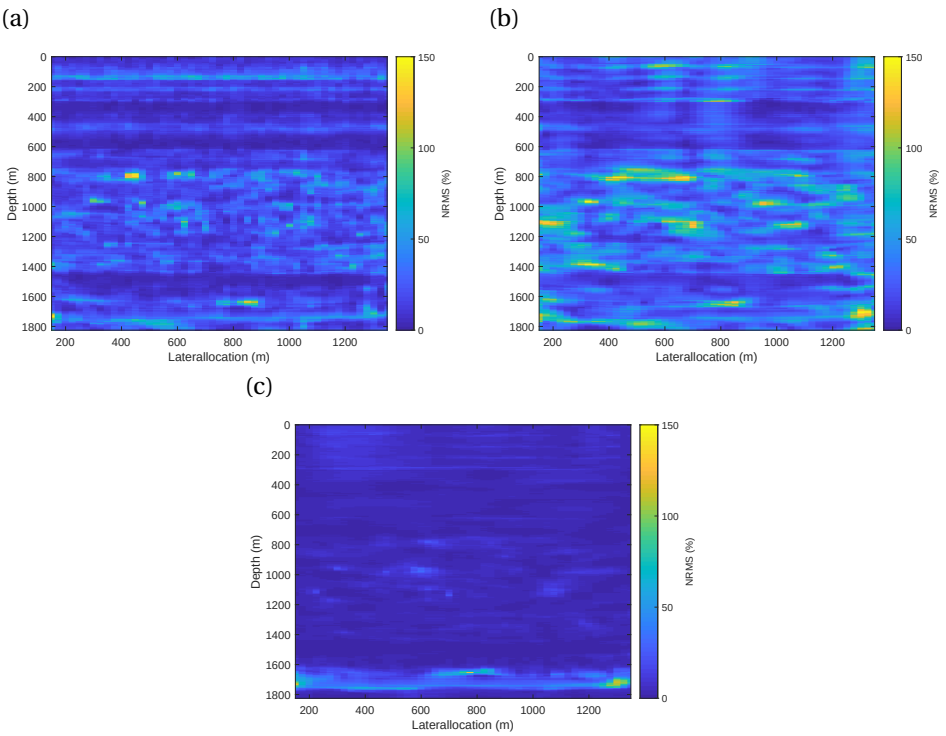

Figure 5.18: NRMS attributes derived from migrated sections: (a) Reference data; (b) Independent approach and (c) Simultaneous approach. A depth window of ±18.75 m is used to compute NRMS values.

	Baseline	Monitor
Independent	7.41	7.80
Simultaneous	10.95	10.89

Table 5.4: SNR values from independent and simultaneous approaches. As compared to the independent approach, the simultaneous approach achieves higher SNR values.

parametrized Λ according to [25] containing the information on the reservoir of interest. For both baseline and monitor surveys, some improvements are recognizable in the simultaneous approach as compared to the independent one. In the difference plots, some errors in deblending and reconstruction are still visible in the independent approach (Figures 5.16e and f). Aside from some edge effects, the events in Figures 5.16g and h consist mainly of low frequency and steeply dipping events which are presumably indicative of residual multiples. This suggests that the simultaneous approach recovers the desired signal reasonably well. Table 5.4 summarizes the SNR values that can quantify the performance of data recovery from the two approaches for two vintages. This supports the contribution of the simultaneous approach to the enhancement of data quality.

Figure 5.17 shows migrated sections where the three columns differentiate for reference (left), independent (middle) and simultaneous (right) scenarios, respectively, obtained from the same velocity model. The three rows then indicate sections from the baseline survey (top), the monitor survey (middle) and the time-lapse difference (bottom). Similar to the previously described synthetic examples, the migrated sections from the independent approach still attain a reasonable quality when compared to the other two cases. However, the time-lapse responses obtained from the three cases show clear differences. The reservoir level is located at a depth of roughly 1700 m, indicated by the yellow dashed rectangle in Figures 5.17g-i. In the reference data, relatively large differences are detectable in the area of the produced reservoir although other events at overburden levels irrelevant to the production activities are still observed. It is hard to discern a meaningful time-lapse signature in the independent approach. On the contrary, major time-lapse differences from the simultaneous approach are seemingly attributable to the production effect.

Figure 5.18 shows the NRMS attributes computed with a depth window of $\pm$18.75 m. It is obvious that the independent approach degrades the likeliness of traces from two vintages. On the other hand, a clear reduction of NRMS is easily recognizable in the simultaneous approach, indicating that the two recovered datasets are well correlated, even when compared with the reference datasets. Our inversion scheme preferentially recovers significant components in the frequency-wavenumber domain. This suppresses incoherent events to a certain extent. In addition, the method enables vintages to communicate with each other to share static information while preserving dynamic changes according to Λ. These factors contribute to lowering NRMS and providing appropriate datasets for time-lapse analysis.

	$\mathbf{P}'$
Detector interval	irregular
Number of detectors	36
Source interval	irregular
Number of sources	28 (4-8-16)

Table 5.5: Detector and source sampling schemes applied to real data example in section 5.4. Three numbers within round brackets correspond, respectively, to the numbers of DSA source type 1 (low frequency), DSA source type 2 (mid frequency) and DSA source type 3 (high frequency).

5.4. ACQUISITION DESIGN FOR TIME-LAPSE DATASETS

The previous section describes the capability of the proposed simultaneous approach to effectively recover compressed time-lapse datasets. In this section, we apply the same process to the field data using the different acquisition parameters described in Table 5.5. Most parameters including spectral properties of DSA source units are kept the same, except for the number of sources which is reduced by 33% as compared to $\mathbf{P}'$ shown in Table 5.3. We can easily anticipate that this acquisition scenario likely degrades the performance of data recovery if we do not pay any attention to the choice of survey parameters. In this section, we aim to mitigate deterioration of data quality by optimizing the blending and spatial sampling schemes.

In the case of conventional seismic surveys, several key parameters sufficiently describe how the data are acquired, e.g., detector and source intervals as well as detector and source apertures [26], and for time-lapse purposes, the exact repeatability among vintages needs to be cultivated. On the contrary, this is no longer the case with the application of compressed measurements, where irregularity is incorporated in the spatial sampling and/or blending schemes. This increases the number of survey parameters tremendously, making the parameter selection problem extremely complex, particularly when dealing with 3D acquisition geometries.

In this respect, we applied the proposed survey-design method (described in Chapter 2) to find optimum survey parameters, $\mathbf{D}$, $\mathbf{S}$ and $\mathbf{\Gamma}$, that enhance the quality of the recovered datasets and minimize the time-lapse errors between the two surveys from the Troll field. The workflow aims at a minimal data recovery error for each vintage as:

$$J_{\mathrm{X}} = \sum_{i=1}^{N} \sum_{\omega} \left\| \mathbf{X}^{(i)} - \left\langle \mathbf{X}^{(i)} \right\rangle \right\|_2^2. \tag{5.4}$$

where $\mathbf{X}^{(i)}$ and $\langle \mathbf{X}^{(i)} \rangle$ indicate unblended and well-sampled data, and recovered data for the i^{th} vintage, respectively. Furthermore, our scheme also intends to minimize the errors related to the time-lapse responses. For this purpose, we utilize the NRMS attribute to define the quality of the time-lapse effect:

$$J_{\mathrm{NRMS}} = \sum_{i,j} \mathrm{NRMS}^{(i,j)}, \tag{5.5}$$

with

$$i < j, \quad \forall\, i \in \{1, \ldots, N-1\}, \quad \forall\, j \in \{2, \ldots, N\}, \tag{5.6}$$

where $\text{NRMS}^{(i,j)}$ is the NRMS value computed from the i^{th} and the j^{th} vintages. Therefore, the overall scheme aims at minimizing the objective function vector containing information on J_{X} and J_{NRMS}:

$$\vec{J} = \begin{bmatrix} J_{\text{X}} \\ J_{\text{NRMS}} \end{bmatrix}. \tag{5.7}$$

To minimize the vectorized objective function in Equation 5.7, we utilize non-dominated sorting and crowding distance approaches [27] as illustrated in Algorithm 2 in Chapter 3. To discriminate solutions with the same rank, we analyze the crowding distance of each solution. As mentioned previously, an infinite crowding distance is given to two solutions within the t^{th} rank having the maximum and the minimum value of a given objective function (in this case either J_{X} or J_{NRMS}). Crowding distance values for other solutions in the g^{th} generation are then calculated by the sum of individual distance values corresponding to each objective function as:

$$d_{g,j} = \left| \frac{J_{\text{X}}(\vec{C}_{g,j+1}) - J_{\text{X}}(\vec{C}_{g,j-1})}{\max\limits_{j \in n_t} J_{\text{X}g,j} - \min\limits_{j \in n_t} J_{\text{X}g,j}} \right| + \left| \frac{J_{\text{NRMS}}(\vec{C}_{g,j+1}) - J_{\text{NRMS}}(\vec{C}_{g,j-1})}{\max\limits_{j \in n_t} J_{\text{NRMS}\,g,j} - \min\limits_{j \in n_t} J_{\text{NRMS}\,g,j}} \right|, \tag{5.8}$$

with

$$\forall\, j \in [2, \ldots, n_t - 1], \quad \vec{C}_{g,j} \in \vec{F}_t. \tag{5.9}$$

This ensures optimization of J_{X} and J_{NRMS} along with the diversity of the new generation by assigning a higher priority to a more isolated solution in the objective function space.

In addition to the result from our optimized design, we provide another acquisition scenario, called "P50", for comparison purpose. This is obtained from blending and sampling operators created by 800 realizations of uniformly-distributed, random variables. We derived the probability density function (PDF) by kernel density estimation using the 800 realizations. P50 employs the mode value in the estimated PDF, which we assume to be representative for the situation where we rely on a single random realization to embed irregularity into blending and sampling operators.

Figure 5.19 shows the acquisition parameters applied to the two scenarios. Figure 5.20 shows blended shot records from baseline and monitor surveys for the two scenarios. They use the same number of detectors and the same number of sources, yet they are deployed differently. In each record of this study, two active sources are blended with different activation times ranging from 0 s to 0.256 s. In the DSA scenarios, three types of source units are irregularly distributed according to the requirements defined in Table 5.5.

Figure 5.21 shows data recovery results from two acquisition scenarios. Although they use the same numbers of DSA sources and detectors as well as blending fold, certain differences, attributed fundamentally to the choice of survey parameters, can be observed, particularly in difference plots (Figure 5.21e-h). Results from P50 exhibit some crossing events indicating residual blending noise. Furthermore, several reflectors are not properly reconstructed. On the other hand, the optimized scenario attains clear improvement in data recovery for both vintages.

Table 5.6 summarizes SNR values obtained from the two acquisition scenarios. These values quantify the performance of the data recovery process for the entire volumes.

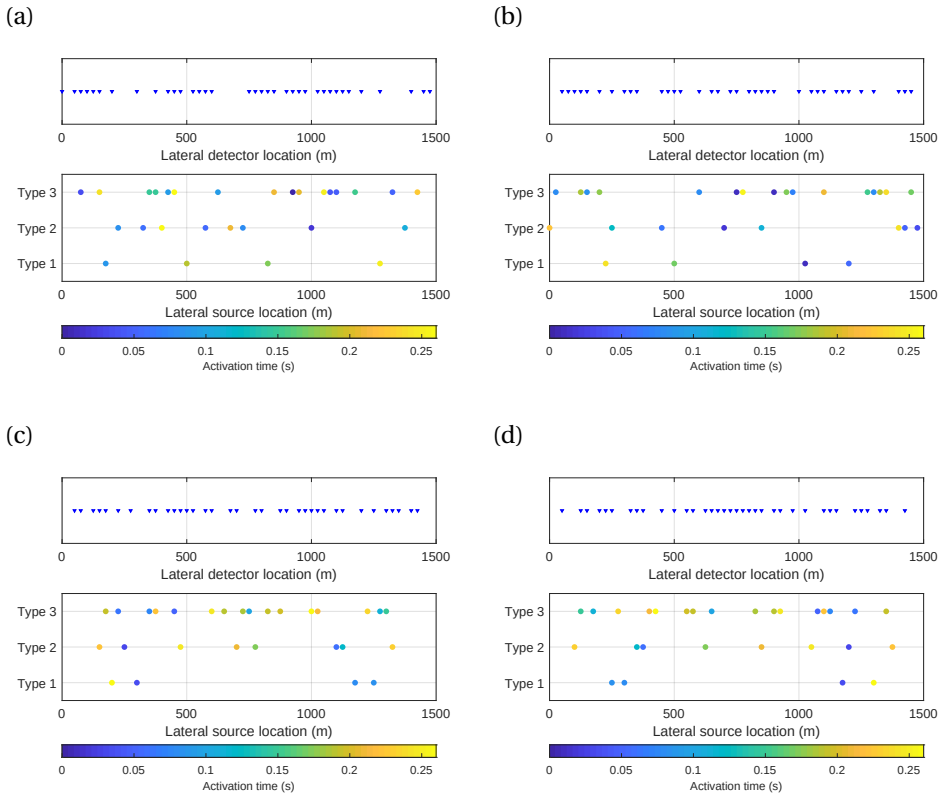

Figure 5.19: Comparison of acquisition scenarios. (a)-(b) P50 design for the baseline survey and the monitor survey. (c)-(d) Optimized design for the baseline survey and the monitor survey. Each sub-plot shows the spatial sampling of detectors (top) and the spatial sampling of three DSA source types as well as activation times (bottom).

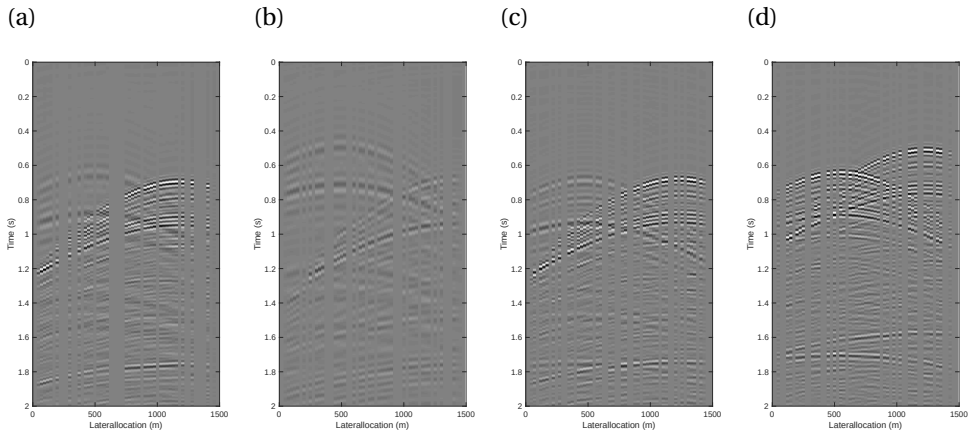

Figure 5.20: Blended and irregularly-sampled data. (a)-(b) Baseline survey and monitor survey (P50). (c)-(d) Baseline survey and monitor survey (Optimized). The two scenarios as well as the two vintages employ different blending and spatial sampling schemes.

	Baseline	Monitor
Independent (P50)	5.13	4.39
Simultaneous (P50)	7.51	7.47
Independent (optimized design)	7.11	7.19
Simultaneous (optimized design)	10.36	10.33

Table 5.6: SNR values for different acquisition scenarios and different recovery schemes. In addition to our recovery scheme, optimization of survey parameters contribute to enhancing SNR.

They show the enhancement of data quality via optimized survey parameters. The optimized scenario employs 33% fewer sources than the acquisition scenario shown in Table 5.3. Nevertheless, the resultant SNR values become fairly comparable. Additionally, Table 5.6 describes results from the independent approach for the P50 design and the optimized designs. The P50 result of the independent approach is considered to be representative for a situation where no proper attention is paid to the choice of survey parameters or the recovery algorithm. This case ends up with low SNR values for both baseline and monitor surveys (the first row of Table 5.6). On the contrary, a clear improvement is attainable with our optimized design and the simultaneous data recovery, yet without an increase in acquisition or processing effort. This indicates that proper acquisition and processing strategies are of importance in delivering the quality of subsurface images.

Figure 5.22 shows migrated sections where three columns differentiate for reference (left), P50 (middle) and optimized (right) scenarios, respectively, obtained from the same velocity model. Three rows then indicate sections from the baseline survey (top), the monitor survey (middle) and the time-lapse difference (bottom). The migrated sections are fairly comparable among the three scenarios (Figure 5.22a-f). As described in the previous section, the simultaneous data recovery surely contributes to preserving time-

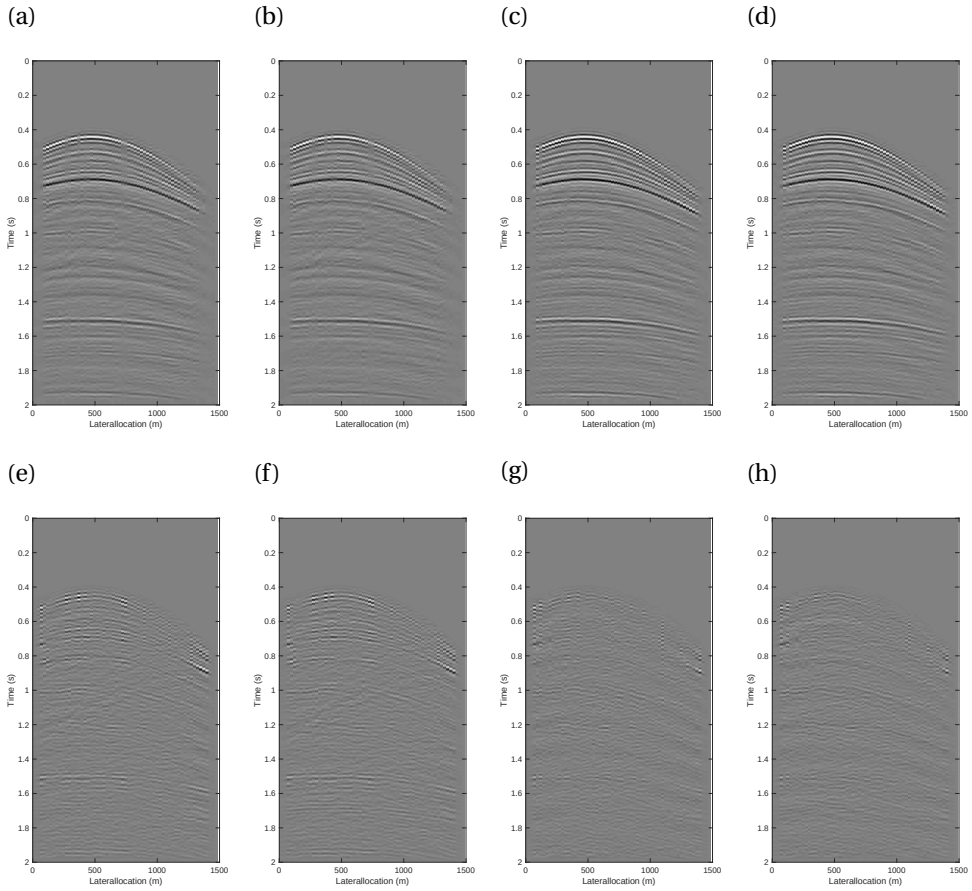

Figure 5.21: Deblended and reconstructed results. The first and second columns: baseline and monitor surveys from the P50 scenario; the third and fourth columns: baseline and monitor surveys from the optimized scenario. The top row shows deblended and reconstructed shot records. The bottom row shows difference plots from the reference datasets shown in Figure 5.13.

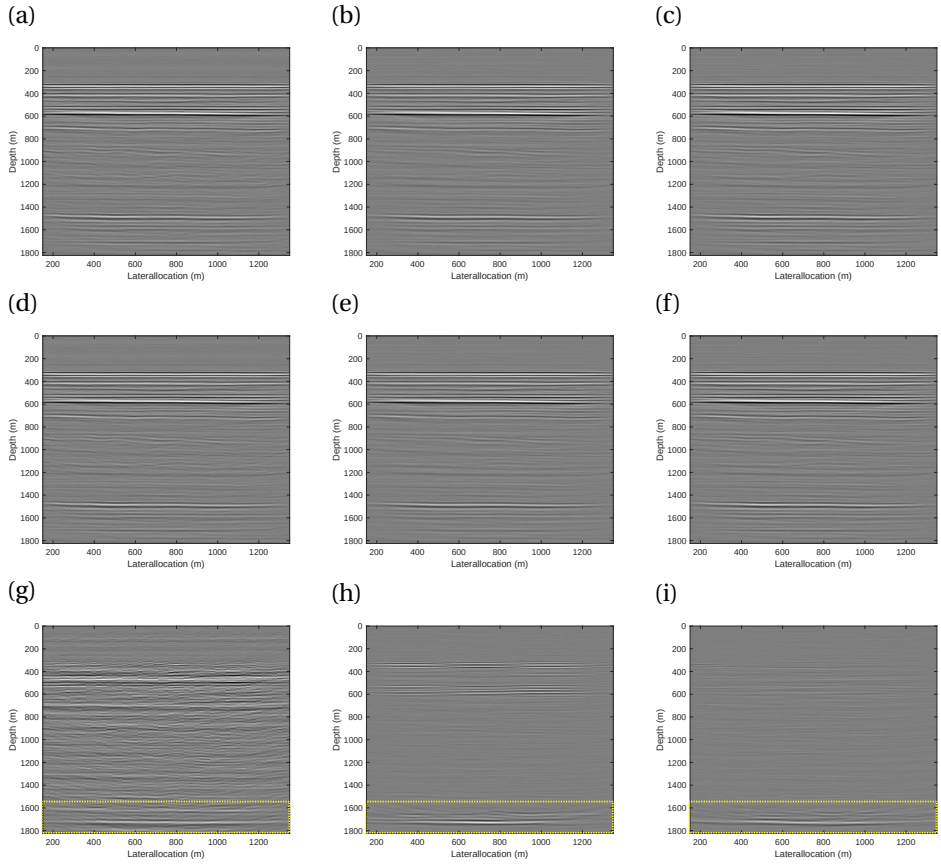

Figure 5.22: Migrated sections from real data examples. Three columns differentiate sections from reference data (left); P50 design (middle) and optimized design (right). Three rows indicate sections from the baseline survey (top), the monitor survey (middle) and the time-lapse difference (bottom). Difference plots are amplified by a factor of ten. Yellow dashed rectangles in difference plots indicate the reservoir level.

lapse signatures in the reservoir of interest (Figure 5.22g-i).

Figure 5.23 shows the NRMS attributes computed with a depth window of ±18.75 m. With the simultaneous data recovery, both the P50 design and the optimized design yield less time-lapse errors than the reference case although both datasets are acquired in a compressed and non-repeated manner. In addition, as compared to P50, our optimized design leads to a further reduction of NRMS values, particularly, at the overburden level, which is assumed to be static in our case. These results demonstrate that the proposed survey design, aimed at minimizing both J_X and J_{NRMS}, provides optimum time-lapse acquisition scenarios. The resultant survey parameters consequently deliver enhanced data quality for each vintage, along with time-lapse responses attributable to dynamic changes in the reservoir.

In addition to the aforementioned observations, Figure 5.24 quantitatively describes

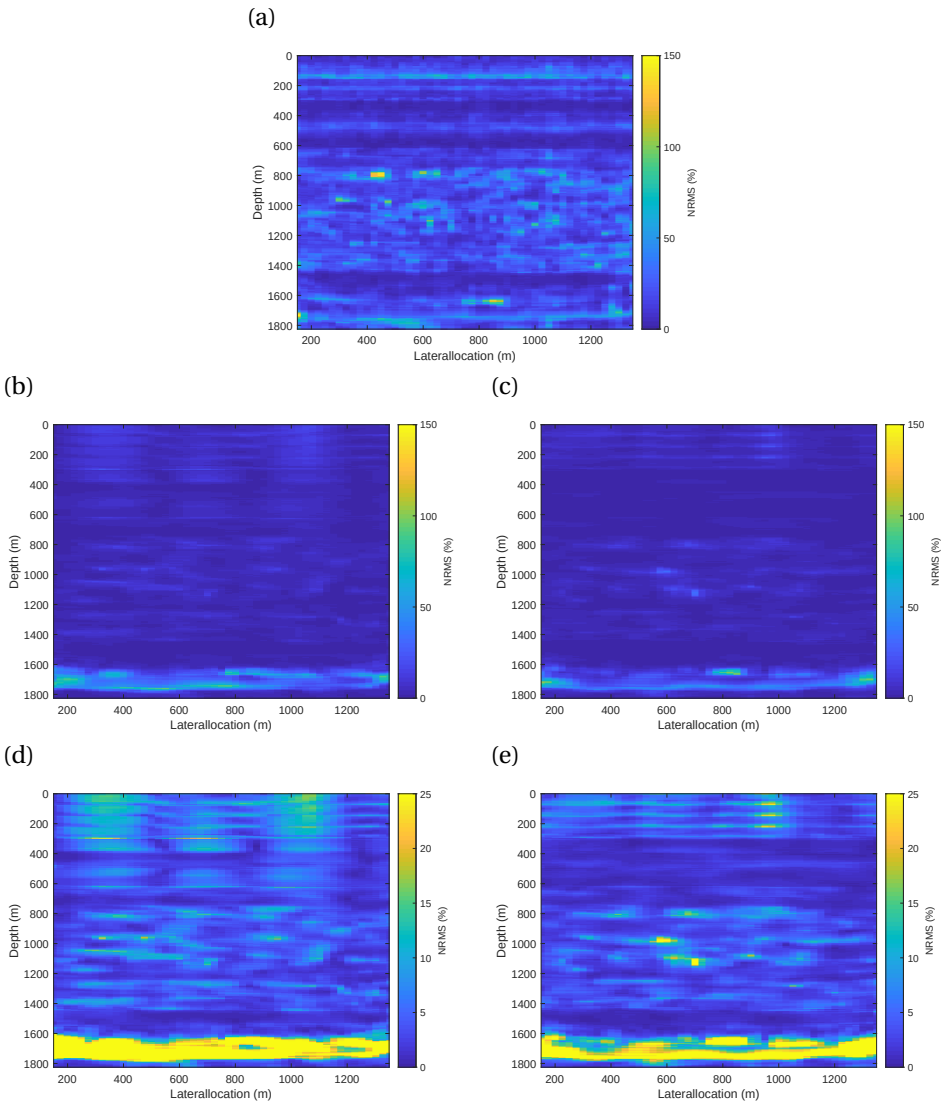

Figure 5.23: NRMS attributes derived from migrated sections: (a) Reference data; (b) P50 design and (c) Optimized design. Subplots (d) and (e) are the same as subplots (b) and (c), yet they are amplified by a factor of six. A depth window of ±18.75 m is used to compute NRMS values.

the overall data quality of each realization. Figure 5.24a shows a cross plot of J_X against J_{NRMS} from 800 random realizations. The colours of the circle markers indicate the number of the realization. The green and cyan squares correspond to the P50 design and optimized design, respectively. The three dashed lines in Figure 5.24a are constant probability density contours each of which represents the boundary of the area that contains a certain percentage (25%, 50% and 75% from the inner to the outer contour) of the estimated PDF. It shows a close to unimodal distribution indicating an increase in data points towards a single peak in the $J_X - J_{NRMS}$ space. This implies that the P50, obtained from the mode value in the PDF, indicates the anticipated data quality in the case where we use a single random realization to design blending and sampling schemes. If this PDF is assumed to represent the outcome of the Monte Carlo simulation, we observe that the cumulative probability of the objective-function values from our optimized design turns out to be smaller than 10^{-25}. Statistically, this suggests that a huge number of random realizations are required to reach a result that is equivalent to our optimized design. On the other hand, our workflow is capable of obtaining it with 800 realizations. Figure 5.24b shows a cross plot of J_X against J_{NRMS} from our approach. This clearly demonstrates that the proposed workflow effectively and efficiently minimizes both J_X and J_{NRMS} through the course of iterations.

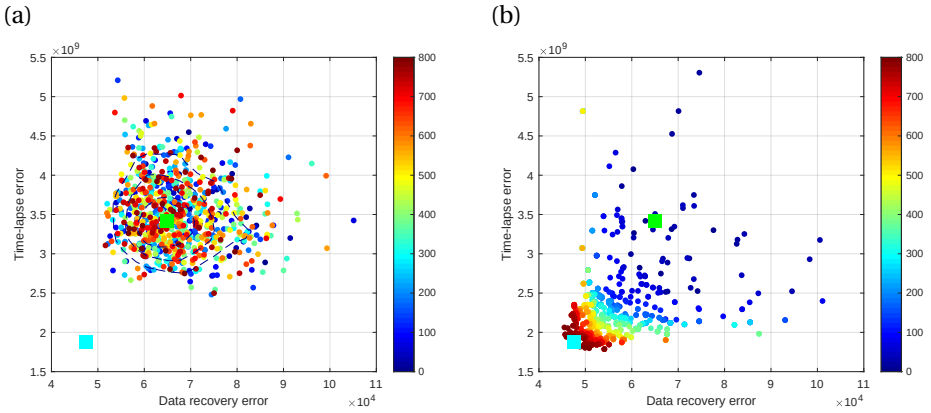

Figure 5.24: The progress of the optimization from (a) random realization and (b) proposed approach. Plot colours indicate the realization number. The green and cyan squares are the results from the P50 and optimized design, respectively. In (a), the three dashed lines are constant probability density contours from kernel density estimation each of which represents the boundary of the area that contains a certain percentage of data points (25%, 50% and 75% from the inner to the outer contour).

5.5. DISCUSSION

As conceptualized in Figure 5.25 and described previously, there is an increasing demand for high-quality seismic images throughout the field development profile. In general, a single seismic survey is insufficient to fulfil the various objectives arisen at different stages during the field life. Hence, multiple surveys are generally acquired to be fit for different purposes and different needs varying from one development phase to another. To

overcome deficiencies in an existing vintage by a newly planned survey, a viable solution is to enhance the specifications, e.g., in terms of temporal and spatial sampling. Despite the added value to the subsurface description, this leads to a considerable investment at every survey. To accurately monitor dynamic changes in the reservoir, it is considered desirable to acquire a high-spec baseline survey and to precisely repeat it at frequent intervals. However, in practice, there may be various factors that make this approach difficult to realize. Particularly, budgetary constraints can easily force compromises on survey parameters. The exact replication of an acquisition geometry is normally considered as a primary concern in time-lapse measurements, yet it becomes even more challenging in mature fields due to an increase in surface installations during the field development. Despite extra efforts incurred in both acquisition and processing, insufficiency in the recorded data may not be resolved, e.g., around a large obstruction such as a production platform. As a conventional seismic survey often aims primarily at attaining preset fold coverages of certain offset classes, an existing vintage might not necessarily have been acquired as a suitable baseline for future time-lapse measurements. The proposed scheme potentially contributes to dealing with the aforementioned challenges. The simultaneous data recovery utilizes all the vintages to share static information among them while preserving dynamic changes in each individual dataset. This consequently provides an increasing data quality along with increasingly reliable time-lapse signatures as more datasets are fed into the inversion scheme. Since compressed measurements successively contribute to the data recovery process, higher data quality can be supplied in the later stage of the field development without increasing an acquisition effort. Efficient and cost-effective surveys, acquired in a blended and irregularly-sampled manner, would be able to continuously satisfy the technical requirements from the exploration phase until the IOR/EOR phase. Repeatability in seismic acquisition becomes insignificant, which offers flexibility in field operations and more opportunities of time-lapse measurements for the areas having difficulty in replicating the positions of detectors and sources. The cost-effectiveness of the compressed measurements certainly makes data acquisition at frequent and proper intervals justifiable. Furthermore, the enhancement of the survey efficiency contributes to minimizing the HSE exposure in the field. In a marine environment, the DSA concept is also of help in reducing the level of acoustic emission exposed to the environment, as compared to a conventional source comprising of a cluster of airguns [12].

In the proposed simultaneous approach, we disregarded some aspects which possibly provide future directions for our research. For example, this study does not explicitly deal with the situation of significant time-lapse variations in the overburden, e.g., due to dynamic changes in the sea state, near-surface conditions and/or geomechanical effects. These overburden effects may potentially lead to amplitude fluctuations and travel time shifts, and subsequently bias the time-lapse analysis. Investigation of the overburden effects, including but not limited to their significances, integration of this information into the inversion scheme, and possible consequences due to their uncertainties, should be considered as our future target.

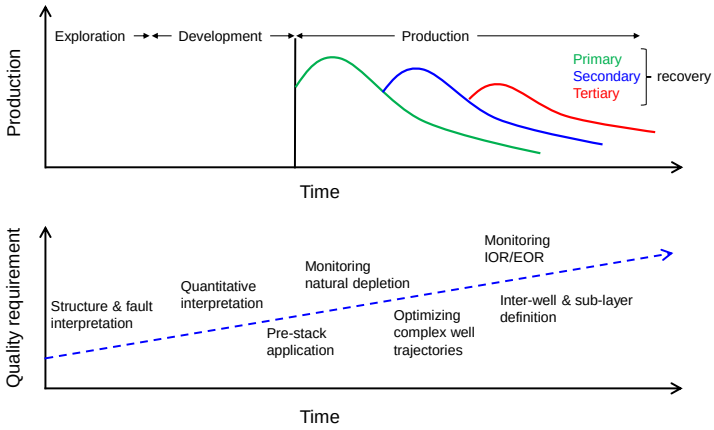

Figure 5.25: Schematic conceptualizing requirements of geophysically derived information in conjunction with the field development profile.

5.6. CONCLUSION

The deblending and data reconstruction scheme introduced in this study simultaneously recovers time-lapse datasets acquired in a blended and irregularly-sampled manner. The implemented strategy minimizes data misfits and promotes sparsity of the estimated data. Additionally, it enables different vintages to communicate with each other, such that static elements among vintages can be shared, while dynamic changes can be extracted according to prior subsurface information. Both synthetic and field data examples presented in this study show the ability of the method to enhance the quality of data recovery as more datasets are fed into the inversion scheme. The approach successfully retrieves time-lapse signatures from irregular, sparse, blended DSA datasets without any particular focus on repeatability in acquisition parameters. This chapter also explores the effect of acquisition design on the performance of the simultaneous data recovery. The real data examples in this study illustrate that quality of recovered data varies with the choice of survey parameters. As compared to a randomly derived design, an acquisition scenario derived from our iterative survey-design method enables us to deliver optimal data recovery and to realize the benefits of compressed time-lapse measurements. As a consequence, properly designed compressed time-lapse measurements along with simultaneous decompression potentially allow us to optimally satisfy various geophysical requirements in different field development phases at an affordable cost and with minimal HSE exposure in the field.

REFERENCES

[1] S. Nakayama, G. Blacquière, T. Ishiyama, and S. Ishikawa, *Blended-acquisition design of irregular geometries towards faster, cheaper, safer and better seismic surveying*, Geophysical Prospecting **67**, 1498 (2019).

[2] S. Nakayama, G. Blacquière, and T. Ishiyama, *Automated survey-design for blended-*

acquisition with irregular spatial sampling via the integration of a metaheuristic and deep learning, Geophysics **84**, P47 (2019).

[3] S. Nakayama and G. Blacquière, *Simultaneous deblending and data reconstruction to supply proper time-lapse datasets throughout the field life in a cost-effective and efficient manner,* Geophysical Journal International **220**, 568 (2020).

[4] C. J. Beasley, E. C. Ronald, and Z. Jiang, *A new look at simultaneous sources,* 68th SEG Annual Meeting, New Orleans, Louisiana, USA, Expanded Abstracts, 133 (1998).

[5] A. J. Berkhout, *Changing the mindset in seismic data acquisition,* The Leading Edge **27**, 924 (2008).

[6] G. Hennenfent and F. J. Herrmann, *Simply denoise: Wavefield reconstruction via jittered undersampling,* Geophysics **73**, V19 (2008).

[7] J. Bouska, *Distance separated simultaneous sweeping, for fast, clean, vibroseis acquisition,* Geophysical Prospecting **58**, 123 (2010).

[8] R. Abma, Q. Zhang, A. Arogunmati, and G. Beaudoin, *An Overview of BP's Marine Independent Simultaneous Source field trials,* 82nd SEG Annual Meeting, Las Vegas, Nevada, USA, Expanded Abstracts, 1 (2012).

[9] F. J. Herrmann, *Randomized sampling and sparsity: Getting more information from fewer samples,* Geophysics **75**, WB173 (2010).

[10] C. C. Mosher, S. T. Kaplan, and F. D. Janiszewski, *Non-uniform optimal sampling for seismic survey design,* 74th EAGE Conference and Exhibition, Copenhagen, Denmark, Extended Abstracts **X034** (2012).

[11] A. J. Berkhout, *Blended acquisition with dispersed source arrays,* Geophysics **77**, A19 (2012).

[12] M. Caporal, G. Blacquière, and M. Davydenko, *Broadband imaging via direct inversion of blended dispersed source array data,* Geophysical Prospecting **66**, 942 (2018).

[13] H. Kutscha and D. J. Verschuur, *Data reconstruction via sparse double focal transformation: An overview,* IEEE Signal Processing Magazine **29**, 53 (2012).

[14] A. Kontakis and D. J. Verschuur, *Deblending via sparsity-constrained inversion in the Focal domain,* 76th EAGE Conference and Exhibition, Amsterdam, The Netherlands, Extended Abstracts **Th ELI1 02** (2014).

[15] C. Li, C. C. Mosher, L. C. Morley, Y. Ji, and J. D. Brewer, *Joint source deblending and reconstruction for seismic data,* 83rd SEG Annual Meeting, Houston, Texas, USA, Expanded Abstracts, 82 (2013).

[16] J. Cheng and M. D. Sacchi, *Separation and reconstruction of simultaneous source via iterative rank reduction,* Geophysics **80**, V57 (2015).

[17] J. Cao, E. Verschuur, H. Gu, and L. Li, *Joint deblending and data reconstruction with focal transformation,* Geophysics **84**, V219 (2019).

[18] F. Oghenekohwo, H. Wason, E. Esser, and F. J. Herrmann, *Low-cost time-lapse seismic with distributed compressive sensing—Part 1: Exploiting common information among the vintages,* Geophysics **82**, P1 (2017).

[19] H. Wason, F. Oghenekohwo, and F. J. Herrmann, *Low-cost time-lapse seismic with distributed compressive sensing—Part 2: Impact on repeatability,* Geophysics **82**, P15 (2017).

[20] T. Ishiyama, M. Y. Ali, S. Ishikawa, G. Blacquière, and S. Nakayama, *Research note: Deblended-data reconstruction using generalized blending and deblending models,* Geophysical Prospecting **67**, 1852 (2019).

[21] S. Qu and D. J. Verschuur, *Simultaneous joint migration inversion for semi-continuous time-lapse seismic data,* 87th SEG Annual Meeting, Houston, Texas, USA, Expanded Abstracts, 5808 (2017).

[22] A. J. Berkhout, *Review Paper: An outlook on the future of seismic imaging, Part I: Forward and reverse modelling,* Geophysical Prospecting **62**, 911 (2014).

[23] D. E. Lumley, R. A. Behrens, and Z. Wang, *Assessing the technical risk of a 4-D seismic project,* The Leading Edge **16**, 1287 (1997).

[24] E. D. Kragh and P. Christie, *Seismic repeatability, normalized rms, and predictability,* The Leading Edge **21**, 640 (2002).

[25] T. Hellem, A. Kjemperud, and O. Ovrcbo, *The troll field: a geological/geophysical model established by the pl085 group,* Habitat of Hydrocarbons on the Norwegian Continental Shelf, 217 (1986).

[26] G. J. O. Vermeer, *3D Seismic Survey Design, Second Edition* (Society of Exploration Geophysicists, 2012).

[27] K. Deb, A. Pratap, S. Agarwal, and T. Meyarivan, *A fast and elitist multiobjective genetic algorithm: NSGA-II,* IEEE Transactions on Evolutionary Computation **6**, 182 (2002).

6

CONCLUSIONS AND RECOMMENDATIONS

6.1. CONCLUSIONS

The primary focus of this thesis is on the development of an iterative scheme to design survey parameters related to both the blending and spatial sampling operators to satisfy pre-set geophysical, operational and economical requirements. This section discusses the main research findings in this thesis.

In **Chapter 2**, we describe the proposed iterative scheme for acquisition design. The workflow aims to find optimum survey parameters responsible for source blending and the spatial sampling of detectors and sources. The proposed approach integrates a genetic algorithm (GA) and a convolutional neural network (CNN) to make optimization feasible within a practical computation time. Genetic operators are capable of simultaneously updating the survey parameters, even in the case of complex blending and irregular spatial sampling schemes, e.g., the dispersed source array (DSA) concept. The network architecture used in the workflow is designed to relate the quality of the final product to the choice of survey parameters. The classification through a CNN helps us to minimize the computation of suboptimal designs while keeping the optimal ones in the iterative scheme. For a further reduction of the computational effort, a repeated encoding sequence is implemented to limit the solution space. Although the proposed approach potentially ends up with a local minimum, this is fully acceptable in our application as long as the resultant acquisition designs satisfy pre-set geophysical requirements.

In **Chapter 3**, we implement the proposed survey design to derive survey parameters that can provide optimum deblending and data reconstruction quality. The results from this chapter clearly show the variation of deblending and data reconstruction quality attributable solely to the design of acquisition scenarios. Optimizing them enhances the performance of deblending and data reconstruction, which is attainable via the proposed approach. The applied network architectures successfully relate the

performance of deblending and data reconstruction to the choice of survey parameters. Our forward modelling can accommodate various types of encoded signatures. This accordingly allows us to simulate several scenarios that resemble acquisition in marine, transition zone, and land environments. The inverse model then makes robust deblending and reconstruction of these data achievable. The method consequently enables us to accommodate various blending and spatial sampling schemes that describe different acquisition scenarios. A strategy to handle two conflicting objectives, i.e., cost and quality, is investigated using a non-dominated sorting genetic algorithm. Our implementation successfully diversifies and spreads out the solutions, and consequently delivers different acquisition scenarios along the Pareto optimal front of cost and quality.

In **Chapter 4**, we extend our design scheme to derive survey parameters that provide optimum subsurface properties estimated directly from blended and irregularly-sampled data. Joint migration inversion (JMI) is applied as the property estimation tool for this implementation. In the workflow, we extended the standard implementation of JMI to cope with the data acquired in a blended fashion along with irregular detector and source geometries. The numerical examples that employ the DSA concept demonstrate the variation of JMI results with the choice of survey design. Optimally designed parameters lead to the enhancement of both reflectivity and velocity models estimated directly from blended and irregularly-sampled data. Genetic operators coupled with non-dominated sorting are capable of minimizing errors in reflectivity and velocity models by simultaneously updating the survey parameters. The neural network architecture applied to this study also relates the performance of JMI to the choice of survey parameters. The proposed approach provides survey parameters to enhance the results of JMI obtained by directly processing blended and irregularly-sampled data without the need for deblending or data reconstruction. The resultant acquisition scenarios allow us to optimally estimate subsurface properties at an affordable cost and with a low environmental footprint.

In **Chapter 5**, we explore a strategy to realize the value of compressed acquisition through the field life. We introduce a deblending and data reconstruction scheme to simultaneously recover time-lapse datasets acquired in a blended and irregularly-sampled manner. The implemented strategy minimizes data misfits and promotes sparsity of the estimated data. Additionally, it enables different vintages to communicate with each other, such that static elements among vintages can be shared, while dynamic changes can be extracted according to prior subsurface information. The synthetic as well as field data examples presented in this chapter show the ability of the method to enhance the quality of data recovery as more datasets are fed into the inversion scheme. The approach successfully retrieves time-lapse signatures from irregular, sparse, blended DSA datasets without any particular focus on acquisition repeatability. We subsequently examine the effect of acquisition design on the performance of simultaneous data recovery. The proposed scheme effectively designs compressed time-lapse surveys that provide an enhanced subsurface image from the individual vintages as well as time-lapse responses that are concordant with dynamic changes in the field.

The contribution of source blending and efficient geometries to a health, safety and environment (HSE) perspective is also discussed in this thesis. Deployment of fewer detectors and blended sources enhances the survey efficiency and accordingly leads to a re-

duced operational risk and environmental footprint in the field. Reduction of shot points with properly designed source signatures via the DSA concept contributes to marine-mammal protection by reducing peak pressure and possibly sound pressure level as well as sound exposure level, without adversely affecting the subsurface illumination.

The proposed workflow provides acquisition scenarios that enable us to realize the benefits of blending and efficient acquisition geometries; thereby enhancing operational efficiency, well managing budgetary and practical constraints, minimizing HSE exposure in the field, yet satisfying pre-set geophysical requirements.

6.2. RECOMMENDATIONS

The primary focus of this thesis is on the retrieval of $\mathbf{X}$ (or $\mathbf{R}$ and $\mathbf{W}$) from $\mathbf{P}'$ by optimally designed acquisition parameters, whereas less emphasis is given to the effect of noise. Blacquière and Nakayama [1] proposed to include realistic noise in the iterative loop to design a seismic survey. As compared to the desired signal, i.e., primary reflections, some types of noise, either incoherent or coherent, potentially employ different characteristics and can be detrimental in the recorded data. For example, Scholte waves offshore Abu Dhabi are characterized by a significantly higher amplitude, lower frequency and lower apparent velocity along with their dispersive and multi-modal nature [2, 3]. Difference in properties between signal and noise potentially imposes certain challenges in the quality measures applied in the proposed survey design scheme. The basis function used in a data recovery algorithm may not sufficiently capture the characteristics of the signal due to the presence of noise, which potentially leads to imperfection in the recovered data. When an applied property estimation tool does not account for some phenomena within the shot-generated wavefield, they are regarded as undesired events. Hence, together with noise, they need to be dealt with prior to feeding data into an algorithm. With JMI, the survey design scheme needs to incorporate a strategy to handle angle dependent reflectivity, anisotropy, mode conversion, refractions, surface waves, anelasticity, etc. Therefore, further investigation towards preprocessing strategies such as suppression of undesired events and preservation of desired ones in $\mathbf{P}'$ prior to a data recovery or a property estimation step would be a worthwhile research direction. This information should then be incorporated into the survey design scheme.

Neural networks and metaheuristics can be flexibly modified, allowing us to adapt them to a problem-specific task. On the other hand, defining a suitable framework is still difficult due to the enormous number of possible choices. For example, our case involves types of operators in the GA, preconditioning of input data for the CNN, architecture of the CNN, and parameters used in each operator in the GA and each layer in the CNN. This consequently makes the design space extremely large and complex. One way to manage this is to set variables in a deterministic fashion through careful experiments and considerations, which still requires a certain amount of effort. On the other hand, there have been numerous studies describing ways to derive frameworks with minimal human intervention. For metaheuristics, several automated approaches have been extensively investigated such as parameter tuning and parameter control [4, 5]. For neural networks, the selection of appropriate hyperparameters as well as architectures can be posed as an optimization problem in itself [6–8]. Exploiting these strategies potentially enables us to develop an automated framework design in conjunction with sur-

vey parameter optimization. Although handcrafting a problem-specific framework may outperform a fully automated method, reduction of human expertise and labour in the latter case would enhance the widespread applicability of the approach. Hence, more research into this area is warranted.

Several possibilities are also considered for further enhancement of optimization efficiency. This thesis indicates that neural networks can relate the choice of survey parameters to the performance of certain processes used as a quality measure. This study, however, does not explicitly examine how the applied architecture classifies solutions and which elements can contribute to a distinction between optimal and suboptimal designs. A better understanding of key information transferred within the network for the prediction is of potential help in survey design. For example, this knowledge may be further utilized as a constraint to allow the algorithm to generate desired solutions and, at the same time, to avoid undesired ones. For the purpose of survey design, the computational burden incurred for evaluating an objective function (data recovery or JMI in our case) may be lessened. For instance, we may reduce the number of iterations for these quality measures during the parameter update, provided that outcomes from a reduced number of iterations can still approximate or infer the results with full iterations. This accordingly makes evaluation of a large number of candidate solutions possible at affordable computational cost. Alternatively, it could accelerate the overall computation. In this case, full iterations would only be required for confirmation of the final solutions. Wu *et al.* [9] proposed a survey design workflow which automatically optimizes detector and source geometries to obtain satisfactory illumination of a chosen subsurface grid. Besides the use of global optimization, they updated the sampling density representing the spatial locations of detectors and sources instead of individual sampling points, requiring fewer parameters to be optimized. This parametrization then enables the use of a gradient descent scheme. Although the technique may become sensitive to nonlinearity of the problem, it possibly contributes to the reduction of computation time as compared to global optimization schemes. Unlike $\mathbf{D}$ or $\mathbf{S}$, accommodating $\mathbf{\Gamma}$ is an intricate task as it consists of frequency- and space-dependent complex numbers. Therefore, exploiting advantages of the density parametrization for spatial sampling schemes coupled with the design of blending schemes would possibly provide a future research venue.

REFERENCES

[1] G. Blacquière and S. Nakayama, *Aquisition Design,* New Advances in Land Geophysical Acquisition Technologies Workshop, Muscat, Oman (2019).

[2] S. Nakayama, M. Benson, T. Matarid, K. Belaid, and D. Zarubov, *Dealing with spatial sampling sparseness and irregularity in 3D OBC seismic data offshore Abu Dhabi,* First Break **34**, 35 (2016).

[3] T. Ishiyama, G. Blacquière, and W. A. Mulder, *The impact of surface-wave attenuation on 3-D seismic survey design,* Geophysical Prospecting **65**, 86 (2017).

[4] B.-B. Thomas, *Experimental Research in Evolutionary Computation* (Springer, 2006).

[5] F. G. Lobo, C. F. Lima, and Z. Michalewicz, *Parameter Setting in Evolutionary Algorithms* (Springer, 2006).

[6] J. Snoek, H. Larochelle, and R. P. Adams, *Practical bayesian optimization of machine learning algorithms,* In Proceedings of the 25th International Conference on Neural Information Processing System, 2960– (2012).

[7] B. Baker, O. Gupta, N. Naik, and R. Raskar, *Designing neural network architectures using reinforcement learning,* 5th International Conference on Learning Representations (2017).

[8] M. Suganuma, S. Shirakawa, and T. Nagao, *A genetic programming approach to designing convolutional neural network architectures,* Proceedings of the Genetic and Evolutionary Computation Conference, 497 (2017).

[9] S. Wu, E. Verschuur, and G. Blacquière, *Automated target-oriented acquisition design: Optimizing both source and receiver geometries,* 89th SEG Annual Meeting, San Antonio, Texas, USA, Expanded Abstracts, 142 (2019).

A

JOINT DEBLENDING AND DATA RECONSTRUCTION

A

This appendix provides theoretical frameworks of joint deblending and data reconstruction implemented in Chapter 3. The separation of blended data and the reconstruction of missing data can share a certain resemblance. Both cases are often treated as an inverse problem that involves iterative estimation of desired signals and subtraction of undesired ones, i.e.., blending and aliasing noise, in the model space domain. Kutscha and Verschuur [1], for instance, imposed an L1 constraint in the Focal domain to handle the reconstruction problem. Kontakis and Verschuur [2] then extended this scheme to deblending. Additionally, Li *et al.* [3], Cheng and Sacchi [4], Cao *et al.* [5] jointly dealt with deblending and reconstruction.

According to our forward model described in Equation 2.7, the general solution to obtain deblended and reconstructed data is given by:

$$\langle \mathbf{X} \rangle = \mathbf{D}^H (\mathbf{D}\mathbf{D}^H)^{-1} \mathbf{P}^{'} ({\mathbf{S}^{'}}^H \mathbf{S}^{'})^{-1} {\mathbf{S}^{'}}^H. \tag{A.1}$$

However, this particular solution often faces difficulty in dealing with the under-determined inverse problem. We, therefore, apply an iterative scheme to estimate $\langle \mathbf{X} \rangle$, in the 3D frequency-wavenumber domain.

Using the Fourier transform operator, $\mathbf{L}$, and its adjoint, $\mathbf{L}^H$, we describe the forward and inverse transforms as:

$$\mathbf{L}\mathbf{X} = \mathbf{M}, \tag{A.2}$$

and

$$\mathbf{X} = \mathbf{L}^H \mathbf{M}. \tag{A.3}$$

Here, $\mathbf{M}$ represents the model parameters in the transform domain. Therefore, an optimum estimate of $\langle \mathbf{M} \rangle$ leads to:

$$\langle \mathbf{X} \rangle = \mathbf{L}^H \langle \mathbf{M} \rangle . \tag{A.4}$$

Mahdad *et al.* [6] utilized an iterative deblending scheme using sparseness and coherency constraints. Ishiyama *et al.* [7] established a generalized blending model and a deblended-data reconstruction method based on this model. Following these studies, we formulate an inverse scheme based on the L1 norm optimization as:

$$\min \| \langle \mathbf{M} \rangle \|_1 \text{ s.t. } \mathbf{P}' = \mathbf{D} \langle \mathbf{X} \rangle \mathbf{S}^{'}. \tag{A.5}$$

We deal with the inverse problem via the alternating direction method of multipliers (ADMM), classified as one of the augmented Lagrangian methods [8]. ADMM decomposes a given optimization problem into sub-problems, each of which updates different variables derived from the original objective function. Equation A.5 is considered as a constrained Basis pursuit problem, in which ADMM splits the primal variable $\langle \mathbf{M} \rangle$ in Equation A.5 into two separate variables, here called $\langle \mathbf{M}_1 \rangle$ and $\langle \mathbf{M}_2 \rangle$. These two variables are updated in a sequential or alternating manner, along with an equality constraint imposed between the two. According to [9], Equation A.5 can be rewritten as:

$$\min f(\langle \mathbf{M}_1 \rangle) + \| \langle \mathbf{M}_2 \rangle \|_1 \text{ s.t. } \langle \mathbf{M}_1 \rangle - \langle \mathbf{M}_2 \rangle = 0, \tag{A.6}$$

Here, $f(\langle \mathbf{M}_1 \rangle)$ is the indicator function of $\langle \mathbf{M}_1 \rangle | \mathbf{P}' = \mathbf{D} \langle \mathbf{X} \rangle \mathbf{S}'$, which accounts for minimizing the data misfit, while $\| \langle \mathbf{M}_2 \rangle \|_1$ accounts for promoting the sparsity of data. ADMM solves for the two variables separately and subsequently updates another variable $\mathbf{U}$ called a Lagrange multiplier which performs a dual variable update. The $(i+1)^{\text{th}}$ updates of sub-problems in ADMM are given by:

$$\begin{aligned} \langle \mathbf{M}_1 \rangle_{i+1} &= P_c \left(\left\langle \underline{\mathbf{M}_2} \right\rangle_i - \underline{\mathbf{U}}_i \right), \\ \langle \mathbf{M}_2 \rangle_{i+1} &= S_\rho \left(\langle \mathbf{M}_1 \rangle_{i+1} - \underline{\mathbf{U}}_i \right), \\ \mathbf{U}_{i+1} &= \underline{\mathbf{U}}_i + \langle \mathbf{M}_1 \rangle_{i+1} - \langle \mathbf{M}_2 \rangle_{i+1}, \end{aligned} \tag{A.7}$$

where $\left\langle \underline{\mathbf{M}_2} \right\rangle$ and $\underline{\mathbf{U}}$ represent data after the application of preconditioning to $\langle \mathbf{M}_2 \rangle$ and $\mathbf{U}$. It consists of the constraints based on causality and coherency of the data. $S_\rho(x)$ in Equation A.7 is a soft-thresholding operator defined by:

$$S_\rho(x) = \begin{cases} x - \rho & (x > \rho) \\ 0 & (-\rho \le x \le \rho) \\ x + \rho & (x < -\rho) \end{cases}. \tag{A.8}$$

Here, ρ is a user-defined penalty parameter. P_c in Equation A.7 is the projection onto $\langle \mathbf{M}_1 \rangle | \mathbf{P}' = \mathbf{D} \langle \mathbf{X} \rangle \mathbf{S}'$ given by:

$$P_c \left(\underline{\mathbf{M}_2}_i - \underline{\mathbf{U}}_i \right) = \mathbf{L} \left[\mathbf{L}^H \left(\underline{\mathbf{M}_2}_i - \underline{\mathbf{U}}_i \right) + \alpha \mathbf{A}_i \right], \tag{A.9}$$

where

$$\mathbf{A}_i = \mathbf{D}^H \left(\mathbf{D}\mathbf{D}^H \right)^{-1} \Delta \mathbf{P}'_i \left(\mathbf{S}'^H \mathbf{S}' \right)^{-1} \mathbf{S}'^H, \tag{A.10}$$

with

$$\Delta \mathbf{P}'_i = \mathbf{P}' - \mathbf{D} \left[\mathbf{L}^H \left(\underline{\mathbf{M}_2}_i - \underline{\mathbf{U}}_i \right) \right] \mathbf{S}'. \tag{A.11}$$

In an ADMM form, α is fixed to one. It can also be altered through the course of iterations, e.g., by satisfying:

$$\sum\nolimits_\omega \left\| \Delta \mathbf{P}'_i - \alpha_i \mathbf{B}_i \right\|_2^2 \to \min, \tag{A.12}$$

with

$$\mathbf{B}_i = \mathbf{D}\mathbf{A}_i \mathbf{S}'. \tag{A.13}$$

Therefore, the scalar factor that can make the partial derivative of Equation A.12 with respect α_i zero is:

$$\alpha_i = \frac{\sum_\omega \operatorname{tr} \left[\Delta \mathbf{P}'^H_i \mathbf{B}_i \right]}{\sum_\omega \operatorname{tr} \left[\mathbf{B}_i^H \mathbf{B}_i \right]}. \tag{A.14}$$

Hence, the inversion scheme promotes the sparsity of the solution while minimizing the misfit between $\mathbf{P}'$ and $\mathbf{D} \langle \mathbf{X} \rangle \mathbf{S}'$. Along with the previously mentioned constraints, an estimate of $\langle \mathbf{X} \rangle$ from $\mathbf{P}'$ is possible.

A

REFERENCES

[1] H. Kutscha and D. J. Verschuur, *Data reconstruction via sparse double focal transformation: An overview,* IEEE Signal Processing Magazine **29**, 53 (2012).

[2] A. Kontakis and D. J. Verschuur, *Deblending via sparsity-constrained inversion in the Focal domain,* 76th EAGE Conference and Exhibition, Amsterdam, The Netherlands, Extended Abstracts **Th ELI1 02** (2014).

[3] C. Li, C. C. Mosher, L. C. Morley, Y. Ji, and J. D. Brewer, *Joint source deblending and reconstruction for seismic data,* 83rd SEG Annual Meeting, Houston, Texas, USA, Expanded Abstracts, 82 (2013).

[4] J. Cheng and M. D. Sacchi, *Separation and reconstruction of simultaneous source via iterative rank reduction,* Geophysics **80**, V57 (2015).

[5] J. Cao, E. Verschuur, H. Gu, and L. Li, *Joint deblending and data reconstruction with focal transformation,* Geophysics **84**, V219 (2019).

[6] A. Mahdad, P. Doulgeris, and G. Blacquière, *Separation of blended data by iterative estimation and subtraction of blending interference noise,* Geophysics **76**, Q9 (2011).

[7] T. Ishiyama, M. Y. Ali, S. Ishikawa, G. Blacquière, and S. Nakayama, *Research note: Deblended-data reconstruction using generalized blending and deblending models,* Geophysical Prospecting **67**, 1852 (2019).

[8] DanielGabay and B. Mercier, *A dual algorithm for the solution of nonlinear variational problems via finite element approximation,* Computers and Mathematics with Applications **2**, 17 (1976).

[9] S. Boyd, N. Parikh, E. Chu, B. Peleato, and J. Eckstein, *Distributed optimization and statistical learning via the alternating directionmethod of multipliers,* Foundations and Trends in Machine Learning **3**, 1 (2010).

B

JOINT MIGRATION INVERSION

B

This appendix provides theoretical frameworks of full wavefield modelling (FWMod) and joint migration inversion (JMI) implemented in Chapter 4, which is based fundamentally on [1–3]. We first describe the representation for the reflection, transmission and propagation in FWMod, responsible for the forward modelling module in JMI. As illustrated in Figure B.1, the upward and downward outgoing wavefields leaving a given depth level z_m, $\mathbf{Q}^-(z_m)$ and $\mathbf{Q}^+(z_m)$, can be represented as the sum of the transmitted incoming wavefields in the same propagation direction and the wavefields reflected from the opposite direction as:

$$\begin{aligned}\mathbf{Q}^-(z_m) &= \mathbf{T}^-(z_m)\mathbf{P}^-(z_m) + \mathbf{R}^{\cup}(z_m)\mathbf{P}^+(z_m),\\ \mathbf{Q}^+(z_m) &= \mathbf{T}^+(z_m)\mathbf{P}^+(z_m) + \mathbf{R}^{\cap}(z_m)\mathbf{P}^-(z_m),\end{aligned} \tag{B.1}$$

where $\mathbf{P}^-(z_m)$ and $\mathbf{P}^+(z_m)$ are the upward and downward incoming wavefields respectively. Matrices $\mathbf{R}^{\cup}(z_m)$ and $\mathbf{R}^{\cap}(z_m)$ are the the down-up reflectivity operator and the up-down reflectivity operator, respectively. Matrices $\mathbf{T}^-(z_m)$ and $\mathbf{T}^+(z_m)$ represent the up- and downgoing transmission at the discontinuity, which can be expressed as:

$$\mathbf{T}^{\mp}(z_m) = \mathbf{I} + \delta\mathbf{T}^{\mp}(z_m), \tag{B.2}$$

where $\delta\mathbf{T}^{\mp}(z_m)$ are the differential transmission operators. Combining Equations B.1 and B.2 yields:

$$\begin{aligned}\mathbf{Q}^-(z_m) &= \mathbf{P}^-(z_m) + \delta\mathbf{T}^-(z_m)\mathbf{P}^-(z_m) + \mathbf{R}^{\cup}(z_m)\mathbf{P}^+(z_m),\\ \mathbf{Q}^+(z_m) &= \mathbf{P}^+(z_m) + \delta\mathbf{T}^+(z_m)\mathbf{P}^+(z_m) + \mathbf{R}^{\cap}(z_m)\mathbf{P}^-(z_m),\end{aligned} \tag{B.3}$$

where the last two terms on the right of both equations account for scattering effects at z_m. These terms can be combined to:

$$\begin{aligned}\delta\mathbf{S}^-(z_m) &= \delta\mathbf{T}^-(z_m)\mathbf{P}^-(z_m) + \mathbf{R}^{\cup}(z_m)\mathbf{P}^+(z_m),\\ \delta\mathbf{S}^+(z_m) &= \delta\mathbf{T}^+(z_m)\mathbf{P}^+(z_m) + \mathbf{R}^{\cap}(z_m)\mathbf{P}^-(z_m),\end{aligned} \tag{B.4}$$

leading to:

$$\begin{aligned}\mathbf{Q}^-(z_m) &= \mathbf{P}^-(z_m) + \delta\mathbf{S}^-(z_m),\\ \mathbf{Q}^+(z_m) &= \mathbf{P}^+(z_m) + \delta\mathbf{S}^+(z_m).\end{aligned} \tag{B.5}$$

The propagation operators $\mathbf{W}^-(z_{m-1}, z_m)$ and $\mathbf{W}^+(z_{m+1}, z_m)$ then enable the outgoing wavefields $\mathbf{Q}^{\mp}(z_m)$ to be extrapolated to the next depth levels $z_{m\mp1}$ (Figure B.1).

Berkhout [2] summarized the scattering and propagation processes, recursively occurring at each depth for the downward wavefields ($m = 1, 2, \ldots, M_{\mathrm{d}}$) and the upward wavefields ($m = 1, 2, \ldots, M_{\mathrm{d}} - 1$) as follows:

$$\begin{aligned}\mathbf{P}^+(z_m; z_0) &= \underset{-}{\mathbf{W}}{}^+(z_m, z_0)\mathbf{S}^+(z_0) + \sum_{n=0}^{m-1} \underset{-}{\mathbf{W}}{}^+(z_m, z_n)\mathbf{R}^{\cap}(z_n)\mathbf{P}^-(z_n; z_0),\\ \mathbf{P}^-(z_m; z_0) &= \underset{-}{\mathbf{W}}{}^-(z_m, z_{M_{\mathrm{d}}})\mathbf{P}^-(z_{M_{\mathrm{d}}}; z_0) + \sum_{n=m+1}^{M_{\mathrm{d}}} \underset{-}{\mathbf{W}}{}^-(z_m, z_n)\mathbf{R}^{\cup}(z_n)\mathbf{P}^+(z_n; z_0),\end{aligned} \tag{B.6}$$

with

$$\begin{aligned}\underset{-}{\mathbf{W}}{}^+(z_m, z_n) &= \mathbf{W}^+(z_m, z_{m-1}) \prod_{l=m-1}^{n+1} \mathbf{T}^+(z_l)\mathbf{W}^+(z_l, z_{l-1}),\\ \underset{-}{\mathbf{W}}{}^-(z_m; z_n) &= \mathbf{W}^-(z_m, z_n) \prod_{l=m+1}^{n-1} \mathbf{T}^-(z_l)\mathbf{W}^-(z_l, z_{l+1}).\end{aligned} \tag{B.7}$$

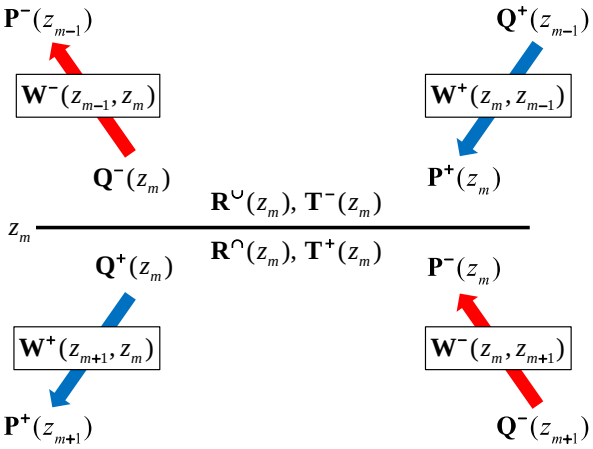

Figure B.1: The incoming and outgoing wavefields in the upward and downward directions, propagating between two depths levels, z_m and $z_{m\pm1}$, as well as being reflected and transmitted at a depth level of z_m (after [1]).

In the following, the reflectively and velocity updates through JMI are discussed. The assumptions of no wave conversion and frequency/angle-independent reflectivity used in the applied JMI process allow for:

$$\begin{aligned} &\mathbf{R}^\cup(z_m) \approx -\mathbf{R}^\cap(z_m) \approx \mathbf{R}(z_m), \\ &\delta\mathbf{T}(z_m)^{\mp} \approx \mp\mathbf{R}(z_m). \end{aligned} \tag{B.8}$$

As shown in Figure B.2, JMI iteratively optimizes velocity and reflectivity models by minimizing the misfit between input and modelled data derived from FWMod as:

$$J = \sum_\omega \|\Delta\mathbf{P}^-(z_0)\|_2^2 = \sum_\omega \|\mathbf{P}^-(z_0) - \langle\mathbf{P}^-(z_0)\rangle\|_2^2, \tag{B.9}$$

where $\mathbf{P}^-(z_0)$ and $\langle\mathbf{P}^-(z_0)\rangle$ represent the observed data and forward-modelled data in the frequency domain recorded at the depth of z_0. As described in Chapter 4, Equation B.9 can be extended to blended and irregularly-sampled data.

Based on [3], a gradient descent scheme is applied to minimize the residual between the observed and forward-modelled data via the reflectivity and velocity updates. Using a given initial reflectivity operator, $\mathbf{R}_0(z_m)$, the true operator can be written as:

$$\mathbf{R}(z_m) = \mathbf{R}_0(z_m) + \Delta\mathbf{R}(z_m), \tag{B.10}$$

where $\Delta\mathbf{R}(z_m)$ is the reflectivity gradient given by:

$$\Delta\mathbf{R}(z_m) = \sum_\omega \underline{\mathbf{W}}^-(z_0, z_m)^H \Delta\mathbf{P}^-(z_0)\mathbf{P}^+(z_m)^H. \tag{B.11}$$

It is a square matrix that contains the gradient values of the reflectivity along its diagonal. All off-diagonal elements of $\Delta\mathbf{R}(z_m)$ are discarded in the followings steps, making

$\Delta\mathbf{R}(z_m)$ a diagonal matrix. The gradient is computed by multiplication of the back-propagated residual and the forward-propagated source fields and then by summing over frequencies at each depth level. Therefore, the wavefield perturbation due to $\Delta\mathbf{R}$ at each depth level is:

$$\Delta\mathbf{P}_r^-(z_0) = \sum_{n=1}^{M_d} \mathbf{W}^-(z_0, z_n)\Delta\mathbf{R}(z_n)\mathbf{P}^+(z_n; z_0). \tag{B.12}$$

A scaling factor α_r that can minimize the residual is given by:

$$\left\|\Delta\mathbf{P}^-(z_0) - \alpha_r\Delta\mathbf{P}_r^-(z_0)\right\|_2^2 \to \min. \tag{B.13}$$

The value of α_r that can make the partial derivative of the expression in Equation B.13 with respect to α_r equal zero is:

$$\alpha_r = \frac{\sum_\omega \mathrm{tr}\left[\Delta\mathbf{P}_r^-(z_0)^H\Delta\mathbf{P}^-(z_0)\right]}{\sum_\omega \mathrm{tr}\left[\Delta\mathbf{P}_r^-(z_0)^H\Delta\mathbf{P}_r^-(z_0)\right]}. \tag{B.14}$$

The reflectivity model is updated from $\mathbf{R}_\mathrm{i}$ to $\mathbf{R}_{\mathrm{i}+1}$ at each iteration according to:

$$\mathbf{R}_{i+1}(z_m) = \mathbf{R}_i(z_m) + \alpha_r\Delta\mathbf{R}(z_m). \tag{B.15}$$

Using given initial upward and downward propagation operators between two depth levels, z_m and z_{m+1}, the true propagation operators can be written as:

$$\begin{aligned}\mathbf{W}^-(z_m, z_{m+1}) &= \mathbf{W}_0^-(z_m, z_{m+1}) + \Delta\mathbf{W}^-(z_m, z_{m+1}),\\ \mathbf{W}^+(z_{m+1}, z_m) &= \mathbf{W}_0^+(z_{m+1}, z_m) + \Delta\mathbf{W}^+(z_{m+1}, z_m).\end{aligned} \tag{B.16}$$

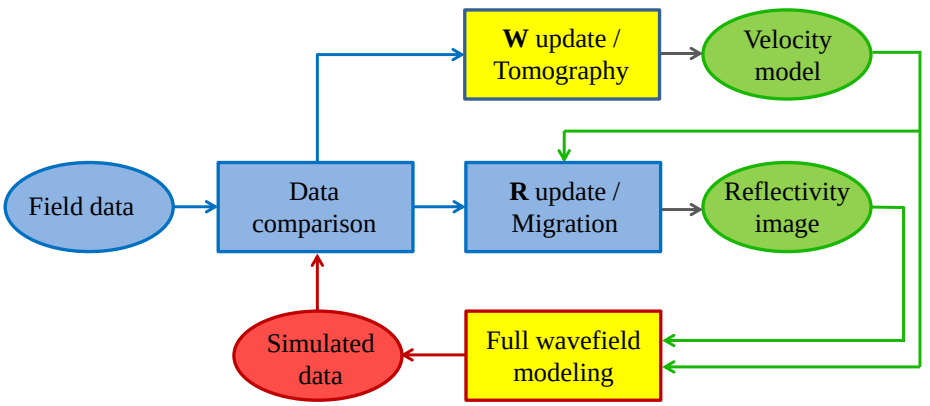

Figure B.2: JMI flow chart (after [4]).

The update direction for the propagation operators can be calculated by:

$$\begin{aligned}\Delta\mathbf{W}^{-}(z_m, z_{m+1}) &= \mathbf{V}_j^{-}(z_0, z_m)^H \Delta\mathbf{P}_i^{-}(z_0)\mathbf{Q}_j^{-}(z_{m+1})^H,\\ \Delta\mathbf{W}^{+}(z_{m+1}, z_m) &= \mathbf{V}_j^{\cup}(z_0, z_{m+1})^H \Delta\mathbf{P}_i^{-}(z_0)\mathbf{Q}_j^{+}(z_m)^H,\end{aligned} \tag{B.17}$$

with

$$\begin{aligned}\mathbf{V}_j^{-}(z_0, z_m) &= \underset{-}{\mathbf{W}}_j^{-}(z_0, z_m)\left[\mathbf{I} - \mathbf{R}_j(z_m)\right],\\ \mathbf{V}_j^{\cup}(z_0, z_{m+1}) &= \underset{-}{\mathbf{W}}_j^{-}(z_0, z_m)\mathbf{R}_j(z_m) + \sum_{n=m+1}^{M_\mathrm{d}} \underset{-}{\mathbf{W}}_j^{-}(z_0, z_n)\mathbf{R}_j(z_n)\underset{-}{\mathbf{W}}_j^{+}(z_n, z_m)\left[\mathbf{I} + \mathbf{R}_j(z_n)\right],\end{aligned} \tag{B.18}$$

and

$$\begin{aligned}\mathbf{Q}_j^{-}(z_m) &= \left[\mathbf{I} - \mathbf{R}_j(z_m)\right]\mathbf{P}_j^{-}(z_m) + \mathbf{R}_j(z_m)\mathbf{P}_j^{+}(z_m),\\ \mathbf{Q}_j^{+}(z_m) &= \left[\mathbf{I} + \mathbf{R}_j(z_m)\right]\mathbf{P}_j^{+}(z_m) - \mathbf{R}_j(z_m)\mathbf{P}_{j-1}^{-}(z_m),\end{aligned} \tag{B.19}$$

where j represents the number of round trips. The propagation operators act as phase-shift operators in the wavenumber domain:

$$\tilde{w}(k_x, \omega) = \exp(-jk_z\Delta z), \tag{B.20}$$

with

$$k_z(\sigma) = \sqrt{\omega^2\sigma^2 - k_x^2}, \tag{B.21}$$

where σ denotes slowness. Their perturbations then allow us to linearize $\tilde{w}$ and slowness, σ:

$$\Delta\tilde{w} = \tilde{w}_{i+1} - \tilde{w}_i \approx \left[\frac{\partial\tilde{w}}{\partial\sigma}\right]_{\sigma_i}\Delta\sigma = -j\omega\Delta z\left[\frac{k}{k_z}\right]_{\sigma_i}\tilde{w}_i\Delta\sigma, \tag{B.22}$$

with

$$k = \omega\sigma, \tag{B.23}$$

where $\tilde{w}_{i+1}$ is the propagation operator in the updated slowness model, σ_{i+1} while $\tilde{w}_i$ is the propagation operator in the current slowness model, σ_i. Based on this linearised relationship between $\Delta\tilde{w}$ and $\Delta\sigma$, Staal [3] defined an operator $\mathbf{G}$. Each row of $\mathbf{G}$ in the wavenumber domain is given as:

$$\vec{\tilde{G}} = -j\omega\Delta z\left[\frac{k_z^* k}{|k_z|^2 + \epsilon}\right]_{\sigma_i} e^{-jk_z\Delta z}e^{-jk_x x_j}, \tag{B.24}$$

where ϵ is a stabilization parameter, and $*$ denotes the complex conjugate. This can relate propagation operators to propagation slowness as:

$$\begin{aligned}\Delta\mathbf{W}^{-}(z_m, z_{m+1}) &\approx \mathbf{G}^{-}(z_m, z_{m+1})\Delta\boldsymbol{\sigma}(z_m),\\ \Delta\mathbf{W}^{+}(z_{m+1}, z_m) &\approx \mathbf{G}^{+}(z_{m+1}, z_m)\Delta\boldsymbol{\sigma}(z_m),\end{aligned} \tag{B.25}$$

where $\Delta\boldsymbol{\sigma}(z_m)$ is a square matrix that has the slowness update of each location at the depth level of z_m along its diagonal. The slowness gradient is given by:

$$\begin{aligned}\Delta\boldsymbol{\sigma}^{'}(z_m) &= \sum_{\omega}\left[\mathbf{G}^{-}(z_m, z_{m+1})\right]^H\Delta\mathbf{W}^{-}(z_m, z_{m+1}),\\ &+ \sum_{\omega}\left[\mathbf{G}^{+}(z_{m+1}, z_m)\right]^H\Delta\mathbf{W}^{+}(z_{m+1}, z_m).\end{aligned} \tag{B.26}$$

All off-diagonal elements of $\Delta\boldsymbol{\sigma}^{'}(z_m)$ are discarded in the followings steps, making $\Delta\boldsymbol{\sigma}^{'}(z_m)$ a diagonal matrix. Therefore, the wavefield perturbation due to $\Delta\boldsymbol{\sigma}^{'}$ at each depth level is obtained as:

$$\begin{aligned}\Delta\mathbf{P}^{-}_{\sigma}(z_0) \quad &= \sum_{n=1}^{M_{\mathrm{d}}} \mathbf{V}^{-}_{j}(z_0,z_n)\Delta\boldsymbol{\sigma}^{'}(z_n)\mathbf{G}^{-}(z_n,z_{n+1})\mathbf{Q}^{-}_{j}(z_{n+1}),\\ &+ \sum_{n=1}^{M_{\mathrm{d}}} \mathbf{V}^{\cup}_{j}(z_0,z_{n+1})\mathbf{G}^{+}(z_{n+1},z_n)\Delta\boldsymbol{\sigma}^{'}(z_n)\mathbf{Q}^{+}_{j}(z_n).\end{aligned} \tag{B.27}$$

A scaling factor α_σ that can minimize the residual is given by:

$$\left\|\Delta\mathbf{P}^{-}(z_0) - \alpha_\sigma\Delta\mathbf{P}^{-}_{\sigma}(z_0)\right\|^2 \rightarrow \min. \tag{B.28}$$

The value of α_σ that can make the partial derivative of the expression in Equation B.28 with respect to α_σ equal to zero is:

$$\alpha_\sigma = \frac{\sum_\omega \mathrm{tr}\left[\Delta\mathbf{P}^{-}_{\sigma}(z_0)^H\Delta\mathbf{P}^{-}(z_0)\right]}{\sum_\omega \mathrm{tr}\left[\Delta\mathbf{P}^{-}_{\sigma}(z_0)^H\Delta\mathbf{P}^{-}_{\sigma}(z_0)\right]}. \tag{B.29}$$

The slowness model is updated from $\boldsymbol{\sigma}_i$ to $\boldsymbol{\sigma}_{i+1}$ at each iteration according to:

$$\boldsymbol{\sigma}_{i+1}(z_m) = \boldsymbol{\sigma}_i(z_m) + \alpha_\sigma\Delta\boldsymbol{\sigma}^{'}(z_m). \tag{B.30}$$

REFERENCES

[1] X. R. Staal and D. J. Verschuur, *Joint migration inversion, imaging including all multiples with automatic velocity update,* 75th EAGE Annual Meeting, London, UK, Extended Abstracts **Tu 02 16** (2013).

[2] A. J. Berkhout, *Review Paper: An outlook on the future of seismic imaging, Part I: Forward and reverse modelling,* Geophysical Prospecting **62**, 911 (2014).

[3] X. R. Staal, *Combined imaging and velocity estimation by Joint Migration Inversion* (Delft University of Technology, Ph.D Thesis, 2015).

[4] S. Qu and D. J. Verschuur, *Simultaneous joint migration inversion for semi-continuous time-lapse seismic data,* 87th SEG Annual Meeting, Houston, Texas, USA, Expanded Abstracts, 5808 (2017).

ACKNOWLEDGEMENTS

First of all, I would like to express my sincere appreciation to my promotor and my daily supervisor, Dr. Gerrit Blacquière. Putting my gratitude to him into words is one of the most difficult parts in my thesis as his supervision has helped me in all the time of my PhD and has extended to various aspects. In addition to a regular weekly meeting, he spent his valuable time for me even when he was not at the university. In addition to the amount of time devoted for me, he always provided me with highly critical and logical feedbacks from both theoretical and practical point of views. His supportive and positive attitude always motivated me a lot. Since I joined TU Delft, I have learnt a lot from him. Without his supervision, I am quite sure that I would not have reached the point where I am today. I am very honoured and happy to be his student. Besides my supervisor, I am grateful to Dr. Eric Verschuur. Together with Dr. Gerrit Blacquière, he provided me with an opportunity to join the Delphi Consortium and TU Delft. I thank him for his effort to lead the consortium and make a pleasant research environment available to us. I was really fortunate to observe his way of managing the consortium to move things forward in the right direction together with a large number of sponsors. I would like to convey my deep appreciation to Prof. Kees Wapenaar who kindly accepted to become my promotor despite his extremely busy schedule. I am grateful for his sharp, critical and supportive feedback on my research and also for his generous support to the applied geophysics section. My gratitude also extends to Prof. Evert Slob, Prof. Wim Mulder, Prof. Dirk Gajewski, Dr. Guy Drijkoningen and Dr. Guido Baeten for accepting to serve on the doctoral committee members and for admitting me to the defense ceremony with thorough assessments.

This thesis would not have existed without the financial support from INPEX. I am indebted to the management of INPEX, particularly, Mr. Masaharu Sano, Mr. Takahiko Ikeda, Mr. Nobuharu Sase, Mr. Hiroshi Nakamura, and Mr. Kuniaki Takayama, for their approvals of my proposal to carry out the research at TU Delft. I must thank my former managers, Mr. Toshiya Oshita, Ms. Mayu Otake and Mr. Kaneyoshi Miyake, for their kind understating of my willingness. I would like to express my deep gratitude to Dr. Tomo Ishiyama who has been of great help to me since 2010. Without him, my interest toward survey design would never have been aroused, and my desire to pursue a PhD study would never have been awakened. Special acknowledgements go to Dr. Isao Takahashi and Mr. Takahiro Watanabe for their clear advices that really encouraged me to pursue the research at TU Delft. I am grateful to all the former colleagues in the technical resources unit for creating a supportive atmosphere towards my decision and their words of encouragement.

I would like to acknowledge my colleagues in Abu Dhabi where I was able to gain valuable skills, knowledge and experience on multi-national and multi-cultural work environments as well as seismic operations including blended acquisition. In particular, Mr. Kamal Belaid, Mr. Thierry Francis Lecoq, Mr. Mark Allen Benson, Mr. Gary

Mercado, Mr. Khalfan Hassan Al-Mansoor, Mr. Ahmed Mubarak Al-Khamiri, and Mr. Ismail Abdulla Al-Darmaki are greatly acknowledged for guiding me deep into the world of geophysics and for allowing me to work in an enjoyable environment. I never forget my memorable 6 years in ADMA-OPCO. I always dream about gathering the best team at Dick El Jin once again. In addition to them, my assignment in Abu Dhabi provided me with a great opportunity to have valuable interactions with two geophysicists, Mr. Hiroshi Hagiwara and Mr. Hiroyuki Inoue, whom I aspire to be like. This ambition motivated me and eventually made me decide to develop myself further at TU Delft.

Warm thanks go to all the colleagues in the Delphi team - Mikahil Davydenko, Aayush Garg, Hussain Hammad, Aparajita Nath, Dong Zang, Nick Luiken, Runhai Feng, Siddarth Sharma, Leo Hoogerbrugge, Siamak Abolhassani, Lele Zhang, Ali Alfaraj, Halah Alasmari, Bouchaib El Marhfoul and Silvia Pintea - for giving me a fun time in the consortium. I wish to thank Shogo Masaya who gave me helpful advises in his calm tone during my stay and even before I joined TU Delft. I am very thankful to Delphi acquisition and preprocessing guys in CiTG - Matteo Caporal, Sixue Wu, Jan-Willem Vrolijk, Billy Revelo, Junhai Cao and Özekan Sertlek - for inspiring me by their outstanding research works and for teaching me a way to survive in the consortium and the faculty. I also wish to express my deep appreciation to Prof. Guus Berkhout (the founder and the former director of the consortium) and all the sponsors, staff, supervisors and alumni involved in the consortium. Although I have never met quite some of them, I wish to thank all of them for the incredible research history, culture and environment that they have created for nearly 40 years. I am also grateful to all the colleagues and staff in CiTG for their continuous support throughout my PhD. I thank Joeri Brackenhoff for the translation of my summary in Dutch.

I would like to thank my parents and my sister for their tremendous amount of care and support throughout my life. Despite the long physical distance between us, I always feel connected to each of you. Last but by no means least, I thank with love to my wife, son and daughter. Thank you for giving me your unconditional love and for being always by my side. You always encourage me, bring me a smile and make my life delightful, beautiful and meaningful. Miho, Yutaro and Nodoka, each of you was, is and will forever be my greatest treasure. Thanks to you, I was able to spend a pleasant time throughout the stay in Delft. Everything I have done I owe to you.

Shotaro Nakayama
Delft, the Netherlands, March 2020

CURRICULUM VITÆ

Shotaro NAKAYAMA

CAREER

2017–2020	PhD in Applied Geophysics Delft University of Technology, Delft, the Netherlands *Thesis:* Optimization of blending and spatial sampling in seismic acquisition design *Promotors:* Dr. ir. G. Blacquière Prof. dr. ir. C.P.A. (Kees) Wapenaar
2016–Present	Geophysicist INPEX Corporation
2010–2016	Geophysicist Abu Dhabi Marine Operating Company
2007–2010	Geophysicist INPEX Corporation

LIST OF PUBLICATIONS

11. **S. Nakayama** and G. Blacquière, *Simultaneous deblending and data reconstruction to supply proper time-lapse datasets throughout the field life in a cost-effective and efficient manner*, Geophysical Journal International **220**(1), 568-584 (2020).

10. **S. Nakayama**, G. Blacquière and T. Ishiyama, *Acquisition design for direct reflectivity and velocity estimation from blended and irregularly-sampled data*, Geophysical Prospecting **67**(8), 2127-2146 (2019).

9. **S. Nakayama**, G. Blacquière and T. Ishiyama, *Automated survey-design for blended-acquisition with irregular spatial sampling via the integration of a metaheuristic and deep learning*, Geophysics **84**(4), P47-P60 (2019).

8. T. Ishiyama, M.A. Ali, S. Ishikawa, G. Blacquière and **S. Nakayama**, *Research note: Deblended-data reconstruction using generalized blending and deblending models*, Geophysical Prospecting **67**(7), 1852-1866 (2019).

7. **S. Nakayama**, G. Blacquière, T. Ishiyama and S. Ishikawa, *Blended-acquisition design of irregular geometries towards faster, cheaper, safer and better seismic surveying*, Geophysical Prospecting **67**(6), 1498-1521 (2019).

6. **S. Nakayama**, M.A. Benson, T. Materid, K. Belaid and D. Zarubov, *Dealing with spatial sampling sparseness and irregularity in 3D OBC seismic data offshore Abu Dhabi*, First Break **34**(2), 35-42 (2016).

5. **S. Nakayama**, G. Mercado, M.A. Benson, K. Belaid and M. Garden, *Field-wide implementation of time and distance separated source techniques on a 3D OBC survey offshore Abu Dhabi, UAE*, First Break **33**(4), 47-53 (2015).

4. **S. Nakayama**, K. Belaid and T. Ishiyama, *Seeking efficient OBC survey designs that still satisfy established geophysical objectives*, First Break **31**(10), 65-73 (2013).

3. N. Kimura, **S. Nakayama**, K. Tsukimura, S. Miwa, A. Okamoto and T. Masuda, *Determination of amphibole fracture strength for quantitative palaeostress analysis using microboudinage structures*, Journal of Structural Geology **32**(2), 136-150 (2010).

2. T. Masuda, **S. Nakayama**, N. Kimura, and A. Okamoto, *Magnitude of σ1, σ2, and σ3 at mid-crustal levels in an orogenic belt: Microboudin method applied to an impure metachert from Turkey*, Tectonophysics **460**(1-4), 230-236 (2008).

1. T. Masuda, **S. Nakayama**, N. Kimura, K. Onodera and A. Okamoto, *Triaxial stress state deep in orogenic belts: An example from Turkey*, Journal of Structural Geology **26**(12), 2203-2209 (2004).